DNA-based nanobiostructured devices: The role of quasiperiodicity and correlation effects

E.L. Albuquerque [a,*], U.L. Fulco [a], V.N. Freire [b], E.W.S. Caetano [c], M.L. Lyra [d], F.A.B.F. de Moura [d]

[a] Departamento de Biofísica e Farmacologia, Universidade Federal do Rio Grande do Norte, 59072-970, Natal-RN, Brazil
[b] Departamento de Física, Universidade Federal do Ceará, 60455-760, Fortaleza-CE, Brazil
[c] Instituto Federal de Educação, Ciência e Tecnologia do Ceará, 60040-531, Fortaleza-CE, Brazil
[d] Instituto de Física, Universidade Federal de Alagoas, 57072-970, Maceió-AL, Brazil

ABSTRACT

The purpose of this review is to present a comprehensive and up-to-date account of the main physical properties of DNA-based nanobiostructured devices, stressing the role played by their quasi-periodicity arrangement and correlation effects. Although the DNA-like molecule is usually described as a short-ranged correlated random ladder, artificial segments can be grown following quasiperiodic sequences as, for instance, the Fibonacci and Rudin–Shapiro ones. They have interesting properties like a complex fractal spectra of energy, which can be considered as their indelible mark, and collective properties that are not shared by their constituents. These collective properties are due to the presence of long-range correlations, which are expected to be reflected somehow in their various spectra (electronic transmission, density of states, etc.) defining another description of disorder. Although long-range correlations are responsible for the effective electronic transport at specific resonant energies of finite DNA segments, much of the anomalous spread of an initially localized electron wave-packet can be accounted by short-range pair correlations, suggesting that an approach based on the inclusion of further short-range correlations on the nucleotide distribution leads to an adequate description of the electronic properties of DNA segments. The introduction of defects may generate states within the gap, and substantially improves the conductance, specially of finite branches. They usually become exponentially localized for any amount of disorder, and have the property to tailor the electronic transport properties of DNA-based nanoelectronic devices. In particular, symmetric and antisymmetric correlations have quite distinct influence on the nature of the electronic states, and a diluted distribution of defects lead to an anomalous diffusion of the electronic wave-packet. Nonlinear contributions, arising from the coupling between electrons and the molecular vibrations, promote an electronic self-trapping, thus opening up the possibility of controlling the spreading of the electronic density by an external field. The main features of DNA-based nanobiostructured devices presented in this review will include their electronic density of states, energy profiles, thermodynamic properties, localization, correlation effects, scale laws, fractal and multifractal analysis, and anhydrous crystals of their bases, among others. New features, like other nanobiostructured devices, as well as the future directions in this field are also presented and discussed.

© 2013 Elsevier B.V. All rights reserved.

* Corresponding author. Tel.: +55 8432153419; fax: +55 8432153791.
E-mail address: eudenilson@gmail.com (E.L. Albuquerque).

Contents

1. Introduction

The field of nanotechnology has emerged as one of the most important areas of research in the near future. While scientists have been hardly aspiring to controllably and specifically manipulate structures at the micrometer and nanometer scale, nature has been performing these tasks and assembling structures with great accuracy and high efficiency using specific biological molecules, such as the deoxyribonucleic-acid (DNA) molecule, and proteins [1,2]. As a consequence, there has been a tremendous interest in recent years to develop concepts and approaches for self-assembled systems, searching for their electronic and optical applications [3]. Biology can provide models and mechanisms for advancing this approach, but there is no straightforward way to apply them to electronics since biological molecules are essentially electrically insulating [4]. However, exquisite molecular recognition of various natural biological materials can be used to form a complex network of potentially useful systems for a variety of optical, electronic, and sensing applications [5]. For instance, investigations of electrical junctions, in which single molecules or small molecular assemblies operate as conductors connecting traditional electrical components, such as metal or semiconductor contacts, constitute a major part of what is nowadays known as molecular electronics [6–10]. Their diversity, versatility, and amenability to control and manipulation, make them potentially important components in nanoelectronic devices [11–14].

For physicists, this continuing progress and the consequent need for further size miniaturization, makes the DNA molecule, the basic building block of living species and carrier responsible of the genetic code [15–17], the best candidate to fulfill this place. Arguably, one of the main challenging research subject of nowadays science, the human DNA is around 6 mm long, has about 2×10^8 nucleotides and is tightly packed in a volume equal to $500 \, \mu m^3$ [18]. If a set of three nucleotides can be assumed to be analogous to a byte, then these numbers represent either 1 Kb μm^{-1} (linear density) or 1.2 Mb μm^{-3} (volume density), an appreciation of how densely information can be stored in DNA.
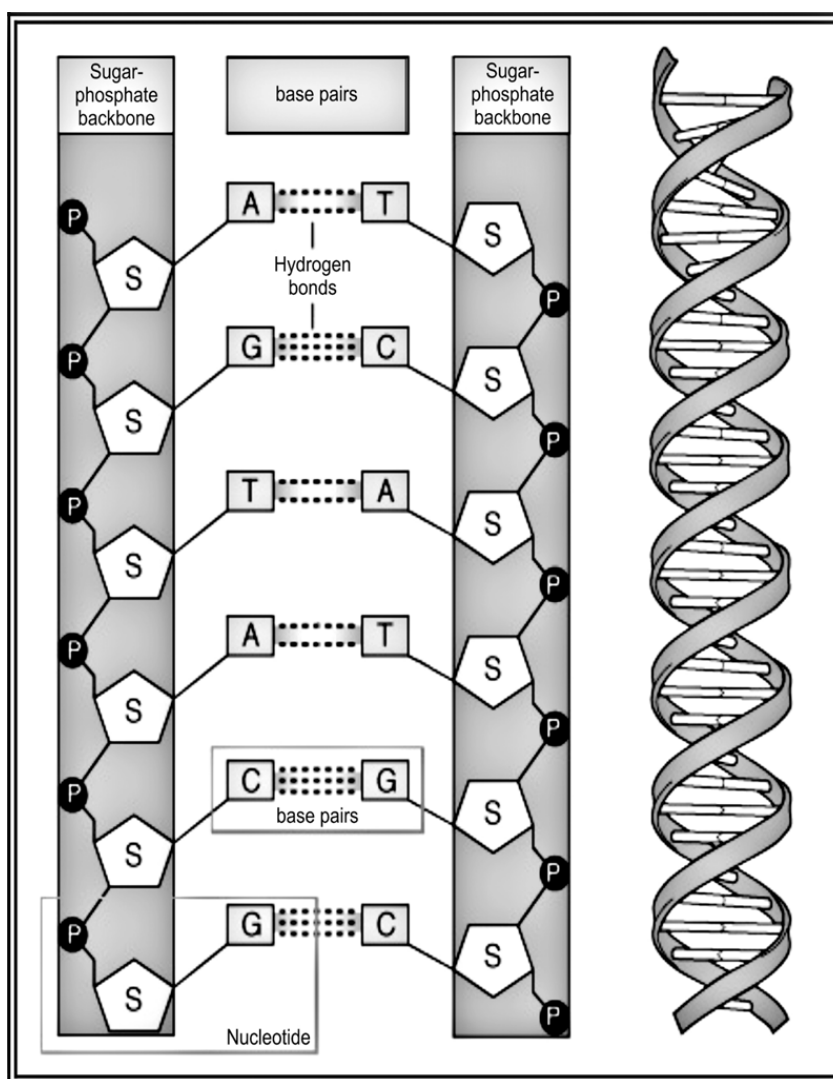
Fig. 1.1. Schematic illustration of the chemical composition of the DNA molecule, showing its four bases guanine (*G*), adenine (*A*), cytosine (*C*) and thymine (*T*) and the sugar–phosphate backbone.

A complete DNA molecule is a chromosome, with protein components present as structural support. The DNA of each gene carries a chemical message which signals to the cell how to assemble the amino acids in the correct sequence to produce the protein for which that gene is responsible. The information is contained in the sequence of the monomers called nucleotides, which make up the DNA molecule, whose structure consists of a base together with a backbone of alternating sugar molecules and phosphate ions. There are four different nucleotides in DNA, differing by their chemical components, linked together forming a backbone of alternating sugar–phosphate residues with the bases that carries the information of the gene. For practical reason these nucleotides can be considered as a symbolic sequence of a four letter alphabet, namely guanine (*G*), adenine (*A*), cytosine (*C*) and thymine (*T*), whose repeated stacks are formed by either *AT* (*TA*) or *GC* (*CG*) pairs coupled by hydrogen bonds, the so-called Chargaff rules [19,20], and held in a double-helix structure by a sugar–phosphate backbone (see the schematic drawing depicted in Fig. 1.1). The specificity of this base pairing and the ability to ensure that it occurs in this fashion (and not some other) is a key factor to use DNA in materials applications. The double helical arrangement of the two molecules leads to a linear helix axis, linear not in the geometrical sense of being a straight line, but in the topological sense of being unbranched. This robust, although malleable, one-dimensional structure of DNA is unique, and may be used to design functional nanostructures, and its charge transport capability in the appropriate energy regime can be quite good. Besides, DNA molecules encode all the information needed to build every cell, tissue and membrane of a living organism and, consequently, occupy an outstanding position in life sciences for its crucial role as carrier of the genetic code.

Numerous algorithms have been introduced to characterize and graphically represent the genetic information stored in the DNA nucleotide sequence. The goal of these methods is to generate a representative pattern for certain sequences, or groups of sequences. Notwithstanding, the design of DNA-based devices for molecular nanoelectronics is not yet an easy task since they are crucially dependent upon elucidation of the mechanism and dynamics of electrons and hole transport in them. Besides, unlike proteins, DNA is not primarily an electron/hole-transfer system, and its suitability as a potential building block for molecular devices may not depend only on long-distance transfer of electrons and holes through the

molecule. However, the discovery that DNA, like proteins, can conduct an electrical current, has made it an interesting candidate for nanoelectronic devices, which could help to overcome the limitations that classical silicon-based electronics is facing presently. Indeed, individual DNA molecules are very suitable for producing a new range of devices that are much smaller, faster and more energy efficient than the present semiconductor-based ones [21].

In fact, DNA offers a solution to many of the hurdles that need to be overcome, since it has the capacity of self-assemblage and self-replication, turning possible to produce nanostructures with a precision that is not achievable with classical silicon-based technologies [22–24]. On the other hand, their conductivity properties are still under intense debate. Controversial reports consider that DNA may be a good linear conductor, while others have found that it is somewhat more effective than proteins, even when they have perfectly ordered base pairs [25]. Recent measurements of electrical transport through individual short DNA molecules indicated that it has a wide-band-gap semiconductor behavior [26,27]. Besides, strongly deformed DNA molecules deposited on a substrate and connected to metallic electrodes can behave as an insulator or a conductor depending, among other things, on the ratio between the thickness of the substrate and molecule [28]. On the other hand, it was recently shown, within the density functional theory (DFT) framework, that anhydrous crystals of the DNA bases are wide band gap semiconductors. Guanine and cytosine (adenine and thymine) anhydrous crystals were predicted to be direct (indirect) band gap semiconductors, with energy gap values equal to 2.68 eV and 3.30 eV (2.83 eV and 3.22 eV), respectively, while the experimentally estimated band gaps measured were 3.83 eV and 3.84 eV (3.89 eV and 4.07 eV), in the same order [29]. The obtained electronic effective masses at band extremes showed that, at low temperatures, anhydrous crystals of DNA bases behave like wide band gap semiconductors for electrons moving along the nucleobases stacking direction, while the hole transport is somewhat limited.

These seemingly contradictory theoretical and experimental results are caused mainly by three factors:

(a) native DNA consists of a double helix with an aperiodic sequence, sugar–phosphate side chains, and water as well as ions surrounding it;
(b) the topology of the double-helix, which is not a rigid object, with the different constituents of DNA moving relative to each other;
(c) the works so far have been performed by using quite different theoretical methods and experimental techniques.

On the other hand, advances on novel DNA constructions, with the creation of three-dimensional DNA topological structures, are opening up a new world for charge transport in DNA junctions and lattices, a scientific advance bridging the molecular world to the world where we live [30,31]. As a matter of fact, the DNA base pairs recognition system can be used to direct the assembly of highly structured materials into a series of 3D triangle-like motifs, with specific nanoscale features, as well as in DNA computation to process complex information, as explicitly stated by Seeman [32]. The combination of synthetic stable branched DNA and sticky-ended cohesion (small cohesive sequences on each end of the motif), that attach to other molecules and place them in a set order and orientation, has led to the development of structural DNA nanotechnology over the last 30 years [32].

The early topological constructs built from DNA led also to the development of specific single-stranded DNA topologies [33,34]. The action of staple strands was later explored to fold DNA strands into a variety of shapes, a technique named DNA origami, which uses a few hundred short DNA strands to direct a very long DNA strand to form structures to any desired shape, serving as their assembly line's framework [35,36]. Nowadays, these several nanometric structures, with great potential biotechnological applications, have evolved to the ability to produce two and three-dimensional DNA crystals with a linear dimension of the order of 1 mm [37]. To explore the complex charge transport in these 3D connected DNA, wire fragments will give rise to novel DNA-based circuits and/or devices, opening up a powerful new direction in the field of integrated nanoelectronic biological structures [38].

Within the above context, the purpose of this review article is to present a comprehensive and up-to-date account of the main electronics/thermodynamics properties of the DNA molecule, mainly within the context of quasiperiodicity of the bases arrangement, and the role played by short- and long-range correlation effects, looking for nano-size devices [39,40]. The DNA is usually described as a short-ranged correlated random ladder, but nothing prevents that the DNA chain can be artificially grown following quasiperiodic sequences as, for instance, the Fibonacci (FB) and Rudin–Shapiro (RS) ones. These structures exhibit interesting properties, namely:

(a) they have a complex fractal spectra of energy, which can be considered as their indelible mark;
(b) they also exhibit collective properties that are not shared by their constituents.

These collective properties are due to the presence of long-range correlations, which are expected to be reflected somehow in their various spectra (as in light propagation, electronic transmission, density of states, etc.) defining another description of disorder (for up to date reviews, see Refs. [41–43]). Besides, the introduction of long range correlations in aperiodic or genomic DNA sequences markedly change their physics and can play a crucial role in their charge transfer efficiency, making a strong impact on their engineering biological processes like gene regulation and cell division [44,45]. Moreover, the nature of this long range correlation has been the subject of intense investigation, whose possible applications on electronic delocalization in the one-dimensional Anderson model have been recently discussed [46].

It is well known that the DNA electronic band structure is composed of two main bands of allowed states separated by an energy gap, similar to those of a solid-state semiconductors. At half filling the presence of the energy gap gives to these molecules an intrinsic insulator character. The introduction of defects may generate states within the gap and substantially

improve the conductance, specially of finite molecules. In single-strand DNA molecules, defects may be originated within the own nucleotide sequence or by laterally attaching new structures at random [47]. However, disorder modifies profoundly the nature of the electronic states in 1D systems. All states usually become exponentially localized for any amount of disorder. Such exponential localization competes with the above improvement on the conductance associated with the presence of states within the gap. Therefore, schemes for introducing defects that minimize the tendency of exponential localization of the electronic states are essential to tailor the electronic transport properties of DNA-based nanoelectronic devices.

We will not consider the possible influence of the environment, like solvent interactions, although its effects may act as a source of disorder [48–50], being important, by instance, in the study of DNA denaturation process [51,52]. However we do consider the influence of the sugar–phosphate backbone, since it promotes the emergence of a band gap of the order of the hopping integral. Recent results showed that the hybridization of the overlapping p-orbital in the base-pair stack coupled to the backbone is sufficient to predict the existence of a gap in the nonequilibrium current–voltage characteristics, with a minimal number of parameters [53].

This review article is organized so that we start with the basic properties of the quasiperiodic structures, giving examples of some of them that either can be or already have been grown by experimentalists like the Cantor, Fibonacci, and Rudin–Shapiro sequences (Section 2). Then, in Section 3, we discuss the important issue of charge transport in the DNA molecule, based on an effective tight-binding model describing an electron moving in a chain with a single orbital per site and nearest-neighbor interactions, together with a transfer-matrix approach to simplify the algebra, which can be otherwise quite heavy. Several different DNA's topologies are taken into account. Section 4 deals with the electrical conductivity looking for their electronic transmission spectra, as well as discussing their wave-function spread profile. The basic properties of their $I–V$ characteristics curves, following a Landauer–Büttiker formulation, are also presented and discussed considering a framework in which the DNA molecule is sandwiched between two electrodes (donor—DN and acceptor—AC, respectively). The effect of diluted disorder is also discussed. The role played by the correlations effects are then introduced, with emphasis in their symmetric and antisymmetric characteristics (Section 5), followed by a discussion of the importance of the inclusion of nonlinearity and field effects into the wave-packet dynamics, which are stressed in Section 6. Mimicking the DNA molecule as a quasiperiodic arrangement of Fibonacci or Rudin–Shapiro sequences, and taking into account that usually collective modes propagating in quasiperiodic systems lead, among other things, to self-similar fractal energy spectra forming a Cantor set, we present in Section 7 their thermodynamic properties using simulation methods employed in the physics of fractals. In general, the properties of the specific heat derived from the natural continuous fractal spectrum obtained from quasiperiodic structures show that at the low temperature limit both systems exhibit an interesting oscillatory behavior in their spectra. This occurs because such systems possess long-range correlations in its own constitution, leading to the transference of these characteristics to their energy spectra in the form of a fractal distribution of bands. As a consequence of this type of distribution, the specific heat oscillates log-periodically when the system temperature goes to zero, depicting a Schottky anomaly. In the sequence it is highlighted that, although the crystal structures of anhydrous thymine and cytosine were determined several years ago, the crystal structures of anhydrous guanine and adenine were not obtained until recently, due to the lack of good quality crystals. Taking advantage of this state of the art, Section 8 deals with the subject of DNA bases crystals, in which published crystallographic data for anhydrous DNA nucleobase crystals (ACrs) guanine, adenine, cytosine and thymine were used, together with the Density Functional Theory (DFT) computations, to set up a comparative study of their structural, electronic, and optical properties. Finally, in Section 9, the prospecting future trends and concluding remarks of this work are presented.

2. Quasiperiodic structures

The subject of quasicrystals first achieved prominence in 1984, following the report by Schechtman et al. [54] of metallic Al–Mn alloys, showing amassing and interesting electron diffraction data. They mixed Al and Mn in a roughly six-to-one proportion and heated the mixture until it melted. The mixture was then rapidly cooled back to the solid state by dropping the liquid into a cold spinning wheel, a process known as melt spinning. When the solidified alloy was examined with an electron microscope, a novel structure was revealed. It exhibited five-fold symmetry, which is forbidden in ideal crystals, and a long-range order, which is lacking in amorphous solids. Its order, therefore, was neither truly amorphous nor crystalline. Subsequent measurements, using X-ray scattering at much higher resolution, led to electron diffraction patterns showing not only five-fold but also icosahedral symmetries, forbidden by the rules of crystallography (for reviews see Refs. [55–59]). Theoretical studies developed by Levine and Steinhardt [60] explained these types of symmetry through the aperiodic 2D and 3D Penrose tilings [61] in their diffraction patterns. Tiling is the geometrical operation that results in filling a space with an arrangement of regular polyhedra. Their predictions were, indeed, qualitatively similar to the observations by Schechtman et al. [54]. In addition to further experimental studies, the subsequent challenge has been the development of theoretical models to characterize these artificial structures.

Although the term quasicrystal is more appropriate when applied to natural compounds or artificial alloys, in 1D there is no difference between it and the quasiperiodic structures formed by the incommensurate arrangement of periodic unit cells. The particular mathematical sequences (Cantor, Fibonacci and Rudin–Shapiro, among others) that define the type of quasiperiodic structure will be discussed in the following sub-sections. An appealing motivation for studying such structures is that they exhibit a highly fragmented energy spectrum displaying a self-similar pattern [62–64]. Indeed, from a strictly mathematical perspective, it has been proven that their spectra are Cantor sets in the thermodynamic limit [65].

A fascinating feature of these quasiperiodic structures is that they exhibit distinct physical properties, not found neither in periodic arrangements, nor in their constituent parts, giving rise to a novel description of disorder. Indeed, theoretical transfer matrix treatments can be used to show that these spectra are fractals, defining intermediate systems between periodic crystals and random amorphous solids [66–69]. This is one of the features that makes them of particular interest to study.

The presence and nature of long-range correlations in such systems preclude using canonical approaches like perturbation theory, where one first separates a small localized piece of the system, treating the rest as a perturbation *a posteriori*. This approach typically does not work for the cases under consideration here, because the behavior of the overall macroscopic system is quite distinct from the behavior of its separate small pieces, due to the long-range correlations. Fortunately, the presence of long-range correlations itself gives the key to circumvent this difficulty, namely that these systems are normally robust to wide modifications on a microscopic scale. An important consequence of this robustness, where many systems which are distinct within a microscopic scale may exhibit the same critical behavior, is that one can classify the various systems in a few universality classes (for details see Ref. [70]). For an analogy, we may consider the topic of continuous phase transitions: the critical behavior is known to depend only upon global properties, namely the geometric dimension of the system and the symmetries of its order parameter, being insensitive to the details of the microscopic interactions between the atoms or molecules [71].

The spectra of many types of elementary excitations in quasiperiodic structures have been extensively studied by numerous groups. In all cases, the spectra were found to be Cantor-like with critical eigenfunctions [72]. For electronic systems, exact eigenfunctions were found only at the special null energy value. However, there are infinitely many eigenvalues in the energy spectrum, although they are rare for the electron chaotic orbits [73,74]. An important issue is to understand the wave functions corresponding to these chaotic orbits. We note that it does not necessarily follow that the wave functions themselves are chaotic, because the orbits represent only selected points on the lattice [75]. In addition, there may be a discrete set of extended states, and a quite complex fractal energy spectrum, which can be considered as their basic signature, a common feature of these systems. Several different mathematical techniques, including renormalization group theory [76], the transfer matrix method [77], and chaotic Hamiltonian systems [78], to mention just a few, have been successfully applied to describe quasiperiodic structures, leading to remarkable results.

Another important motivation for studying quasiperiodic structures comes from recognizing that the localization of electronic states, one of the most active fields in condensed matter physics, could occur not only in disordered systems but also in the deterministic quasiperiodic systems [79,80]. Localization of electronic states in quasi-periodic structures were studied using a tight-binding Schrödinger equation by several groups [81–83].

The quasiperiodic structures considered here are of the type generally known as substitutional sequences. The sequences generated by substitutions have been studied in several areas of mathematics [84–86], computer science [87,88], and cryptography [89]. The sequences are characterized by the nature of their Fourier spectrum, which can be dense pure points (as for the Fibonacci sequence) or singular continuous (as for the Rudin–Shapiro sequence) [90].

We start with some general mathematical considerations and terminology. First we give the definition of a substitutional sequence of the type used here. Consider a finite set ξ (here $\xi = \{A, B\}$, for example, with A and B being two different building blocks) called an alphabet, and denote by ξ^* the set of all words of finite length (such as *AABAB*) that can be written in this alphabet. Now let us define ζ as a map from ξ to ξ^* by specifying that ζ acts on a word by substituting each letter (e.g. *A*) of this word by its corresponding image, denoted by $\zeta(A)$. A sequence is then called a substitutional sequence if it is a fixed point of ζ, i.e. if it remains invariant when each letter in the sequence is replaced by its image under ζ.

These substitutional sequences are described in terms of a series of generations that obey particular inflation rules. Let $a_1, a_2, \ldots, a_g$ be g basic units, and define this pattern as stage n of the sequence. Then the next stage $n + 1$ of the sequence is obtained inductively from stage n by the inflation rule $\vec{a} \to \bar{M}\vec{a}$, where $\vec{a}$ represents the column vector $(a_1, a_2, \ldots, a_g)^t$, with t denoting the transpose. Also $\bar{M} = (m_{ij})$ is a $g \times g$ matrix with non-negative integer matrix elements. The matrix $\bar{M}$ and its successive applications fully determine the sequence. At each stage, a_i is replaced by $m_{i1}a_1$, followed by $m_{i2}a_2, \ldots$, etc., for $i = 1, 2, \ldots, g$. For example, for the case of the Fibonacci lattice to be discussed shortly, we have $g = 2$ and it turns out that we operate with the 2×2 substitution matrix $\bar{M}$

$$\bar{M} = \begin{pmatrix} 1 & 1 \\ 1 & 0 \end{pmatrix}, \tag{1}$$

on the vector $(a_1, a_2)^t$ at each stage. This gives, in terms of the building blocks A and B, the substitution rules $A \to AB$, $B \to A$ which will then generate the whole sequence, provided we start with AB as the first compound word of the sequence. Similar procedures can be identified to generate other quasiperiodic sequences. In the following, we proceed to give explicit definitions of the main substitutional sequences to be used here.

2.1. Cantor

Probably the most well-known and simple deterministic fractal geometry is the triadic Cantor sequence [91]. This set is obtained through the repetition of a simple rule: divide any given segment into three equal parts, then eliminate the central one (we may call this the *inbound* Cantor sequence), and continue this process. For example, if we start algebraically with the closed set $S_0 = [0, 3]$ of all numbers from 0 to 3 and remove its open middle third, we are left with the pair of closed intervals
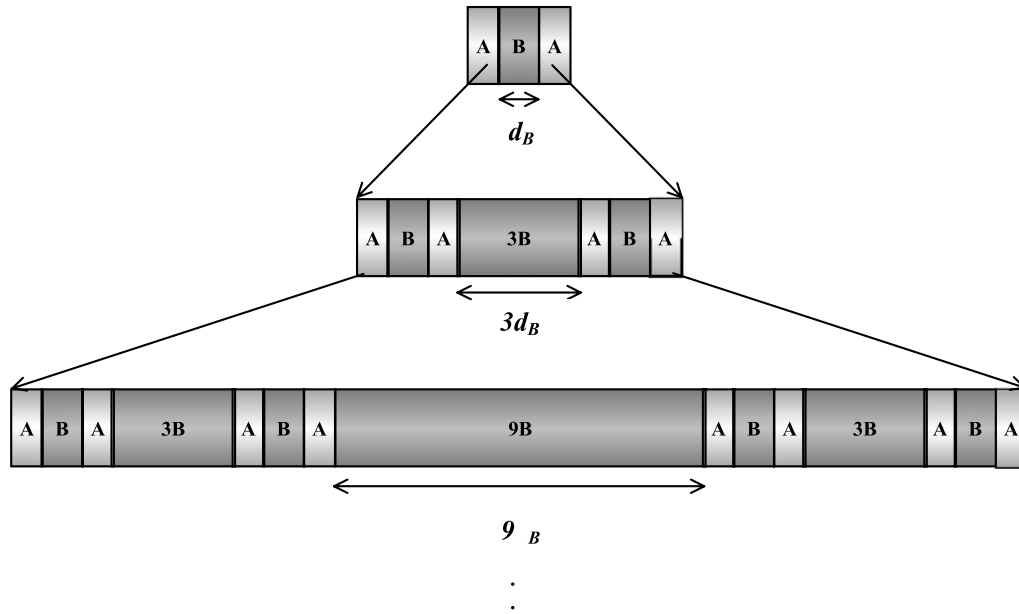
Fig. 2.1. Schematic illustration of the Cantor quasiperiodic structure.

[0, 1] and [2, 3] representing S_1. The open middle thirds in each of these intervals would be removed again to produce four smaller intervals representing S_2, and so on. After many stages, we would have a large number of small intervals, separated by gaps of various sizes.

For applications of the building blocks to multilayered structures, it is more appropriate to consider instead the so-called *outbound* Cantor sequence. This has its N_cth stage defined in terms of the previous stage by the rule $S_{N_c} = S_{N_c-1} B_{N_c} S_{N_c-1}$, with initial conditions taken as $S_0 = A$ and $S_1 = AB_1 A$. In this case B_{N_c} for the N_cth sequence stage differs from the basic B_1 ($\equiv B$) for the first stage only by its thickness $d_{B_{N_c}} = 3^{N_c-1} d_{B_1}$. We can also construct the same sequence rather more straightforwardly by the substitutional transformations $A \rightarrow ABA, B \rightarrow BBB$.

The resulting Cantor generations are therefore

$$S_0 = A; \qquad S_1 = ABA; \qquad S_2 = ABABBBABA; \qquad \text{etc.} \tag{2}$$

which are represented clearly by the diagrammatic expansion scheme shown in Fig. 2.1.

The fractal properties of the quasiperiodic structures will turn out to be of relevance later for a description of the excitation spectrum. Roughly speaking, fractals can be thought of as complex geometric shapes with fine structure at arbitrary small scales. It is obvious how this fine structure comes about in the above example of the Cantor sequence because of the repeated division into smaller intervals. Some general accounts of fractals and their properties are to be found in several books, e.g. Refs. [91–93]. The concept of fractal dimension is often useful in respect to the self-similarity property, i.e. again roughly, if we magnify a tiny part of the fractal we will see features reminiscent of the whole. If, from a d-dimensional object (a "box") of size l, some N conformal copies of reduced size lr (with $0 < r < 1$) are produced and the process is repeated a large number of times, then the fractal dimension D_0 can be defined by the relation $N = \exp(-rD_0)$, or equivalently

$$D_0 = \ln(N)/\ln(1/r). \tag{3}$$

For the present example of the Cantor sequence, we have $N = 2$ and $r = 1/3$, so it has a fractal dimension equal to a noninteger, namely $\ln 2/\ln 3 \simeq 0.63$. This is less than its geometric dimension $d = 1$.

2.2. Fibonacci

The Fibonacci sequence (FB) is the oldest example of an aperiodic chain of numbers. It was developed by Leonardo de Pisa (whose nickname was Fibonacci) in 1202 as a result of his investigation on the growth of a population of rabbits. The successive Fibonacci numbers are generated by adding together the two previous numbers in the sequence, after specifying suitable initial conditions.

For our purposes, a Fibonacci structure can be realized experimentally by juxtaposing the two basic building blocks A and B in such a way that the N_{FB}th stage of the process $S_{N_{FB}}$ is given by the recursive rule $S_{N_{FB}} = S_{N_{FB}-1} S_{N_{FB}-2}$, for $N_{FB} \geq 2$, starting with $S_0 = B$ and $S_1 = A$. It has the property of being invariant under the transformations $A \rightarrow AB$ and $B \rightarrow A$.

The Fibonacci generations are (see Fig. 2.2(a)):

$$S_0 = B; \qquad S_1 = A; \qquad S_2 = AB; \qquad S_3 = ABA; \qquad S_4 = ABAAB; \qquad \text{etc.} \tag{4}$$
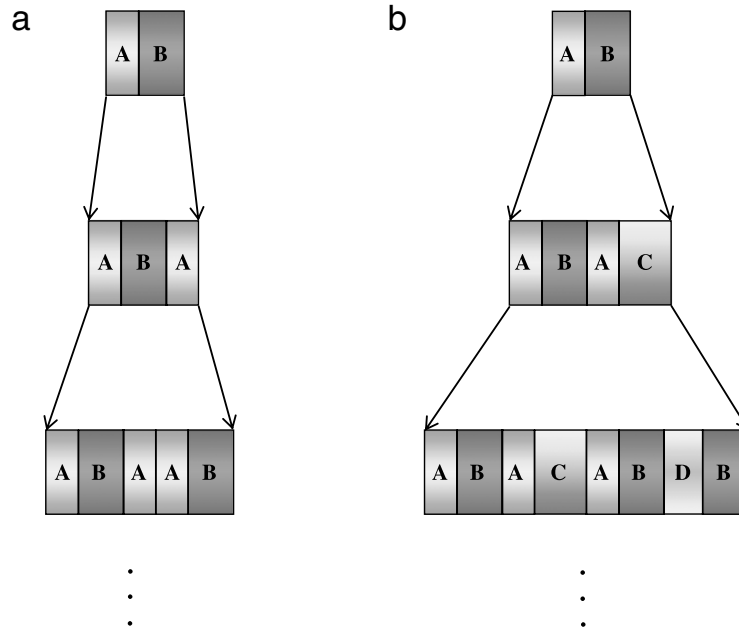
Fig. 2.2. Schematic illustration of the two quasiperiodic structures considered in this work: (a) Fibonacci; (b) Rudin–Shapiro.

In this case, the number of building blocks increases in accordance with the Fibonacci number F_{N_F} defined by the rule $F_{N_{FB}} = F_{N_{FB}-1} + F_{N_{FB}-2}$ (with $F_0 = F_1 = 1$). Also the ratio between the number of the building blocks A and the number of the building blocks B in the sequence tends to the golden mean number $\tau_{FB} = (1 + \sqrt{5})/2 \simeq 1.62$ for large generation number N_{FB}. This particular irrational number is related to five-fold symmetries (e.g. it is twice the ratio of the distance between the center-vertex and the center mid-edge in a pentagon). It is interesting to note that all the Fibonacci numbers can be generated from the golden mean number through the relation $F_{N_{FB}} = [(\tau_{FB})^{N_{FB}} - (-\tau_{FB})^{-N_{FB}}]/\sqrt{5}$. This means that a sequence of rational numbers (namely the integer-valued Fibonacci numbers) can be obtained from powers of irrational numbers.

There are variations of the above sequence leading to generalized Fibonacci structures (GFB) that involve different relationships between the number of the building blocks A and the number of the building blocks B (thus generalizing also the golden mean number). In these cases, the Nth stage of the structure $S_{N_{GFB}}$ is taken to be generated by the sequence given recursively as

$$S_{N_{GFB}+1} = S_{N_{GFB}}^p S_{N_{GFB}-1}^q \tag{5}$$

with, as before, $S_0 = B$ and $S_1 = A$. Here the indexes p and q are arbitrary positive integer numbers and $N_{GFB} \geq 1$. The above notation means that $S_{N_{GFB}}^p$ represents p adjacent repetitions of the stack $S_{N_{GFB}}$. This type of inheritance is normal in iterative processes and frequently produces self-similar structures that are the basis of fractal configurations. When $p = q = 1$ (the simplest possible case) we have just the well-known Fibonacci sequence discussed previously. Equivalently, the generalized Fibonacci sequences can also be generated by the substitutional relation

$$B \to A, \qquad A \to A^p B^q, \tag{6}$$

where A^p (or B^q) represents a string of p A-blocks (or q B-blocks). The total number of blocks in $S_{N_{GFB}}$ is equal to the generalized Fibonacci number denoted by $F_{N_{GFB}}$, given now by the recurrence relation

$$F_{N_{GFB}} = pF_{N_{GFB}-1} + qF_{N_{GFB}-2}, \tag{7}$$

with initial values $F_0 = F_1 = 1$. The characteristic value $\tau(p, q)$, defined as being the ratio of $F_{N_{GFB}}$ to $F_{N_{GFB}-1}$ in the limit of $N_{GFB} \to \infty$, must satisfy the quadratic equation

$$\tau(p, q)^2 - p\tau(p, q) - q = 0. \tag{8}$$

Solving for the positive root gives explicitly

$$\tau(p, q) = \lim_{N_{GFB} \to \infty} F_{N_{GFB}}/F_{N_{GFB}-1} = \frac{p + \sqrt{p^2 + 4q}}{2}. \tag{9}$$

This expression generalizes the previous golden-mean result and introduces other types of means, depending on the values of p and q. For instance, for $p = q = 1$ we have $\tau(1, 1) \equiv \tau_{FB} \simeq 1.62$, the well-known golden mean. Similarly, $\tau(2, 1) \simeq 2.41$ is the silver mean, $\tau(3, 1) \simeq 3.30$ is the bronze mean, and $\tau(1, 3) \simeq 2.30$ is the nickel mean.

It is worth briefly mentioning here a mathematical aspect that has interesting implications for the physical properties of a quasiperiodic system. We may note that the expression for $\tau(p, q)$ in Eq. (9) is formally equivalent to a result arising when determining the eigenvalues of the substitution matrix $\bar{M}$ introduced earlier in this section. This was exemplified by Grimm and Baake [94] in treating a quantum spin chain with quasiperiodic pair interactions. Essentially they were able to classify the different substitutional sequences based on the irrationality of $\tau^-(p, q)$, which denotes the negative root of Eq. (9). They found that if $|\tau^-(p, q)| < 1$, it is a so-called Pisot–Vijayaraghavan (PV) irrational number, and the fluctuations of the physical properties associated with the sequence are relatively well behaved and stable. On the other hand, if $|\tau^-(p, q)| > 1$, the fluctuations of the physical properties are almost chaotic. For the examples of generalized Fibonacci cases mentioned above, only the nickel-mean sequence is not a PV type and, therefore, we expect a more chaotic behavior of its physical properties (as found in the specific heat calculations discussed in [95]).

2.3. Rudin–Shapiro

To set up a quasiperiodic chain of Rudin–Shapiro (RS) type, we consider the juxtaposing of four basic building blocks A, B, C, and D, in such a way that they have the property of being invariant under the transformations $A \rightarrow AB$, $B \rightarrow AC$, $C \rightarrow DB$, and $D \rightarrow DC$. The RS sequence belongs to the family of the so-called substitutional sequences, which are characterized by the nature of their Fourier spectrum. It exhibits an absolutely continuous Fourier measure, a property which it shares with the random sequences. The total number of building blocks in the unit cell increases with $2^{N_{RS}+1}$, N_{RS} being the Rudin–Shapiro generation number. The generations of this quasiperiodic structure are:

$$S_0 = [AB]; \qquad S_1 = [ABAC]; \qquad S_2 = [ABACABDB]; \qquad S_3 = [ABACABDBABACDCAC]; \qquad \text{etc.} \tag{10}$$

as depicted in Fig. 2.2(b).

3. Charge transport in DNA

Charge transport in DNA molecules attracts considerable interest among the physics, chemistry, and biology communities, not only because of its relevance, as the carrier of genetic code of all living organisms, but also as a promising candidate for molecular electronics. In fact, the use of molecules as an electronic component is a powerful new direction in the science and technology of nanometer-scale systems due to their scientific and engineering applications [96,97]. Besides, charge mobility in DNA has its own importance based on its biological context, as well as on its technological applications, (e.g. the use of DNA in electrochemical sensors and in future nanotechnologies [99,98]). In fact, the electronic conduction in DNA molecules is a research frontier in molecular electronics because of their potential use in nanoelectronic devices, both as a template for assembling nanocircuits, and as an element of such circuits [100,101]. Processes that possibly use charge transfer include, among others, the function of DNA damage response enzymes, transcription factor and polymerase co-factors, all of them playing important roles in the cell [102]. Indeed, it was proved that damaged regions have significantly different behavior than healthy regions in DNA after the passage of an electric current [103].

Although the use of DNA molecules in nanoelectronic circuits is very promising due to their self-assembly and molecular recognition abilities, their conductivity properties are not yet properly recognized. Different conclusions are obtained by several experiments. On the theoretical side, both *ab initio* calculations [104–106] and model-based Hamiltonians [107–110] are extensively adopted to interpret the diversity of the experimental results and to ascertain the underlying charge transport mechanisms. The former can provide a detailed description, but is currently limited to relatively short molecules. The latter is much less detailed although allowing addressing systems of more realistic length. However, the model-based approach can play an additionally important complementary role, because it grasps usually the underlying physics.

Earlier models of the electronic transport in DNA molecules assumed that the transmission channels are along their longitudinal axis. A π-stacked array of the DNA nucleobases, namely guanine (G), adenine (A), cytosine (C) and thymine (T), provides the way to promote long range charge migration, which in turn gives important clues to mechanisms and biological functions of charge transport [111–114].

The increasing diversification of applications requiring materials with specific electronic properties at nanoscale size, and the consequent need for further miniaturization makes the DNA molecule an excellent candidate for molecular electronics. This immediately leads to the question of what are the possible mechanisms governing charge migration through DNA, and what are the parameter ranges (length, temperature, geometrical arrangements etc.) which it may support electric current.

3.1. The tight-binding models

In condensed matter physics, the tight-binding model (or TB model) is an approach to calculate the electronic band structure using an approximate set of wave functions based upon their superposition for isolated atoms located at each atomic site [115,116]. The method is closely related to the LCAO (Linear Combination of Atomic Orbitals) method used in quantum chemistry [117,118]. Tight-binding models are applied to a wide variety of systems, including organic materials such as the DNA molecule, to set up their electronic density of states. Though the tight-binding model is a one-electron
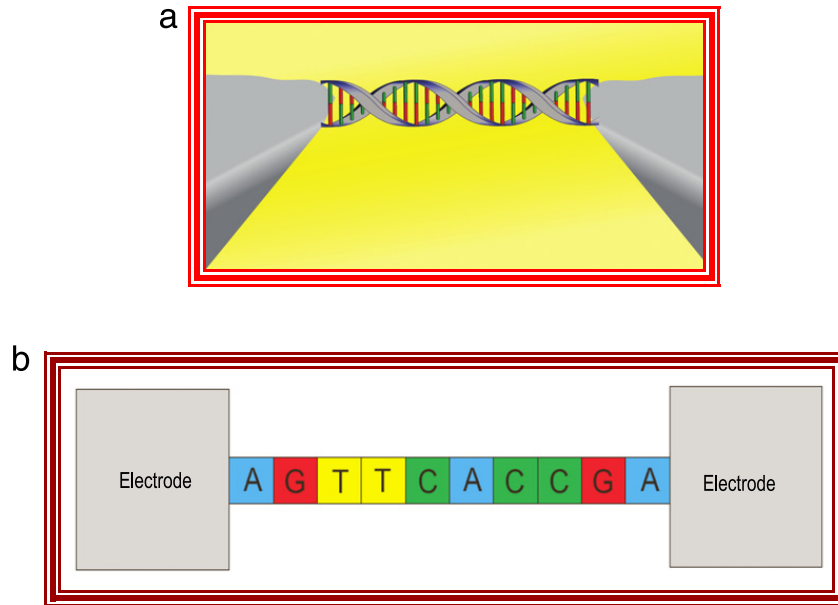
Fig. 3.1. (Color online) Schematic illustration of the DNA molecule sandwiched between two electrodes. (a) pictorial view; (b) the single-strand case.

model, it also provides a basis for more advanced calculations (like that of surface states), and applications to various kinds of many-body problem and quasiparticle calculations. Generally it gives good qualitative results in many cases, and their parameters can be calculated by quantum models such as in the DFT case (Density Functional Theory) [119–121].

The name tight-binding comes from because usually it describes the properties of tightly bound electrons in solids. The electrons in this model should be tightly bound to the atom to which they belong, and they should have limited interaction with states and potentials on surrounding atoms of the solid. As a result, the wave function of the electron will be rather similar to the atomic orbital of the free atom it belongs to. The energy of the electron will also be rather close to the ionization energy of the electron in the free atom or ion because the interaction with potentials and states on neighboring atoms is limited.

Many interesting theoretical results concerning the electronic properties of one dimensional chains have been obtained by using the Schrödinger equation in the tight-binding approximation. A considerable amount of work has been devoted to the study of this equation, for both random and quasiperiodic sequences of the on-site potential ϵ_n and/or the hopping potential t_{nm} between the quantum states $|n\rangle$ and $\langle m|$. The main achievements are:

(a) if the Hamiltonian parameters are independent random variables, the system exhibits Anderson localization, i.e., the eigenstates are exponentially localized, and the energy spectrum itself is a regular object, with at most a finite number of bands [122]. In the case of a binary potential distribution, the spectrum has one or two bands;

(b) if the hopping potentials t_{nm} are a binary sequence arranged in a pure Fibonacci or generalized Fibonacci way, the energy spectrum is a Cantor set of zero (Lebesgue) measure, i.e., there is an infinite number of gaps, and the total bandwidth vanishes. Specifically for the pure Fibonacci case, the eigenstates are neither extended nor localized, but exhibit an intermediate behavior. For the generalized Fibonacci case, the eigenstates are extended [123,124]. In higher-dimensional cases, the energy spectra can be band-like with finite measure, fractal-like with zero band-width, or a mixture of partly band-like and partly fractal-like character [125].

3.2. The single-strand DNA structure model

Consider now a model in which a finite DNA molecule is sandwiched between two electrodes, as depicted in Fig. 3.1(a). For a single-strand DNA chain (Fig. 3.1(b)), the tight-binding Hamiltonian is written in terms of a localized basis as [126,127]:

$$H = \sum_n \epsilon_n |n\rangle\langle n| + \sum_{n,m} t_{nm} |n\rangle\langle m|, \tag{11}$$

where ϵ_n represents the energy (in units of $\hbar$) of the site n, and t_{nm} is the hopping potential. The sum over m is limited to the nearest neighbors.

The Dyson equation is [128,129]

$$G(\epsilon) = \epsilon^{-1}[I + HG(\epsilon)], \tag{12}$$

where I is the identity matrix and H is the Hamiltonian given by Eq. (11).

Starting with the guanine (G) nucleotide as seed, let us consider that the DNA can be modeled by a Fibonacci quasiperiodic sequence, in such a way that it can be built through the inflation rules $G \rightarrow GC$ and $C \rightarrow G$. For the first generation of the FB sequence, with only a guanine linked to the electrodes, its Green function can be found by applying the tight-binding Hamiltonian (11) to the Dyson Eq. (12) to get [130]:

$$G_{nn}^{-1}(\epsilon) = \epsilon - \epsilon_G + 2\gamma(1), \tag{13}$$

where

$$\gamma(1) = -\frac{t_{GS}^2}{\epsilon - \epsilon_S + t_{SS}T(\epsilon)}. \tag{14}$$

Here t_{GS} (t_{SS}) is the hopping term between the guanine G and the substrate S (within the substrate S). Also, $T(\epsilon)$ is the transfer function given by:

$$T(\epsilon) = -(2t_{SS})^{-1}\left[(\epsilon - \epsilon_S) \pm \sqrt{(\epsilon - \epsilon_S)^2 - 4t_{SS}^2}\right]. \tag{15}$$

Repeating the procedure for any Fibonacci generation, we get:

$$G_{nn}^{-1}(\epsilon) = \epsilon - \epsilon_G + \gamma(1) + \kappa(N), \tag{16}$$

where

$$\kappa(N) = -\frac{t_{n,n\pm1}^2}{\epsilon - \epsilon_n + \kappa(N-1)}, \tag{17}$$

with $\kappa(1) = \gamma(1)$, provided we replaced the hopping term t_{GS} by t_{CS} (the hopping term between the cytosine C and the substrate S). Also, N is the number of nucleotides in the strand. The symmetry $t_{n,n+1} = t_{n+1,n}$ holds.

Let us now contrast this results (Fibonacci sequence) with a Rudin–Shapiro (RS) sequence modeling the single-strand DNA molecule. Starting also from a G (guanine) nucleotide as seed, the quasiperiodic RS sequence is then built through the inflation rules $G \rightarrow GC$, $C \rightarrow GA$, $A \rightarrow TC$, and $T \rightarrow TA$. The RS sequence starts to deviate from the FB sequence in the third generation, when the sequence has 4 nucleotides $GCGA$ connected to the electrodes. Using a procedure similar to the quasiperiodic Fibonacci case, we can get for any RS generation number the same expression as for the Fibonacci case provided, in Eq. (16), we replace $\kappa(N)$ by $\gamma(N)$ given by:

$$\gamma(N) = -\frac{t_{n,n\pm1}^2}{\epsilon - \epsilon_n + \gamma(N-1)}. \tag{18}$$

Differently from the FB sequence, observe that for the Rudin–Shapiro sequence $t_{n,n\pm1}$ represents four distinct values of hopping potentials, namely: t_{CT}, t_{GC}, t_{GA}, and t_{TA}, where we have assumed that $t_{n,n\pm1} = t_{n\pm1,n}$ in both cases.

The electronic density of state (DOS), i.e., the number of electronic states per interval of energy at each energy level that are available to be occupied by the electrons, is given by:

$$\rho(\epsilon) = -(1/\pi)\text{Im}\left[\text{Tr}\langle n|G(\epsilon)|n\rangle\right] \tag{19}$$

where Im means the imaginary part of the argument shown between brackets. The energies ϵ_n are chosen from the ionization potential of the respective nucleotides. In the following, we will use as representative values $\epsilon_G = 7.75$ eV (guanine), $\epsilon_A = 8.24$ eV (adenine), $\epsilon_C = 8.87$ eV (cytosine), and $\epsilon_T = 9.14$ eV (thymine) [131,132]. All the hopping terms t_{nm} among the bases were taken equal to 1 eV, considering that theoretical calculations using *ab initio* methods yield for this potential values in the range 0.4–1 eV [131,132]. The potential at the interface DNA–electrode (here considered as a platinum metal) is considered to be the difference between the Fermi's level of the platinum and the HOMO's (Highest Occupied Molecular Orbital) isolate guanine (cytosine) state, giving us $t_{GS} = 2.39$ ($t_{CS} = 2.52$) eV. We are aware that the HOMO state of the guanine (cytosine) may significantly change in the presence of the electrode, yielding a different potential at the interface DNA–electrode. Although we do not expect any relevant change in the DOS main features, the actual electron's localization length may be influenced, specially at the band edges. The hopping term inside the electrode (t_{SS}) is 12 eV [133]. Further, the on-site energy for the electrode (platinum) is $\epsilon_S = 5.36$ eV, which is related with the work function of this metal [134].

Fig. 3.2 depicts the density of states for a DNA quasiperiodic chain corresponding to the 11th (blue line), 13th (red line), and 15th (black line) FB sequence generation number, respectively. Here N_{FB} means the sequence generation number, while n_{FB} corresponds to the number of nucleotides in a given sequence generation. From there we can infer the following main properties:

(a) the parity of the FB generation is not important for the DOS spectrum;
(b) although the DOS for each generation as a whole does not show any symmetry, there are two very well defined and symmetrical regions, lying in the energy's intervals (in units of eV) $5.75 < \epsilon < 9.30$ (we call it region I), and $9.30 < \epsilon < 10.30$ (region II);
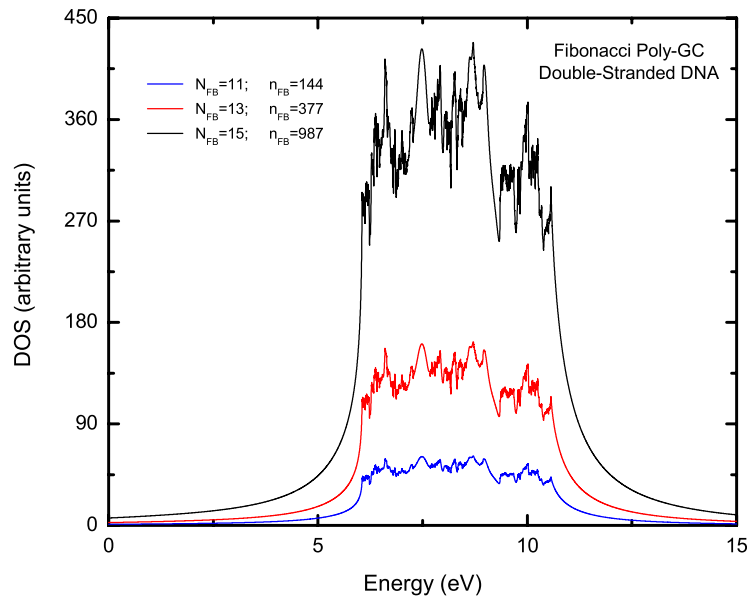
Fig. 3.2. Density of state spectra for the Fibonacci (FB) Poly(GC) DNA single-strand model corresponding to the 11th (blue line), the 13th (red line), and the 15th (black line) FB sequences generation. (For interpretation of the references to colour in this figure legend, the reader is referred to the web version of this article.)

(c) region II, which appears as a sort of anomaly in the DOS spectrum, is due to the presence of the cytosine nucleotide in the quasiperiodic chain. We can also notice that this region represents a kind of the profile of the region I inverted and in a smaller scale.

(d) each region defines a clearly auto-similar spectrum for different generations. The auto-similarity holds also for the whole spectrum (regions I+ II);

(e) the central peak for region I is next to the guanine's ionization energy $\epsilon_G = 7.75$ eV, while the central valley in region II corresponds to $\epsilon_G + 2t_{nm} = 9.75$ eV;

(f) the ratio among the distances of consecutive generations tends to the gold mean, $\tau_{FB} = (1 + \sqrt{5})/2$, a number intrinsically linked to the Fibonacci sequence.

The density of states for a DNA quasiperiodic chain following a Rudin–Shapiro quasiperiodic sequence are shown in Fig. 3.3, corresponding to its 7th (black line), 9th (red line), and 11th (blue line) sequence generation number. Although some similarities with the Fibonacci case persist (for instance, the asymmetry of the spectra and the fact that again the parity of the quasiperiodic generation is not important), they are completely different, indicating how important is the model considered to simulate the DNA structure. As their main features, their central peaks, which are sequence independent, lie around 6.8 eV (which is about $\epsilon_C - t_{nm}$), with the band-width approximately given by $\epsilon_G \pm 4t_{nm}$.

3.3. The double-strand DNA structure model

Consider now the so-called double-strand model to describe an infinite DNA molecule, as depicted in Fig. 3.4. The tight-binding Hamiltonian describing one electron moving in this ladder geometry composed by two interconnected chains of sites, side by side, with a single orbital per site and nearest-neighbor interactions can be given by ($\hbar = 1$):

$$
\begin{aligned}
t(\psi_{n+1}^{\alpha} + \psi_{n-1}^{\alpha}) + w\psi_n^{\beta} = (E - \epsilon_n^{\alpha})\psi_n^{\alpha}, \\
t(\psi_{n+1}^{\beta} + \psi_{n-1}^{\beta}) + w\psi_n^{\alpha} = (E - \epsilon_n^{\beta})\psi_n^{\beta}.
\end{aligned}
\tag{20}
$$

Here ϵ_n^{α} is the single energy at the orbital ψ_n^{α} (the upper index refers to the chain, while the lower index refers to the site position in each chain — see Fig. 3.4). Also, t and w are the intra-chain and the inter-chain first-neighbor electronic overlaps (hopping amplitude), respectively.

Within this framework, the (discrete) Schrödinger equation can be written as

$$
\begin{pmatrix} \psi_{n+1}^{\alpha} \\ \psi_{n+1}^{\beta} \\ \psi_n^{\alpha} \\ \psi_n^{\beta} \end{pmatrix} = M(n) \begin{pmatrix} \psi_n^{\alpha} \\ \psi_n^{\beta} \\ \psi_{n-1}^{\alpha} \\ \psi_{n-1}^{\beta} \end{pmatrix}
\tag{21}
$$
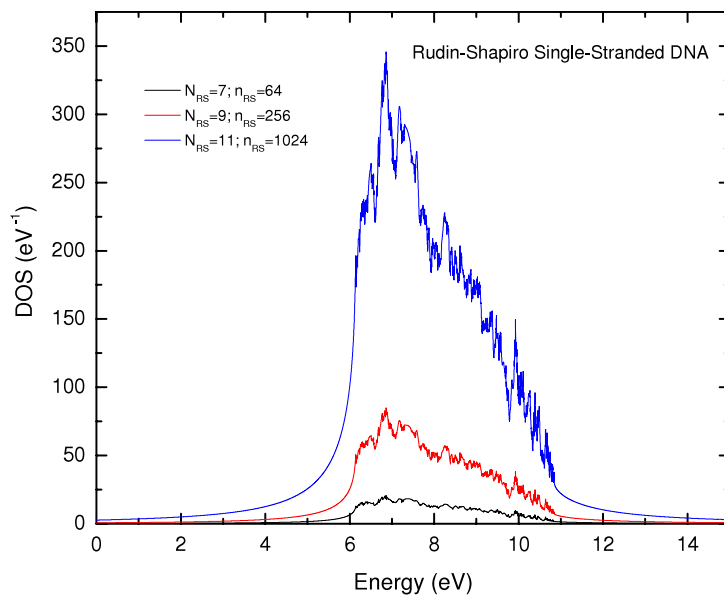
Fig. 3.3. Density of state spectra for the Rudin–Shapiro (RS) DNA single-strand model corresponding to the 7th (black line), the 9th (red line), and the 11th (blue line) RS sequence generation. (For interpretation of the references to colour in this figure legend, the reader is referred to the web version of this article.)

Fig. 3.4. (Color online) Schematic representation of an infinite double-strand DNA molecule, showing the intra-chain (t) and the inter-chain (w) first-neighbor hopping terms. The unit cell L is also depicted.

where $M(n)$ is the transfer matrix

$$M(n) = \begin{pmatrix} (E-\epsilon_n^\alpha)/t & -w/t & -1 & 0 \\ -w/t & (E-\epsilon_n^\beta)/t & 0 & -1 \\ 1 & 0 & 0 & 0 \\ 0 & 1 & 0 & 0 \end{pmatrix}. \tag{22}$$

After successive applications of the transfer matrix $M(n)$, we have

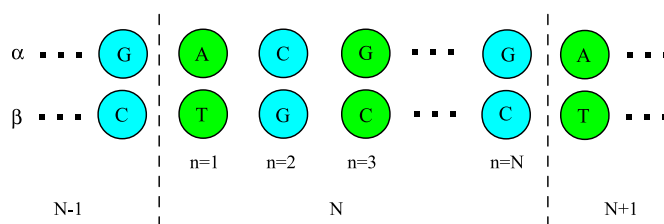$$\begin{pmatrix} \psi_{n+1}^\alpha \\ \psi_{n+1}^\beta \\ \psi_n^\alpha \\ \psi_n^\beta \end{pmatrix} = M(n)M(n-1)\cdots M(2)M(1) \begin{pmatrix} \psi_1^\alpha \\ \psi_1^\beta \\ \psi_0^\alpha \\ \psi_0^\beta \end{pmatrix}. \tag{23}$$

In this way, we have the wave function at an arbitrary site. Calculating this product of transfer matrices is completely equivalent to solve the Schrödinger equation for the system.

Defining the ket formed by the orbitals of the Nth unitary cell, i.e.:

$$|\psi^{(N)}\rangle = \begin{pmatrix} \psi_{N+1}^\alpha \\ \psi_{N+1}^\beta \\ \psi_N^\alpha \\ \psi_N^\beta \end{pmatrix}, \tag{24}$$

and taking into account that in our model, each generated sequence is an unitary cell whose repetition builds up the entire infinite DNA molecule, Bloch's ansatz for each chain yields:

$$|\psi^{(N+1)}\rangle = T_n|\psi^{(N)}\rangle = \exp(iQ_iL)|\psi^{(N)}\rangle, \tag{25}$$

where $T_n = M(n)M(n-1)\cdots M(2)M(1)$, Q_i is the Bloch's wavevector and L the periodic distance. Therefore,

$$[T_n - \exp(iQ_iL)I]|\psi^{(N)}\rangle = 0, \tag{26}$$

where I is the identity matrix. Since T_n is an unimodular matrix (det $T_n = 1$), its eigenvalue should satisfy $\lambda_1\lambda_2\lambda_3\lambda_4 = 1$, i.e., $\lambda_2 = \lambda_1^{-1}$ and $\lambda_4 = \lambda_3^{-1}$, implying the existence of only two independent eigenvalues. Therefore, Bloch's wavevector should satisfy

$$\exp(iQ_rL) = \lambda_r, \quad r = 1, 2. \tag{27}$$

The secular equation is then:

$$\lambda^4 + \Xi\lambda^3 + \Gamma\lambda^2 + \Xi\lambda + 1 = 0, \tag{28}$$

where $\Xi = -\text{Tr}[T_n]$ (Tr meaning the trace of the matrix T_n), and

$$\Gamma = (T_{11} + T_{22})(T_{33} + T_{44}) - T_{34}T_{43} - T_{12}T_{21} - T_{13}T_{31} - T_{14}T_{41} - T_{23}T_{32} - T_{24}T_{42} + T_{11}T_{22} + T_{33}T_{44}. \tag{29}$$

Here, T_{ij} are the elements of the transfer matrix T_n. Rearranging Eq. (28), we have:

$$\gamma^2 + \Xi\gamma + \Gamma - 2 = 0. \tag{30}$$

Here, $\gamma_i = (\lambda_i + \lambda_i^{-1})$, are the roots of the second-order degree equation, each one corresponding to one of the independent eigenvalues of the transfer matrix T_n. Its explicit form is:

$$\gamma_{1,2} = \frac{-\Xi \pm \sqrt{\Xi^2 - 4(\Gamma - 2)}}{2}. \tag{31}$$

For the DNA ordering of the first sequenced human chromosome 22 (Ch22), entitled NT_{011520}, the numbers of letters of this sequence is about 3.4×10^6 nucleotides (for a statistical study of this sequence see Ref. [135]). This sequence was retrieved from the internet page of the National Center of Biotechnology Information. The energies ϵ_n are chosen from the ionization potential of the respective bases, as given in Section 3.1. The hopping term t among the bases were also taken equal to 1 eV, while the hopping potential w due to the hydrogen bonds linking the two strands is considered to be 0.1 eV.

With the intention of comparing the quasiperiodic sequences FB and RS with the genomic one, we assume also that the energies ϵ_n take the values $\epsilon_G, \epsilon_A, \epsilon_C$, and ϵ_T, as in the DNA genomic sequence, with the same numerical values.

Fig. 3.5 shows the electron energy spectra, as measured by their equivalent bandwidth Δ (the sum of all allowed energy regions in the band structures), for the Fibonacci (Fig. 3.5(a)) and the Rudin–Shapiro (Fig. 3.5(b)) quasiperiodic sequences, as well as for the genomic DNA Ch22 (Fig. 3.5(c)), respectively, up to the number of nucleotides n equal to 93 in each unit cell N. This is nothing but the Lebesgue measure of the energy spectrum. From there, one can infer the forbidden and allowed energies as a function of the number of nucleotides n. Notice that, as expected, as n increases the allowed band regions get narrower and narrower, as an indication of more localized modes.

3.4. The extended double-strand DNA structure model

Consider now the so-called extended double-strand DNA model [136,137], as depicted in Fig. 3.6. It seems to be more appropriate to describe the DNA molecule than the simple double-strand DNA model discussed in the previous section, since the diagonal interstrand transfer matrix elements additionally presented are more relevant than the vertical intrastrand coupling [138–140]. Its tight-binding model Hamiltonian is given by [141]:

$$H = \sum_{j=1}^{2N} \epsilon_j |j\rangle\langle j| + \sum_{j=1}^{2(N-1)} t_{j,j+2} [|j\rangle\langle j+2| + |j+2\rangle\langle j|] + \sum_{j=1}^{N} t_{2j-1,2j} [|2j-1\rangle\langle 2j| + |2j\rangle\langle 2j-1|]$$

$$+ \sum_{j=1}^{N-1} \left[t_{2j-1,2j+2} (|2j-1\rangle\langle 2j+2| + |2j+2\rangle\langle 2j-1|) + t_{2j,2j+1} (|2j\rangle\langle 2j+1| + |2j+1\rangle\langle 2j|) \right], \tag{32}$$

where N is the number of DNA's base pairs, and ϵ_j is the ionization on-site energy representing the guanine ($j = G$), adenine ($j = A$), cytosine ($j = C$), and thymine ($j = T$) bases, respectively. Also, t_{nm} is the nonrandom hopping amplitudes. The long-range on-site energies used here are evaluated by using the density-functional theory (DFT), which depend on the flanking nucleobases [138]. It means that we average the 16 values for the on-site energy given in Ref. [138] for each nucleobases, as it was done in Ref. [137], in which the extended ladder model of DNA was proposed and studied. This yield $\epsilon_G = 8.178$, $\epsilon_A = 8.631$, $\epsilon_C = 9.722$, and $\epsilon_T = 9.464$ (all units in eV), slightly different from those used in the previous sections. The hopping parameters are listed in Table 1, where a single-strand sequence notation was used (the other strand is determined considering the DNA unique base pairing). Because of the directionality of DNA strands, $t_{5'-XY-3'} \neq t_{3'-XY-5'} = t_{5'-YX-3'}$ for $X \neq Y$. Furthermore, due to symmetry, $t_{5'-XY-5'} = t_{5'-YY-5'}$, and $t_{3'-XY-3'} = t_{3'-XY-3'}$ for all X, Y.

Fig. 3.5. Energy spectra for (a) Fibonacci DNA chain; (b) Rudin–Shapiro DNA chain; (c) human chromosome 22 (Ch22) DNA chain.

Fig. 3.6. (Color online) Schematic representation of an extended double-strand DNA molecule. Here the letters X, Y, X' and Y' represent the base pairs: guanine, adenine, cytosine, and thymine.

To evaluate the electronic density of states (DOS) it is necessary to rewrite the Hamiltonian (32) in matrix form as:

$$
H = \begin{pmatrix}
\epsilon_1 & t_{1,2} & t_{1,3} & t_{1,4} & & & & & & \\
t_{1,2} & \epsilon_2 & t_{2,3} & t_{2,4} & & & & & 0 & \\
t_{1,3} & t_{2,3} & \epsilon_3 & t_{3,4} & t_{3,5} & t_{3,6} & & & & \\
t_{1,4} & t_{2,4} & t_{3,4} & \epsilon_4 & t_{4,5} & t_{4,6} & \ddots & & & \\
 & & t_{3,5} & t_{4,5} & \epsilon_5 & t_{5,6} & \ddots & & & \\
 & & t_{3,6} & t_{4,6} & t_{5,6} & \epsilon_6 & \ddots & t_{N-3,N-1} & t_{N-3,N} & \\
 & & & \ddots & \ddots & \ddots & \ddots & t_{N-2,N-1} & t_{N-2,N} & \\
 & 0 & & & t_{N-3,N-1} & t_{N-2,N-1} & \epsilon_{N-1} & t_{N-1,N} & \\
 & & & & t_{N-3,N} & t_{N-2,N} & t_{N-1,N} & \epsilon_N &
\end{pmatrix} .
\tag{33}
$$

Table 1
Hopping parameters for the extended double-strand DNA structure (all energies are expressed in eV) [137,138].

X	Y			
	G	A	C	T
(a) $t_{5'-XY-3'} = t_{3'-YX-5'}$				
G	0.053	−0.077	−0.114	0.141
A	−0.010	−0.004	0.042	−0.063
C	0.009	−0.002	0.022	−0.055
T	0.018	−0.031	−0.028	0.180
(b) $t_{5'-XY-5'}$				
G	0.012	−0.013	0.002	−0.009
A	−0.013	0.031	−0.001	0.007
C	0.002	−0.001	0.001	0.0003
T	−0.009	0.007	0.0003	0.001
(c) $t_{3'-XY-3'}$				
G	−0.032	−0.011	0.022	−0.014
A	−0.011	0.049	0.017	−0.007
C	0.022	0.017	0.010	−0.004
T	−0.014	−0.007	−0.004	0.006

Based on Dean's negative eigenvalue theorem [142], the Schrödinger equation can be solved and the eigenvalue can be obtained exactly. The corresponding DOS is written as

$$\rho(E) = \lim_{N \to \infty} \frac{1}{N} \sum_k \delta(E - E_k). \tag{34}$$

Fig. 3.7 shows the DOS for several intra-strand (inter-strands) nucleobases couplings, taking into account the three different sequences: (a) Fibonacci, (b) Rudin–Shapiro and (c) human chromosome 22 (Ch 22).

Rather than traces of bands, the DOS profile for each structure is fragmented, showing a number of discrete strongly localized bunches of states that are believed to reflect their 1D band structure. Observe that the number of van Hove singularities is bigger for the RS and Ch22 structures than for the simplest Fibonacci one. Indeed, by inspecting Fig. 3.7, one can observe that for the Fibonacci case, there are two well defined regions around ϵ_G and ϵ_C, respectively. On the other hand, the Rudin–Shapiro and Ch22 structures have four regions centered roughly at the ionization energies of their nucleotides ϵ_G, ϵ_A, ϵ_C, and ϵ_T, respectively.

### 3.5. The sugar–phosphate backbone structure model

Now we consider the charge transport in a poly(dG)–poly(dC) DNA finite segment, taking into account its double-strand geometry, including the sugar–phosphate backbone. Our theoretical model is again based on a tight-binding Hamiltonian, within a Dyson's framework, together with a transfer matrix employed to simplify the algebra. The electronic density of states are calculated considering that the DNA molecule is sandwiched between two electrodes. Besides, it is arranged in a poly(dG)–poly(dC) geometry, following a Fibonacci (FB) quasiperiodic structures. The spectra are then compared with those found from a genomic DNA sequence, considering again a finite segment of the first sequenced human chromosome 22 (Ch 22).

Our model for the double-strand poly(dG)–poly(dC) DNA, including the contribution of the sugar–phosphate (SP) backbone, is depicted in Fig. 3.8. The tight-binding Hamiltonian is written in terms of a localized basis as [143]

$$\begin{aligned}
H = \sum_n &\Big[\epsilon_{SP}^n |n, 1\rangle \langle n, 1| + \epsilon_\alpha^n |n, 2\rangle \langle n, 2| + \epsilon_\beta^n |n, 3\rangle \langle n, 3| + \epsilon_{SP}^n |n, 4\rangle \langle n, 4| \Big] \\
&+ \sum_n \Big[w_{12}(\alpha \to SP)[|n, 1\rangle \langle n, 2| + |n, 2\rangle \langle n, 1|] \Big] \\
&+ \sum_n \Big[w_{23}(\alpha \to \beta)[|n, 2\rangle \langle n, 3| + |n, 3\rangle \langle n, 2|] \Big] \\
&+ \sum_n \Big[w_{34}(\beta \to SP)[|n, 3\rangle \langle n, 4| + |n, 4\rangle \langle n, 3|] + t_{SS}(|n, S\rangle \langle n, S|) \Big] \\
&+ \sum_n \Big[t_{11}(SP \to S)(|n, 1\rangle \langle n-1, 1|) + t_{44}(SP \to SP)(|n, 4\rangle \langle n \pm 1, 4|) \Big],
\end{aligned} \tag{35}$$
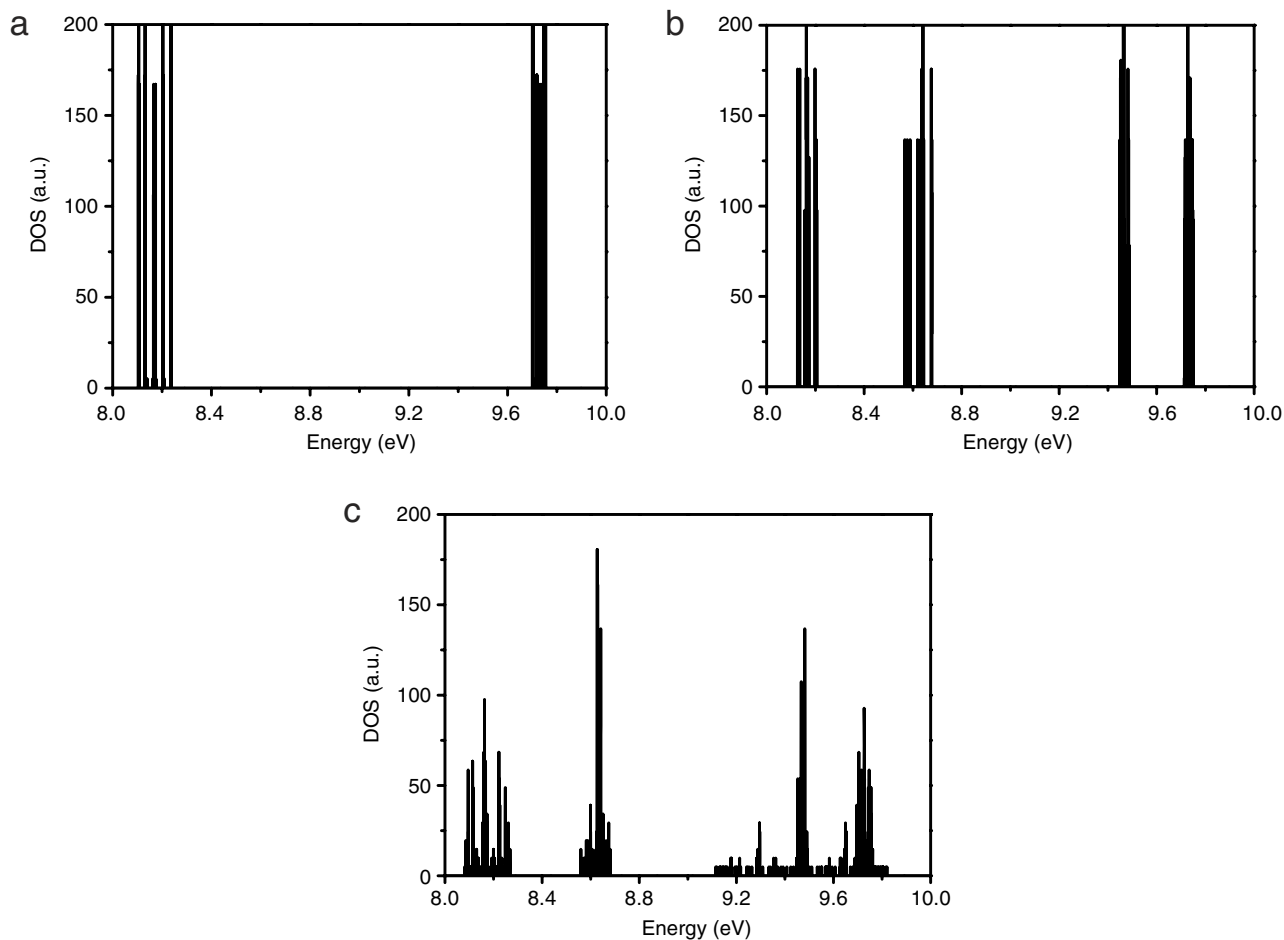
Fig. 3.7. The electronic density of states (DOS) in arbitrary units plotted against the energy E (in eV) for: (a) Fibonacci sequence; (b) Rudin–Shapiro sequence; (c) DNA human chromosome 22 (Ch22).
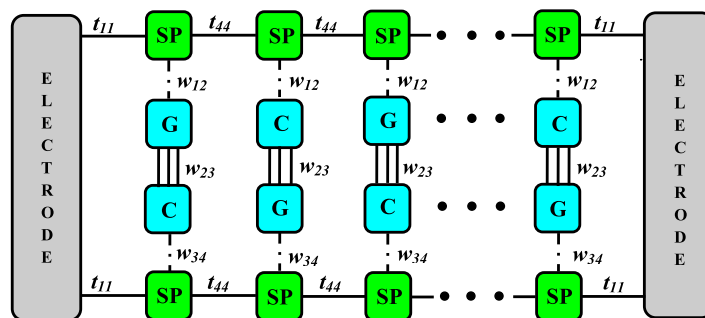
Fig. 3.8. (Color online) Schematic representation of a double-strand DNA molecule, including the sugar–phosphate contribution.

where ϵ_{SP}^{n} represents the single energy, in units of $\hbar$, at site n of the sugar–phosphate orbital, and with ϵ_{α}^{n} ($\alpha = C$ or G) being the ionization energy of the respective base α. Also $w_{12}(\alpha \rightarrow SP)$, $w_{23}(\alpha \rightarrow \beta)$ and $w_{34}(\beta \rightarrow SP)$ are the inter-chain first-neighbor electronic overlaps (hopping amplitude), with $\alpha, \beta = C$, or G, while t_{SS} is the hopping term in the electrodes. Besides, $t_{11}(SP \rightarrow S) = t_{S}$ and $t_{44}(SP \rightarrow SP) = t_{SP}$ are the intra-chain hopping amplitudes. Here, the letter S means the electrode (considered, as before, a platinum metal), while SP means the sugar–phosphate backbone.

To model a DNA segment, we consider a quasiperiodic chain of Fibonacci type, starting with a G (guanine) base as seed. It can now be built in a similar way, as described in Section 3.1, through the inflation rules $G \rightarrow GC$ and $C \rightarrow G$ for the first strand. For the second strand, we have complementary bases, in such a way that we always have a GC or a CG base pair.

For the first generation of the FB sequence, in which only a guanine base is linked to the electrodes, the Dyson equation leads to:

$$G(\epsilon)^{-1} = K_{G} + 2\Gamma(1), \tag{36}$$

where

$$\Gamma(1) = -L_{SPS}[K_S + L_S T]^{-1} L_{SPS}. \tag{37}$$

Here T is a transfer matrix linking the Green functions of two next-neighbors sites. Also, $L_S = -t_{SS}I$, I being a 4×4 identity matrix, and K_G, K_S, L_{SPS} are matrices given by

$$K_G = \begin{bmatrix} \epsilon - \epsilon_{SP} & -w_{12}(G \to SP) & 0 & 0 \\ -w_{12}(G \to SP) & \epsilon - \epsilon_G & -w_{23}(G \to C) & 0 \\ 0 & -w_{23}(G \to C) & \epsilon - \epsilon_C & -w_{34}(C \to SP) \\ 0 & 0 & -w_{34}(C \to SP) & \epsilon - \epsilon_{SP} \end{bmatrix}, \tag{38}$$

$$K_S = \begin{bmatrix} \epsilon - \epsilon_S & -t_{SS} & 0 & -t_{SS} \\ -t_{SS} & \epsilon - \epsilon_S & -t_{SS} & 0 \\ 0 & -t_{SS} & \epsilon - \epsilon_S & -t_{SS} \\ -t_{SS} & 0 & -t_{SS} & \epsilon - \epsilon_S \end{bmatrix}, \tag{39}$$

$$L_{SPS} = \begin{bmatrix} -t_S & 0 & 0 & 0 \\ 0 & 0 & 0 & 0 \\ 0 & 0 & 0 & 0 \\ 0 & 0 & 0 & -t_S \end{bmatrix}. \tag{40}$$

Repeating the procedure for any Fibonacci generation, we get:

$$G(\epsilon)^{-1} = K_G + \Gamma(1) + \Lambda(n_{FB}), \tag{41}$$

where n_{FB} is the number of nucleotides in the strand. Here

$$\Lambda(n_{FB}) = -L_{SPSP}[K_i + \Lambda(n_{FB} - 1)]^{-1} L_{SPSP}, \tag{42}$$

whose initial condition is:

$$\Lambda(1) = -L_{SPS}[K_S + L_S T]^{-1} L_{SPS}. \tag{43}$$

We will now turn our discussion to the determination of the electronic density of state (DOS), as given in Eq. (20). The energies $\epsilon_{\alpha,\beta}$ are again chosen from the ionization potential of the respective bases, i.e., $\epsilon_G = 7.77$ eV (guanine), and $\epsilon_C = 8.87$ eV (cytosine). Also, we use the energy of the sugar–phosphate backbone as $\epsilon_{SP} = 12.27$ eV, while the hopping term between the base pair is $w_{23}(G \to C) = 0.90$ eV [144]. The hopping potentials between the base (G or C) and the sugar–phosphate (SP) backbone is $w_{12}(G \to SP) = w_{34}(C \to SP) = 1.5$ eV [133]. Finally, the hopping potential between the sugar–phosphate backbone, is $t_{SP} = 0.02$ eV [133].

The electronic density of states (DOS) spectrum, considering the DNA molecule modeled by the quasiperiodic Fibonacci sequence, is shown in Fig. 3.9 as a function of the energy (in eV), for a Fibonacci's generation numbers $N_{FB} = 12$ and $n_{FB} = 610$. Here N_{FB} means the sequence generation number, while n_{FB} corresponds to the number of nucleotides in a given sequence generation. For comparison, we are showing segments of natural DNA, as part of the human chromosome Ch22 (dashed lines), whose spectra depict a strike agreement with those modeled by the Fibonacci sequence. Although the DOS for each generation as a whole does not show any symmetry, it presents for the spectrum depicted here (Fibonacci and Ch22) two symmetrical regions, located around the frequencies 7.03 eV (peak I), and 15.35 eV (peak III), respectively, besides an asymmetrical one around 9.03 eV (peak II). Although the peak I does not have a direct correlation with the ionization energies of the bases (guanine and cytosine), its frequency value is near the hopping term in the interface DNA–electrode, suggesting an important influence for the choice of the electrodes on the DOS properties of the DNA. The peak II has a strong correlation with the ionization energy of cytosine, which is around 9 eV. This result is interesting because shows that while the amount of cytosine in the FB generations as well as in the first sequenced human chromosome Ch22, is less than the guanine one, its bigger ionization energy makes a difference regarding the electronic DOS of the whole system. The third peak (peak III), occurs to an amount approximately equal to twice the ionization energy of guanine. We can also observe an anomaly in the spectrum around 10.6 eV, which is twice the value of the ionization energy of the electrode ϵ_S. Moreover, the DOS in each level of energy increases with the Fibonacci generation for the intervals (in units of eV) $5.36 < \epsilon < 15.98$, approximately. Note that this interval is comprised between the ionization energy of the electrode ϵ_S and twice the ionization energy of the guanine ϵ_G. However, around 12.5 eV, we observed that the DOS is almost null for both FB and Ch22 case. This result may be related to the hopping term of the electrode and/or to the ionization energy of the sugar–phosphate, which are both around 12 eV.

3.6. Renormalization approach

So far we have assumed the electronic transport in DNA molecules throughout a transmission channel along their longitudinal axis through a π-stacked array of DNA nucleobases, formed by the four nucleotides A, T, G, and C. Further improvements in this model includes the backbone structure of the DNA molecule explicitly, which reduces the DNA base
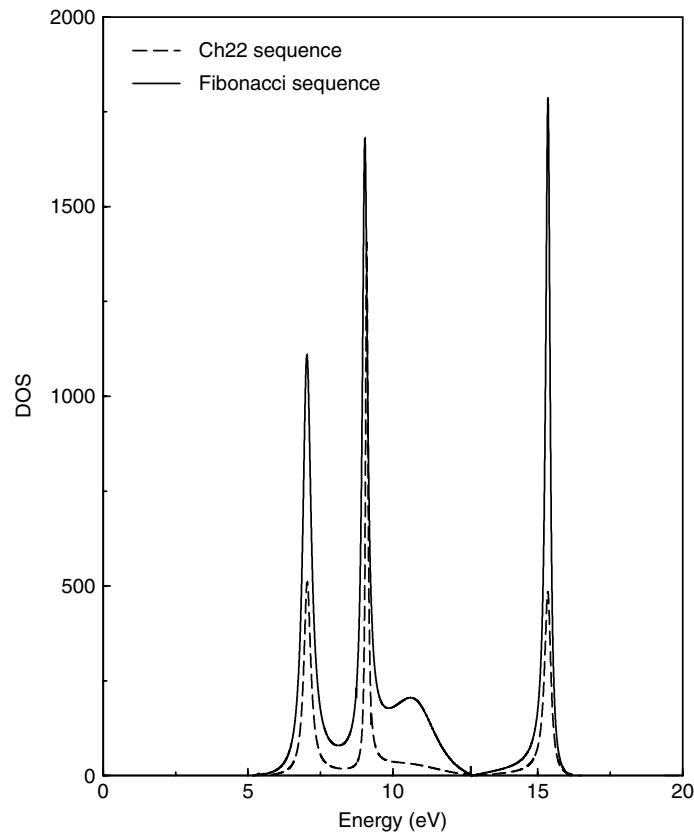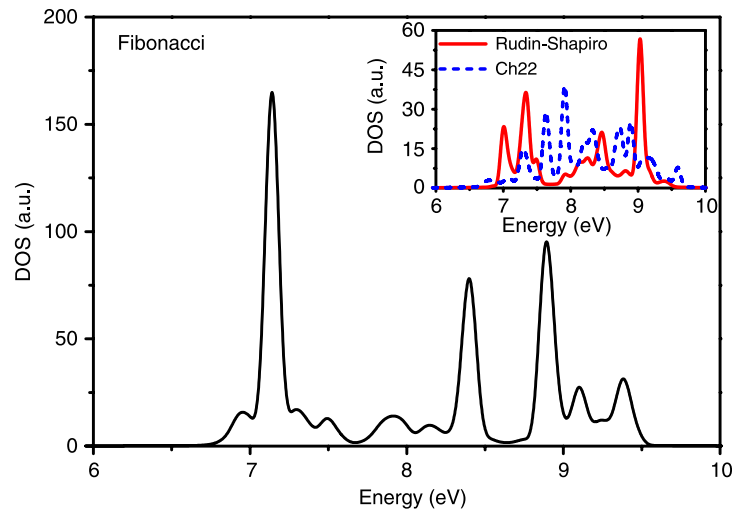
Fig. 3.9. Electronic density of state (DOS) spectra, as a function of the energy (in eV), for the 14th generation number Fibonacci poly(dG)–poly(dC) DNA double-strand model, corresponding to the number of nucleotides $n_{FB} = 610$ (full line). For comparison we are showing also the DOS of a segment of natural DNA, as part of the human chromosome Ch22 (dashed lines).
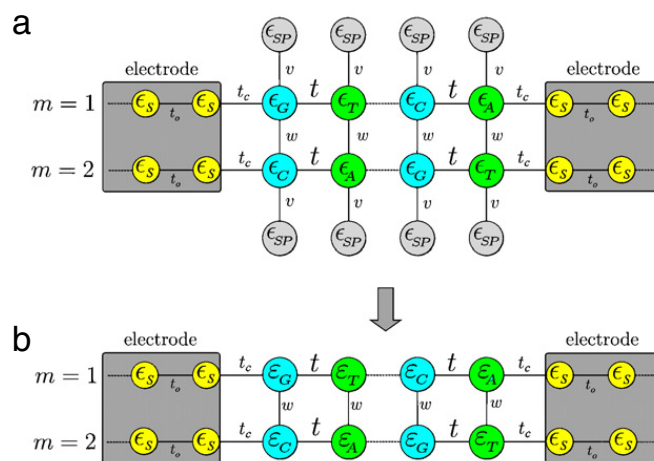
Fig. 3.10. (Color online) Sketch illustration of the renormalization process mapping the DBL-DNA chain model into a linear diatomic lattice. Three different hopping integrals are considered: the intrastrand term (t), the interstrand term (w), and the coupling between the sugar–phosphate backbone and the base pairs (v), respectively. (a) starting effective tight-binding model for the Fibonacci and Rudin–Shapiro sequence for a DBL-DNA model; (b) renormalized model of the DBL-DNA molecule after the first decimation step.

pair architecture into a single site per pair, the so-called fish bone model [145]. Later, Klotsa et al. [146] generalized the fishbone DNA model considering each base as a distinct site, weakly coupled by hydrogen bonds. As a consequence, two central branches are thus obtained, whose interconnected sites represent the DNA base pairs; they are coupled to upper and lower disconnected backbone sites, giving rise to the so-called dangling backbone ladder (DBL)-DNA model.

Taking into account these latest developments, in this subsection we use a model Hamiltonian within a one-step renormalization approach to describe the charge transport properties of a DBL-DNA molecule (see Fig. 3.10). Our description of the DNA molecule considers the contributions of the nucleobase system as well as the sugar–phosphate backbone molecules. We consider a DBL-DNA model following a Fibonacci (FB) and a Rudin–Shapiro (RS) quasiperiodic basis arrangement, as well as the DNA sequence of the first sequenced human chromosome 22 (Ch22) for the sake of comparison.

Fig. 3.11. The electronic density of states (DOS) in arbitrary units plotted against the energy E (in eV) for the DBL-DNA model considering the Fibonacci quasiperiodic sequences with the number of nucleotides $n_{FB} = 34$ (full line-black). In the inset we show also the electronic density of states for the Rudin–Shapiro quasiperiodic sequences, with $n_{RS} = 32$ (full line-red), and a segment of natural DNA, as part of the human chromosome Ch22, whose number of nucleotides $n_{Ch22} = 32$ (dotted line-blue). (For interpretation of the references to colour in this figure legend, the reader is referred to the web version of this article.)

The resulting variations of the charge transport efficiency are analyzed, in these sequences, by numerically computing the main features of their electron transmittance coefficients.

The tight-binding Hamiltonian for a DBL-DNA molecule describes one electron moving in a geometry composed by two interconnected chains of sites sandwiched by two metallic electrodes (donor−DN, acceptor−AC), with a single orbital per site and nearest-neighbor interactions, yielding

$$H_{total} = H_{DNA} + H_{electrode} + H_{coupling}. \tag{44}$$

In order to get a simple mathematical description of the DBL-DNA molecule, keeping most of its relevant physical information, we use now a one-step renormalization process to map the DBL-DNA chain into a linear diatomic lattice (see Fig. 3.10). This model allow us to incorporate the sugar–phosphate backbone contribution into an energy-dependent on-site ionization potential in the main DNA's base pairs, whose renormalized site energies are given by [146,147]:

$$\varepsilon_{\alpha,\beta}^{n} = \epsilon_{\alpha,\beta}^{n} + t_{\alpha,SP}(\alpha \rightarrow SP)^2/(E - \epsilon_{SP}^{n}). \tag{45}$$

Here, $\epsilon_{\alpha,\beta}^{n}$ ($\alpha, \beta = C, G, A$ or T) is the ionization energy (in units of $\hbar$) of the respective base α, β; $t_{\alpha,SP}(\alpha \rightarrow SP)$ are the hopping potentials between the base α (G, C, A or T) and the sugar–phosphate (SP) backbone; finally, ϵ_{SP}^{n} represents the single energy at site n of the sugar–phosphate orbital, taking into account the nature of the neighborhood base, as well as the presence of water molecules and/or counterions attached to the backbone.

Considering the renormalization procedure, the first term of the Hamiltonian (44) can be given by [148]

$$H_{DNA} = \sum_{n}[\epsilon_{\alpha}^{n}|n, 1\rangle\langle n, 1| + \epsilon_{\beta}^{n}|n, 2\rangle\langle n, 2|] + \sum_{n} w(\alpha \rightarrow \beta)[|n, 1\rangle\langle n, 2| + |n, 2\rangle\langle n, 1|]$$

$$+ \sum_{n} t(\alpha \rightarrow \alpha)[|n, 1\rangle\langle n \pm 1, 1|] + \sum_{n} t(\beta \rightarrow \beta)[|n, 2\rangle\langle n \pm 1, 2|]. \tag{46}$$

The second term, related to the two semi-infinite metallic electrodes, reads:

$$H_{electrode} = \sum_{n=-\infty}^{0}\sum_{m=1}^{2}[\epsilon_{S}^{n}|n, m\rangle\langle n, m| + t_0|n, m\rangle\langle n \pm 1, m|]$$

$$+ \sum_{n=N+1}^{\infty}\sum_{m=1}^{2}[\epsilon_{S}^{n}|n, m\rangle\langle n, m| + t_0|n, m\rangle\langle n \pm 1, m|]. \tag{47}$$

Our DNA molecule is coupled to the electrodes by the tunneling Hamiltonian

$$H_{coupling} = \sum_{m=1}^{2} t_c[|0, m\rangle\langle 1, m| + |n, m\rangle\langle n + 1, m|], \tag{48}$$

where $t_c = \sqrt{tt_0}$ represents the hopping amplitude between the AC (DC) electrode and the beginner (end) of the DNA base-pair structure [145].

The electronic density of states (DOS in arbitrary units) spectra are depicted in Fig. 3.11 as a function of the energy in units of eV. We have considered the four nucleotides arranged in a quasiperiodic fashion following a Fibonacci sequence (full line in black with $n_{FB} = 34$ nucleotides). In the inset, we consider the Rudin–Shapiro one (full line in red with $n_{RS} = 32$ nucleotides), as well as the spectrum for the human chromosome Ch22 (dotted line in blue, with $n_{Ch22} = 32$ nucleotides). It is relevant to stress that the presence of long-range correlations in the disorder distribution is a possible mechanism to induce delocalization in low dimensional systems [149]. However, the actual correlations in our model (hopping mechanism) are not strong enough to produce this correlation-induced transition, and the stationary states remain all localized. Nevertheless, the presence of long-range correlations enhances the localization length and, therefore, the DOS spectra, as shown in Fig. 3.11, survive in larger segments as compared with a non-correlated random sequence. Observe also that the DOS for long-range correlated Rudin–Shapiro sequences, depicts a trend similar to the one produced by the genomic Ch22 sequence.

4. Electrical conductivity

Electron transmission conductivity through molecules (such as DNA) and molecular interfaces has been a subject of intensive research nowadays, which is due to the scientific/technological interest in electron-transfer phenomena underlying the operation of the scanning-tunneling microscope on one hand, and in the transmission properties of molecular bridges between conducting leads on the other [150]. In view of that, the traditional molecular assumption of electron transfer, in which their rates depend on the donor and acceptor electrodes properties, on the solvent, and on the electronic coupling between the states involved, gives rise to a novel approach of the molecule as a current-carrying conductor whose observables, such as electron-transfer rates and yields, are being replaced by their conductivities, or more generally by their current–voltage ($I \times V$) profiles. Such investigations of electrical junctions, in which single molecules or small molecular assemblies operate as conductors, constitute a major part of the new field now called molecular electronics.

Electron conductivity properties though DNA are still controversial, mainly due to the tremendous difficulties in setting up the proper experimental environment and the DNA molecule itself. Despite the lack of a consistent picture, many theoretical explanations for the charge transport phenomena have been suggested so far on the basis of the standard solid-state-physics approach such as polarons, solitons, hole hopping model on guanine sites [151], but the situation has been still far from unifying the theoretical scheme. For instance, recently the electric conductance of DNA molecules was studied using a tight-binding small polaron model and the length dependence of the electric current was derived [152], whose main conjecture was that the drift of polarons states may lead to a rapid motion of charges introduced on DNA [153].

From the experimental side, one of the main problem is how to attach proper electrodes to the single DNA molecule, in order to avoid that any recorded conductivity comes from the molecule itself, and not from some residual conductivity in the surrounding medium. Therefore, it is mandatory to provide reliable electrical contacts to the DNA molecule which neither do not allow any electron transfer reactions through the ionic medium surrounding the molecule, nor getting noise from other means.

4.1. Electronic transmission spectra

Consider the DNA model described in Section 3.6, further assumed connected to two semi-infinite electrodes, whose energies ϵ_m are adjusted to simulate a resonance with the guanine highest occupied molecular orbital (G-HOMO) energy level, i.e., $\epsilon_m = \epsilon_G$. For this system, the transmission coefficient $T_N(E)$, that gives the transmission rate through the chain and is related with the Landauer resistance, is defined by [154]:

$$T_N(E) = [|T_1|^2 + |T_2|^2]/2, \tag{49}$$

where T_1 (T_2), is given by

$$T_1(T_2) = N_1(N_2)/D. \tag{50}$$

Here,

$$
\begin{aligned}
N_1 = (&r_{33}r_{11}r_{22} - r_{33}r_{12}r_{21} + r_{34}r_{11}r_{22} - r_{34}r_{12}r_{22} - r_{31}r_{22}r_{13} + r_{31}r_{12}r_{23} \\
&- r_{31}r_{22}r_{14} + r_{31}r_{12}r_{24} + r_{32}r_{21}r_{13} - r_{32}r_{11}r_{23} + r_{32}r_{21}r_{14} - r_{32}r_{11}r_{24}),
\end{aligned} \tag{51}
$$

$$
\begin{aligned}
N_2 = (&r_{43}r_{11}r_{22} - r_{43}r_{12}r_{21} + r_{44}r_{11}r_{22} - r_{44}r_{12}r_{21} - r_{41}r_{22}r_{13} + r_{41}r_{12}r_{23} \\
&- r_{41}r_{22}r_{14} + r_{41}r_{12}r_{24} + r_{42}r_{21}r_{13} - r_{42}r_{11}r_{23} + r_{42}r_{21}r_{14} - r_{42}r_{11}r_{24}),
\end{aligned} \tag{52}
$$

$$D = (r_{11}r_{22}) - (r_{12}r_{21}). \tag{53}$$

In the above equations, r_{ij} are the components of the 4×4 matrix $\mathcal{R}$, defined as $\mathcal{R} = \Theta^{-1}S^{-1}PS$, with:

$$
\Theta =
\begin{pmatrix}
e^{-ikNa} & 0 & 0 & 0 \\
0 & e^{-ikNa} & 0 & 0 \\
0 & 0 & e^{ikNa} & 0 \\
0 & 0 & 0 & e^{ikNa}
\end{pmatrix}, \tag{54}
$$

$$S = \begin{pmatrix} e^{-ika} & 0 & e^{ika} & 0 \\ 0 & e^{-ika} & 0 & e^{ika} \\ 1 & 0 & 1 & 0 \\ 0 & 1 & 0 & 1 \end{pmatrix},$$

(55)

where k is given by

$$k = \cos^{-1}[(E - \epsilon_S)/2t_0].$$

(56)

Also, $P = M_R(\prod_{n=N}^{1} M_n)M_L$, where the M's matrices are given by

$$M_n = \begin{pmatrix} (E - \varepsilon_\alpha^n)/t & -w/t & -1 & 0 \\ -w/t & (E - \varepsilon_\beta^n)/t & 0 & -1 \\ 1 & 0 & 0 & 0 \\ 0 & 1 & 0 & 0 \end{pmatrix},$$

(57)

$$M_l = \begin{pmatrix} (E - \epsilon_S)/t_c & 0 & -t_0/t_c & 0 \\ 0 & (E - \epsilon_S)/t_c & 0 & -t_0/t_c \\ 1 & 0 & 0 & 0 \\ 0 & 1 & 0 & 0 \end{pmatrix},$$

(58)

$$M_R = \begin{pmatrix} (E - \epsilon_S)/t_0 & 0 & -t_c/t_o & 0 \\ 0 & (E - \epsilon_S)/t_0 & 0 & -t_c/t_0 \\ 1 & 0 & 0 & 0 \\ 0 & 1 & 0 & 0 \end{pmatrix}.$$

(59)

The transmission coefficients $T_N(E)$, as given by Eq. (49), are depicted in Fig. 4.1 as a function of the energy (in units of eV). We have considered the four nucleotides arranged in a quasiperiodic fashion, either following a Fibonacci sequence (with $n_{FB} = 34$ nucleotides) or a Rudin–Shapiro one (with $n_{RS} = 32$ nucleotides), respectively, both showing a long-range pair-correlation. For comparison, we also show the spectrum for the human chromosome Ch22 (with $n_{Ch22} = 32$ nucleotides). The transmission bands in the spectrum are fragmented, which is related to the localized nature of the electrons eigenstates in disordered chains, and reflects the number of passbands in each structure. It is relevant to stress that the presence of long-range correlations in the disorder distribution is a possible mechanism to induce delocalization in low dimensional systems [149]. However, the actual correlations in our model (hopping mechanism) are not strong enough to produce this correlation-induced transition, and the stationary states remain all localized. Nevertheless, the presence of long-range correlations enhances the localization length and, therefore, the transmission resonances, as shown in Fig. 4.1, survive in larger segments as compared with a non-correlated random sequence. Observe also that the transmission coefficient for long-range correlated Rudin–Shapiro sequences depicts a trend similar to the one produced by the genomic Ch22 sequence.

4.2. Current–voltage characteristic curves

The transmission coefficient is a useful quantity to describe the transport efficiency in quantum systems. Nonetheless, $T_n(E)$, as discussed in Section 4.1, is usually difficult to be directly measured experimentally [155,156]. Access to transmission properties can be performed by measuring their I–V characteristics. With the tight-binding Hamiltonian given before, one can evaluate the I–V characteristics by applying the Landauer–Büttiker [157,158] formulation [154]:

$$I(V) = (2e/h) \int_{-\infty}^{+\infty} T_N(E)[f_{DN}(E) - f_{AC}(E)]dE,$$

(60)

where the Fermi–Dirac distribution is

$$f_{DN(AC)} = [\exp[(E - \mu_{DN(AC)})/k_B T] + 1]^{-1}.$$

(61)

Also, $\mu_{DN(AC)}$ is the electrochemical potential of the two leads (donor—DN and acceptor—AC) fixed by the applied bias voltage V as

$$|\mu_{DN} - \mu_{AC}| = eV.$$

(62)

The current onset is crucially dependent on the electrochemical potentials of the electrodes, that can be altered by the coupling to molecules [159]. For simplicity, before bias voltage is applied, the electrochemical potential of the whole system is taken to be zero. It is important to emphasize that the transmittance $T_n(E)$ should be calculated in the forward and backward applied electric field direction.

For a double-strand DNA sequences, as described in Section 3.2, the current–voltage characteristics are plotted in Fig. 4.2 for Fibonacci (Fig. 4.2(a)), Rudin–Shapiro (Fig. 4.2(b)), the random case (Fig. 4.2(c)) and the human chromosome Ch22 (Fig. 4.2(d)), respectively [160]. We are assuming a linear voltage drop across the DNA molecules by means of the usual expression, numerically computed near zero temperature, as given by Eq. (62). To reproduce the potential mismatch at zero bias, the energy difference between the guanine HOMO energy level and the metallic Fermi level of the electrode is set to
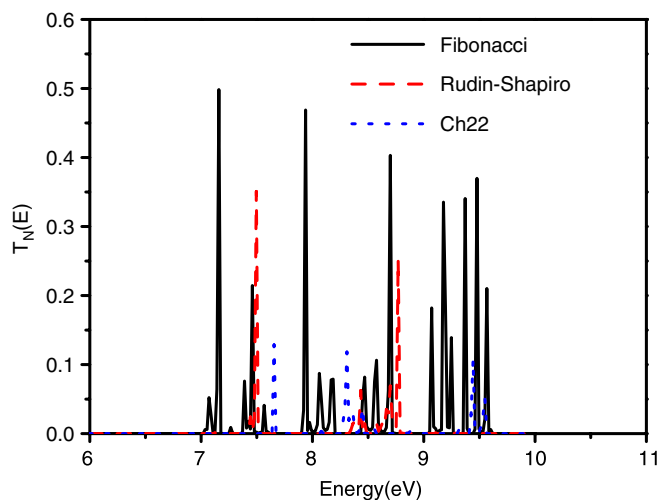
Fig. 4.1. Transmission coefficient $T_N(E)$ as a function of the energy E (in units of eV) for the DBL-DNA model considering the Fibonacci and Rudin–Shapiro quasiperiodic sequences, whose number of nucleotides $n_{FB} = 34$ (full line-black) and $n_{RS} = 32$ (dashed line-red), respectively. For comparison, we are showing a segment of natural DNA, as part of the human chromosome Ch22, whose number of nucleotides $n_{Ch22} = 32$ (dotted line-blue). (For interpretation of the references to colour in this figure legend, the reader is referred to the web version of this article.)
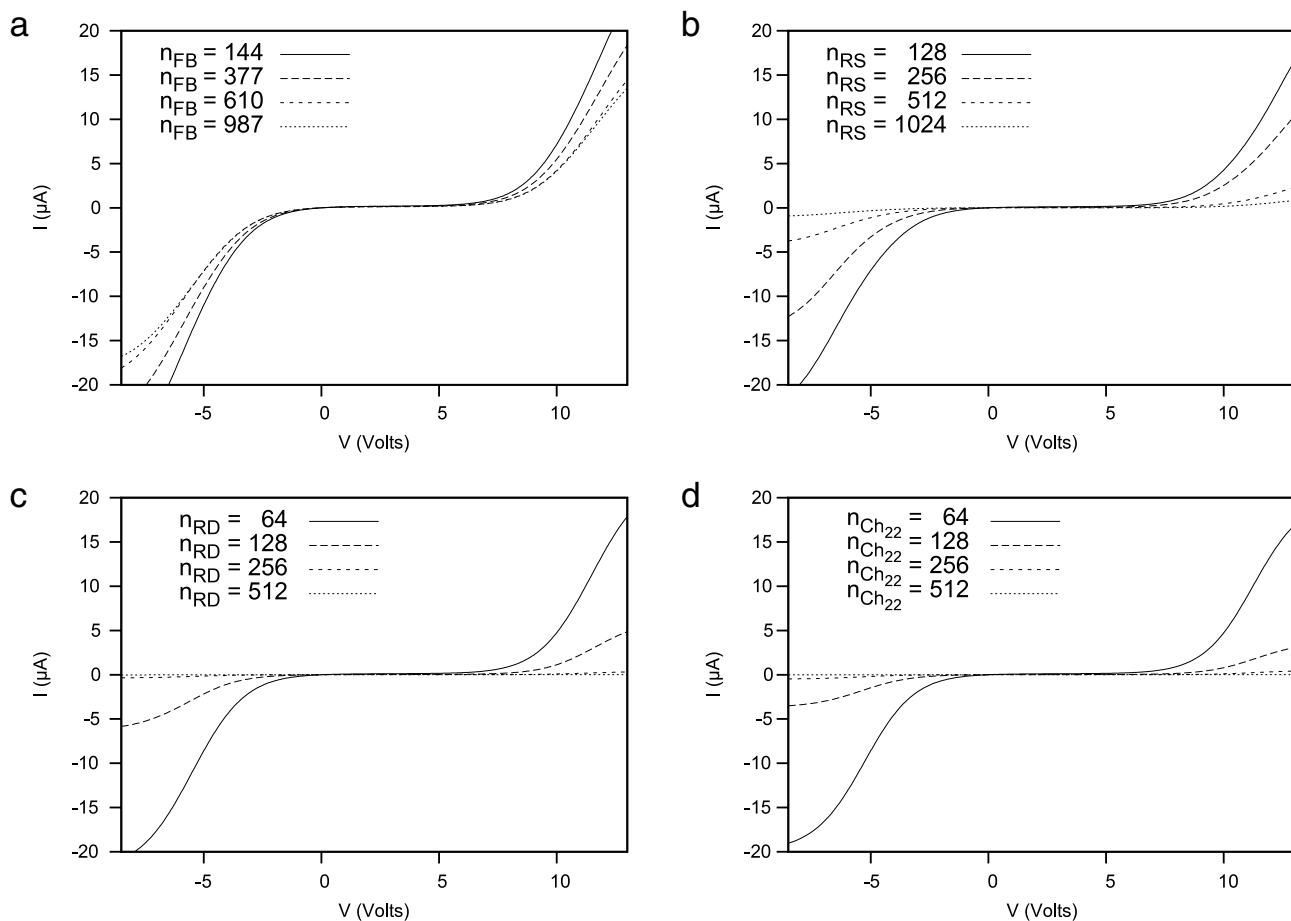
Fig. 4.2. Current–voltage ($I \times V$) characteristics of a double-strand DNA finite segment considering different numbers of nucleotides for (a) Fibonacci sequence; (b) Rudin–Shapiro sequence; (c) the random case; (d) the human chromosome Ch22, respectively.

1.2 eV [161]. As the voltage drop is switched on, the transmission coefficient $T_N(E)$ becomes voltage-dependent, resulting in transmission band shifts (shown in Fig. 4.2 for all cases studied here), which in turn lead to a voltage threshold modulation.

To extract the main features of the tunneling currents in DNA chains, let us compare the behavior of the genomic Ch22 (Fig. 4.2(d)) with those characterizing the quasiperiodic and random structures (Fig. 4.2(a), (b) and (c)) under the resonance condition given by the hopping term choice $t_{nm} = 1$ eV. In this case, if the potential barrier between the metallic contacts and the DNA is set to zero, a staircase in the plot I–V is found [162].

As soon as a potential barrier between the DNA and the metals is introduced (1.2 eV), the I–V characteristic curves show the profiles depicted in Fig. 4.2. The current threshold at a given voltage scale is not sensitive in respect to the different structures considered here, mainly due to the electronic correlations presented by the structures. However, such correlations shall depend strongly on the intra-chain coupling, and further studies considering more realistic model parameters would be needed in order to infer about the actual relevance of this threshold enhancement in DNA molecules. Observe the striking agreement between the I–V characteristic curves for the random and the genomic Ch22 case. Such agreement can be accounted by the short-range pair correlations shared by them, suggesting that the inclusion of just first-neighbors intra-strand pair correlations on the nucleotide distribution may provide an adequate description of the DNA electronic properties.

On the other hand, the current–voltage characteristics of the DBL-DNA model (see Section 3.6) are plotted in Fig. 4.3 for the Fibonacci (black full line), Rudin–Shapiro (red dashed line), and the human chromosome Ch22 (blue dotted line) simulations, respectively. In this case, there is a characteristic Ohmic region for $-5.0 \leq V_{bias} \leq +5.0$ eV, and nonlinear regions indicating transitions toward current saturation for $V_{bias} < -5.0$ eV and $V_{bias} > +5.0$ eV. The inset in Fig. 4.3 shows the transconductance $dI/dV \times V$ of the devices, which are highly nonlinear. All of them have semiconductors characteristics, as in the double-strand case depicted in Fig. 4.2.

4.3. Diluted base-pairing

A very instructive model that unveils the special role played by correlations in the electronic properties of DNA-based structures incorporates diluted base-pairing. In this model, we consider poly(CG) and poly(CT) segments at which guanine bases (G) are attached laterally at a fraction of the cytosine (C) bases. Within a tight-binding description, the density of states and eigenfunctions of the one-electron states can be mapped onto that of the Anderson chain with diluted disorder. As such, the influence of the effective disorder on the nature of the one-electron states, as well as on the wave-packet dynamics, can be explored. In particular, base pairing dilution indeed leads to a complete exponential localization of all one-electron states in segments formed with complementary units [as in poly(CG)]. On the other hand, a resonant state is not affected by disorder and remains extended in chains with non-complementary units [as in poly(CT)]. In the presence of such resonant state, the wave-packet develops a diffusive dynamics.

The theoretical framework makes use of an effective tight-binding Hamiltonian describing one electron moving in a geometry composed of a periodic chain of alternate bases (CG or CT sequences) [163]. The model assumes that G bases are laterally attached to C sites at random with probability p (see Fig. 4.4), taking into account just a single orbital per site and nearest-neighbor transfer integrals t (along the main chain) and w (among paired bases). The corresponding time-independent Schrödinger equation for a poly(CG) sequence is given by:

$$E\psi_j^G = t(\psi_{j-1}^C + \psi_{j+1}^C) + \epsilon_G \psi_j^G \quad \text{for odd } j, \tag{63}$$

$$E\psi_j^C = t(\psi_{j-1}^G + \psi_{j+1}^G) + w\beta_j \psi_j^G + \epsilon_C \psi_j^C, \quad \text{for even } j. \tag{64}$$

For a poly(CT), G is replaced by T. Here ϵ_α ($\alpha = G, T$ or C) represents the on-site potential at the bases G, T or C, and ψ_j^α is the wave-function coefficient in the single orbital basis, defined by

$$|\Psi\rangle = \sum_{(j,\alpha)} \psi_j^\alpha |j, \alpha\rangle, \tag{65}$$

where (j, α) runs over all base units. Also, $\beta_j = 1$ with probability p and $\beta_j = 0$ with probability $1 - p$, where p is the concentration of G sites attached to the single stranded main periodic chain. At the sites where $\beta_j = 1$, there is an additional equation:

$$E\psi_j^G = w\psi_j^C + \epsilon_G \psi_j^G, \tag{66}$$

for even j.

A clear picture of the nature of the electronic states on the above model is achieved after performing a decimation procedure of the attached base units. The above tight-binding model for a DNA-based molecule is mapped onto an effective one-dimensional diluted Anderson model [164–167]. Such model contains a diagonal disorder diluted by an underlying periodicity. The resulting sequence is composed of two inter-penetrating sub-lattices, one composed of random potentials (Anderson chain), while the other has non-random segments.

The degrees of freedom associated with the lateral DNA bases appearing in the above equations are removed by substituting
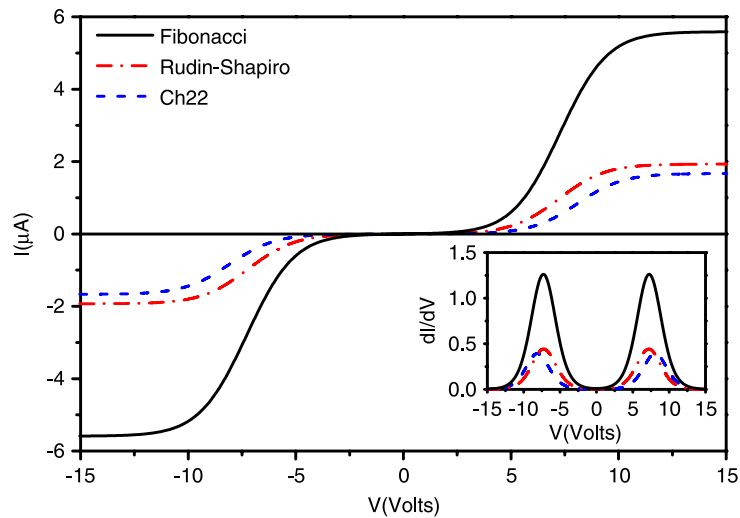
$$\psi_j^G = [w/(E - \epsilon_G)]\psi_j^C, \quad \text{for even } j, \tag{67}$$

into the equation for the coefficients ψ_j^C, yielding:

$$E\psi_j^C = \epsilon_C^* \psi_j^C + t(\psi_{j-1}^G + \psi_{n+1}^G), \tag{68}$$

where

$$\epsilon_C^* = \epsilon_C + [w^2/(E - \epsilon_G)] \tag{69}$$

Fig. 4.3. Current–voltage ($I \times V$) characteristics of a DBL-DNA sequences for (a) Fibonacci sequence (full line-black); (b) Rudin–Shapiro sequence (dashed line-red); (c) the human chromosome Ch22 (dotted line-blue), respectively. The inset shows the differential conductance dI/dV versus the voltage V of the devices. (For interpretation of the references to colour in this figure legend, the reader is referred to the web version of this article.)
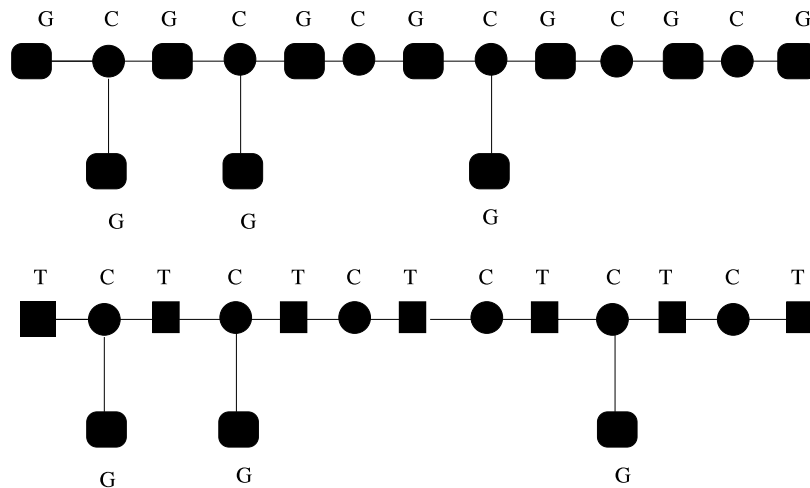

Fig. 4.4. Schematic representation of the single-strand DNA molecule showing the main periodic chains of alternate bases (CG and CT sequences) with diluted base pairing. Guanine (G) bases are laterally attached at random to a fraction p of the cytosine (C) sites.

is the renormalized potential at the cytosine sites at which the G bases are laterally attached. For those cytosine bases with no lateral attachment, the potential remains the bare one.

After eliminating the coefficients associated with the lateral G bases, the remaining set of equations expresses an alternate sequence of CG (or CT) nucleotides. The C sites have two possible values for the on-site potential, namely ϵ_C^* with probability p or ϵ_C with probability $1 - p$, respectively. The remaining bases of the periodic sequence have all the same potential: ϵ_G for poly(CG) or ϵ_T for poly(CT).

The random character of the diluted base-pairing is reflected in a random sequence for the effective on-site energies of the cytosine sites. This kind of sequence is similar to the structure so-called diluted Anderson model. It consists of two inter-penetrating sequences: a periodic sequence containing the guanine or thymine sites, for poly(CG) or poly(CT) respectively, and a random sequence containing bare and renormalized cytosine sites. Due to the periodicity of the non-random sub-lattice, a special resonance energy E_0 appears with vanishing wave-function amplitudes on the random sub-lattice. Therefore, this mode is mainly insensitive to the presence of disorder, and may lead to a possible mechanism to induce conductance in such DNA-based molecules. For the poly(CT) molecule, the resonance energy is $E_0 = \epsilon_T$. At this energy, the renormalized cytosine potential remains finite, leading to a divergence of the localization length of the one-electron eigenmodes, as the resonance energy is approach. On the other hand, the resonance energy for poly(CG) molecules is $E_0 = \epsilon_G$, in which the renormalized cytosine potential diverges. This case corresponds to an effectively infinite disorder which counteracts the delocalization effect. As a consequence, diluted base-pairing induces a stronger localization of the one-electron eigenfunctions in poly(CG) than in poly(CT) structures.

The spectrum of the Lyapunov exponent $\gamma(E)$ (which is the inverse of the localization length) of long DNA segments nicely illustrates the above described features. The Green's function recursion method based on Dyson's equation (see
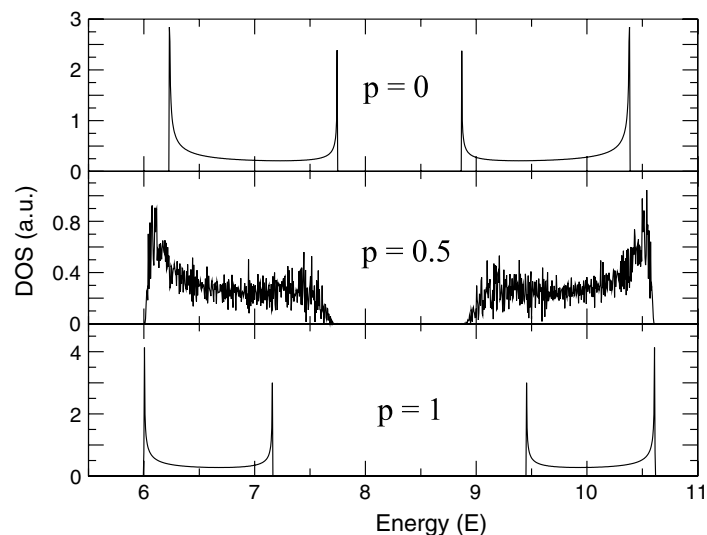
(a) CG sequence ($N = 10^5$).
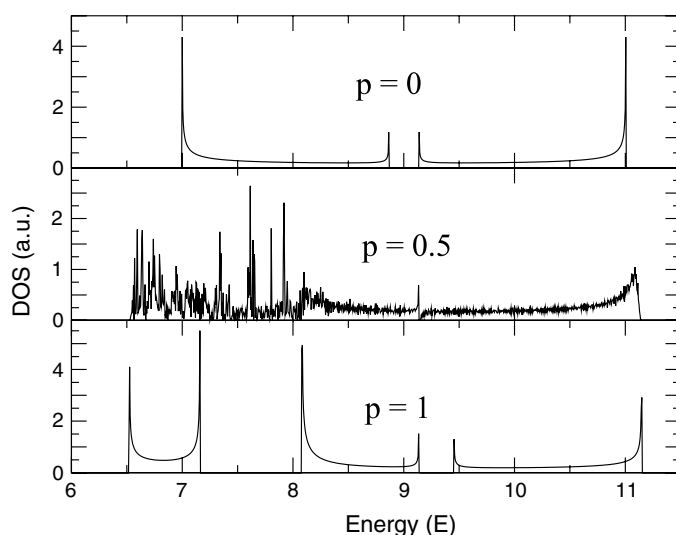
(b) CT sequence ($N = 10^5$).

Fig. 4.5. Plot of the electronic density of states (DOS) versus the reduced energy E (in units of eV), for the particular cases of the hopping term $t = 1$ eV. (a) Poly(CG)-based DNA sequences: the band gap persists for poly(CG) chains with diluted base-pairing, and all van Hove singularities are rounded off; (b) Poly(CT)-based DNA sequences: the band gaps coalesce for base-pair diluted poly(CT) before splitting in three bands. Disorder does not affect the van Hove singularity at $E = \epsilon_T$. The gap-less band structure, together with the non-localization of the resonance state, favors the electronic transport in this case.

Refs. [168,169] for details) provides:

$$G_{n+1,n+1}^{n+1} = \left[E - H_{n+1,n+1}^0 - t_{n+1,n} G_{n,n}^n t_{n,n+1} \right]^{-1},\tag{70}$$

with

$$G_{1,n+1}^{n+1} = G_{1,n}^n t_{n,n+1} G_{n+1,n+1}^{n+1},\tag{71}$$

where $G_{1,n+1}^{n+1}$ denotes the $M \times M$ Green's function operator between the first and the $(n+1)$th base pairs. Also, $G_{n+1,n+1}^{n+1}$ and $H_{n+1,n+1}^0$ are the Green's function operator and the free Hamiltonian for the isolated $(n+1)$ base pair, $t_{n,n+1}$ is the diagonal $M \times M$ matrix coupling the base pairs at position n and $n+1$, and E is the diagonal $M \times M$ matrix for the electron energy.

In the recursive equation above, $G_{1,1}^1 = I$ (identity matrix) and $G_{0,0}^0 = 0$. We stress that for a single-strand DNA-like segment $M = 1$. The Lyapunov exponent for a DNA segment is given by

$$\gamma(E) = (1/2N) \ln \left[\mathrm{Tr} \left| G_{1,N+1}^{N+1} \right|^2 \right].\tag{72}$$

For extended states, $\gamma(E)$ vanishes in the thermodynamic limit.
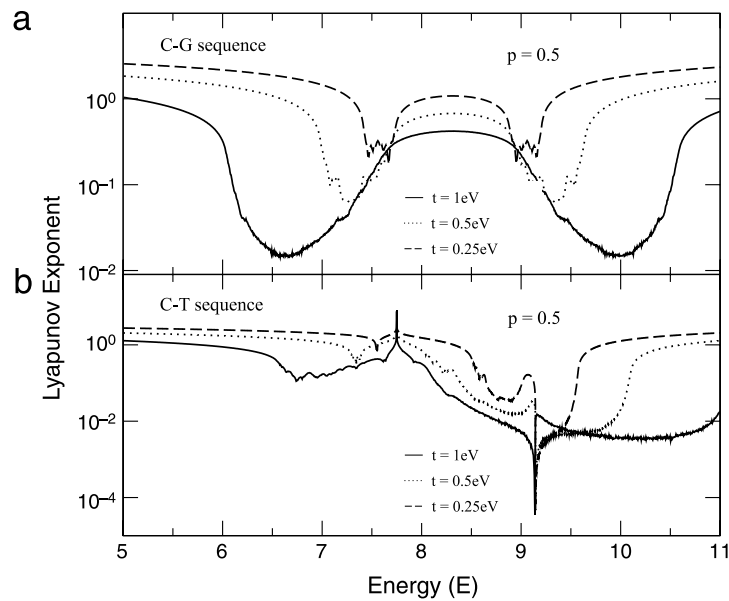
Fig. 4.6. (a) Lyapunov exponent $\gamma(E)$ versus the energy E (in units of eV) for a poly(CG) DNA sequence with $p = 0.5$ diluted base-pairing. All states are exponentially localized, with the maximum localization length being of the order of 10^2 sites for the hopping term $t = 1$ eV, decreasing as $1/t^2$. (b) Same as in (a) but for a poly(CT) DNA sequence. For $E = \epsilon_G$ one observes a strong localization as the renormalized energy ϵ_C^* diverges. At the resonance energy $E = E_0 = \epsilon_T$ the mode is not affected by disorder and keeps its Bloch-like character. Data from different values of the hopping term t confirm that the resonance mechanism is robust with respect to this energy scale.

The resonance effect is robust with respect to distinct transfer integral values, and is more clearly analyzed without considering the additional energy scale associated to distinct intra-strand (t) and inter-strand (w) hopping integrals. In the following illustration, it was considered $w = t = 1$ eV which is somewhat larger than previously reported estimates of intra-strand transfer integrals [170,171], and a typical set for the ionization energies values (see Section 3.2), namely $\epsilon_C = 8.87$ eV (cytosine), $\epsilon_G = 7.75$ eV (guanine), and $\epsilon_T = 9.14$ eV (thymine), all units in eV. An exact diagonalization of the complete tight-binding Hamiltonian, given by Eqs. (63) and (64), provides the participation number of all eigenstates.

The electronic density of states (DOS) is obtained directly from the recursive Dean's method. Fig. 4.5 shows the DOS for three representative values of the concentration of paired cytosine bases, namely:

 (i) $p = 0$, corresponding to pure poly(CG) and poly(CT) chains;
 (ii) $p = 1$, describing the poly(CG) and poly(CT) chains with guanine bases laterally attached to all cytosine bases;
(iii) $p = 0.5$ representing a typical sequence of diluted base-pairing.

The DOS for the poly (CG) sequences is shown in Fig. 4.5(a). The electronic density of states has two main bands, which is typical of binary sequences, with the gap for $p = 1$ being larger than for $p = 0$. Such enhancement of the energy gap is a direct consequence of the base-pairing. For $p = 0.5$, all van Hove singularities at the band edges are rounded off by the presence of disorder. The fluctuations in the DOS have been exploited in the literature to identify the nature of the states [172,173]. The variance in the number of states in a given energy window shall scale linearly with the system size for localized states, while having just a slow logarithmic scaling for extended states. These two regimes reflect the distinct level spacing statistics of localized and extended states. As a result, much smaller fluctuations are attained in the normalized DOS when extended states are present as compared to the fluctuations observed in the energy range corresponding to localized states. These fluctuations are of the same magnitude in both bands, which indicate that these bands are equally affected by disorder.

The DOS for poly(CT)-based chains are depicted in Fig. 4.5(b). For these sequences, a series of relevant features are not found in the previous case. Firstly, the two band structure of the binary $p = 0$ case evolves to a three band structure at $p = 1$, as expected for a periodic structure with three distinct sites in the unit cell. The bottom of the upper band at $p = 0$ coincides with the top of the middle band at $p = 1$. This energy corresponds exactly to the resonance energy $E_0 = \epsilon_T$. When the concentration of the attached guanine bases increases, the two-band structure firstly coalesces in a single band, before splitting in three bands, as shown for the particular case $p = 0.5$. Further, the van Hove singularities are rounded off, except the one located at E_0, which corresponds to the resonance state insensitive to disorder. Therefore, diluted base-pairing produces a gap-less band structure while keeping the states around E_0 extended, an ideal scenario for electronic transport. Additionally, the DOS exhibits stronger fluctuations at the bottom than at the top of the energy band, pointing out that the low-energy states are more localized than the high-energy ones.

The Lyapunov exponent γ directly probes the disorder effect on the nature of the electronic eigenstates. In Fig. 4.6(a), the spectrum of the Lyapunov exponent for the base-pair diluted poly(CG) molecule with $p = 0.5$ is shown. For the hopping amplitude $t = 1$ eV, the Lyapunov exponent achieves a minimum value of the order of 10^{-2} in both energy bands. Therefore,

the maximum localization length in this chain is of the order of 100 sites, i.e., no delocalized mode survives to diluted base-pairing in binary periodic DNA-sequences of corresponding bases, such as poly(CG). The average localization length scales as $1/t^2$. Further, this kind of disorder affects both bands in a similar way, as already pointed out through the analysis of the DOS fluctuations. Fig. 4.6(b) shows the corresponding Lyapunov exponent spectrum for a poly(CT) chain with $p = 0.5$ diluted base-pairing. The presence of two singularities are evident. The first one is at $E = \epsilon_G$ which corresponds to the energy at which the renormalized ϵ_C^* diverges, thus leading to an effective infinite disorder. The one-electron mode at this energy is strongly localized. The second singularity is at $E = E_0 = \epsilon_T$. This corresponds to the energy mode not affected by the disorder and it has a Bloch-like character. The low-energy modes are more localized than the high-energy ones, in agreement with the observation that these regions depict distinct DOS fluctuations. Fig. 4.6 shows the spectra of Lyapunov exponents computed considering chains with weaker hopping amplitudes ($t = 0.5$ and 0.25 eV). They also display the same resonances, thus corroborating the robustness of the resonance mechanism with regard to distinct energy scales of the transfer integrals. The quite distinct effects caused by diluted base-pairing in poly(CG) and poly(CT) have a significant impact on the electronic transport.

5. The role of symmetric and antisymmetric correlations

It is well known that a quasiperiodic two-chain model can support extended states at multiple values of the Fermi energy [174]. Further, it was demonstrated analytically that a two-channel random model can display a band of Bloch-type extended states, when the on-site potentials and the hopping amplitudes show a particular correlation [175]. In particular, the effects of the coexistence of localized and extended states in the correlated random ladder model were recently investigated by using numerical diagonalization and high-order methods to solve the Schrödinger equation [176]. It was shown then that stationary and dynamical properties are dominated by extended states. In addition, it was numerically demonstrated that the superposition of localized and delocalized bands gives rise to a new level-spacing distribution.

Correlated DNA-like tight-binding models can present an apparent delocalization transition [177]. The underlying physical mechanism behind such apparent delocalization transition is directly related to the distinct roles played by symmetric and antisymmetric correlations in the disorder distribution [178]. Considering a two-channel Hamiltonian with a single orbital per site and nearest-neighbor interactions, the wave-packet time evolution is governed by the time dependent Schrödinger equation (with $\hbar = 1$) [178–180]:

$$i \frac{d\psi_j^s}{d\tau} = \epsilon_j^s \psi_j^s + t \left(\psi_{j+1}^s + \psi_{j-1}^s \right) + w \psi_j^{\bar{s}}. \tag{73}$$

Here $s = \pm 1$ labels each strand of the ladder, and $\bar{s} = -s$ indicates its complementary. The index $j = 1, \ldots, N$ (N being the number of base pairs in the DNA segment) runs over the sites along one of the strands coupled by the longitudinal intra-strand hopping parameter t. Also, w is the transverse inter-strand hopping parameter between complementary sites on each strand.

On-site cross correlated energies ϵ_j^s are generated as follows: ϵ_j^{+1} are chosen as an uncorrelated random sequence with $\langle \epsilon_j^{+1} \rangle = 0$ and uniformly distributed within the interval $[-1, 1]$; the on-site energies of the another channel are chosen as (a) $\epsilon_j^{-1} = \epsilon_j^{+1}$ or (b) $\epsilon_j^{-1} = -\epsilon_j^{+1}$. These distinct rules impose, respectively, symmetric and antisymmetric cross correlations in the two-channel Hamiltonian.

Taking the initial condition

$$\psi_j^s(\tau = 0) = \delta_{j,j_0} \delta_{s,s_0}, \tag{74}$$

the set of the above equations can be solved numerically by using a high-order method based on the Taylor expansion of the evolution operator Υ [178]:

$$\Upsilon(\Delta\tau) = \exp(-iH\Delta\tau) = 1 + \sum_{l=1}^{n_0} (-iH\Delta\tau)^l / (l!), \tag{75}$$

H being the tight-binding Hamiltonian. The wave-function at time $\Delta\tau$ is given by

$$|\Phi(\Delta\tau)\rangle = \Upsilon(\Delta\tau)|\Phi(\tau = 0)\rangle. \tag{76}$$

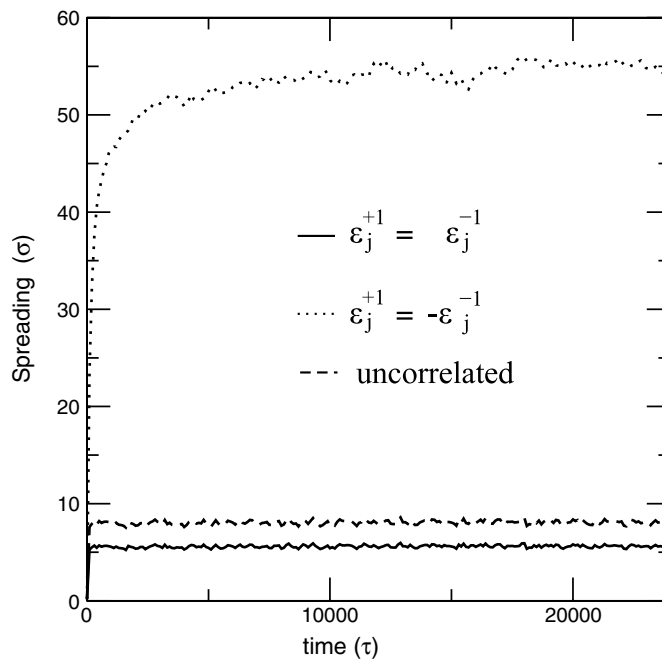This method can be used recursively to obtain the wave-function at time τ. As a first step, we define

$$H^l|\Phi(\tau = 0)\rangle = \sum_{j=1}^{N} \sum_{s=1}^{2} (C_j^s)^l |j, s\rangle. \tag{77}$$

Using the above Schrödinger equation (73), we can compute $H^1|\Phi(\tau = 0)\rangle$ to obtain $(C_j^s)^1$ as

$$(C_j^s)^1 = \epsilon_j^s \psi_j^s + t \left(\psi_{j+1}^s + \psi_{j-1}^s \right) + w \psi_j^{\bar{s}}. \tag{78}$$

Fig. 5.1. The time-dependent wave-packet width $\sigma(\tau)$ versus the time τ. Calculations were done using the number of base-pairs $N = 4000$ and considering distinct kinds of cross correlations within diagonal disorder. Antisymmetric cross correlations $\epsilon_j^{-1} = -\epsilon_j^{+1}$ lead to a wave-packet width much larger than that one produced by symmetric cross correlations $\epsilon_j^{-1} = \epsilon_j^{+1}$.

Therefore, using that

$$H^l|\Phi(\tau=0)\rangle = H \sum_{j=1}^{N} \sum_{s=1}^{2} (C_j^s)^{l-1}|j, s\rangle, \tag{79}$$

$(C_j^s)^l$ can be obtained recursively as

$$(C_j^s)^l = \epsilon_j^s (C_j^s)^{l-1} + t\left[(C_{j+1}^s)^{l-1} + (C_{j-1}^s)^{l-1} \right] + w(C_j^{\bar{s}})^{l-1}. \tag{80}$$

Results were obtained by using $\Delta\tau = 0.5$, and the sum in Eq. (75) was truncated at $n_0 = 20$. This cutoff was enough to keep the wave-function norm conservation along the entire time interval considered.

The square root of the mean-square displacement $\sigma(\tau)$, which gives an estimate of the wave-packet width at time τ, is obtained from

$$\sigma(\tau) = \sqrt{ \sum_{j=1}^{N} \sum_{s=1}^{2} \left[(j - j_0)^2 + (s - s_0)^2 \right] |\psi_j^s(\tau)|^2 }. \tag{81}$$

In the long-time regime, its scaling behavior can also be used to distinguish between localized and delocalized wave-packets [179,180]. Further, the Lyapunov exponent $\gamma(E)$ of long two-channel segments can be obtained using the same formalism described in Section 4.3.

Fig. 5.1 depicts the time dependence of the wave-packet width $\sigma(\tau)$ given by Eq. (81). We have considered $N = 4000$ sites and the hopping terms $t = w = 1$ eV, using both kinds of cross correlations and a standard uncorrelated random two-channel system. Antisymmetric cross correlations $\epsilon_j^{-1} = -\epsilon_j^{+1}$ (see the dotted-line profile) produce a localization degree much weaker than the other cases (see the solid-line data for $\epsilon_j^{-1} = \epsilon_j^{+1}$ and the dashed line profile for the uncorrelated case).

Fig. 5.2 shows a comparative numerical analysis between both types of cross correlations by considering the scaled wave-packet width $\sigma(\tau)/N$ versus the scaled time τ/N. Calculations were done using the same values of t and w but distinct segment sizes. For extended states, data from distinct chain sizes would collapse into a single curve, signaling a ballistic transport ($\sigma(\tau) \propto \tau$). Both calculations show no data collapse. Further, the scaled asymptotic wave-packet width decreases as the system size increases, pointing out to an ultimate localization of the wave-packet in the thermodynamic limit. Therefore, the cross correlations used here do not induce the emergence of truly extended states. These results agree with previous calculations found in Refs. [179–181], confirming that diagonal cross correlations are not enough to promote a metal–insulator transition in a two-channel disordered Hamiltonian.

a

b
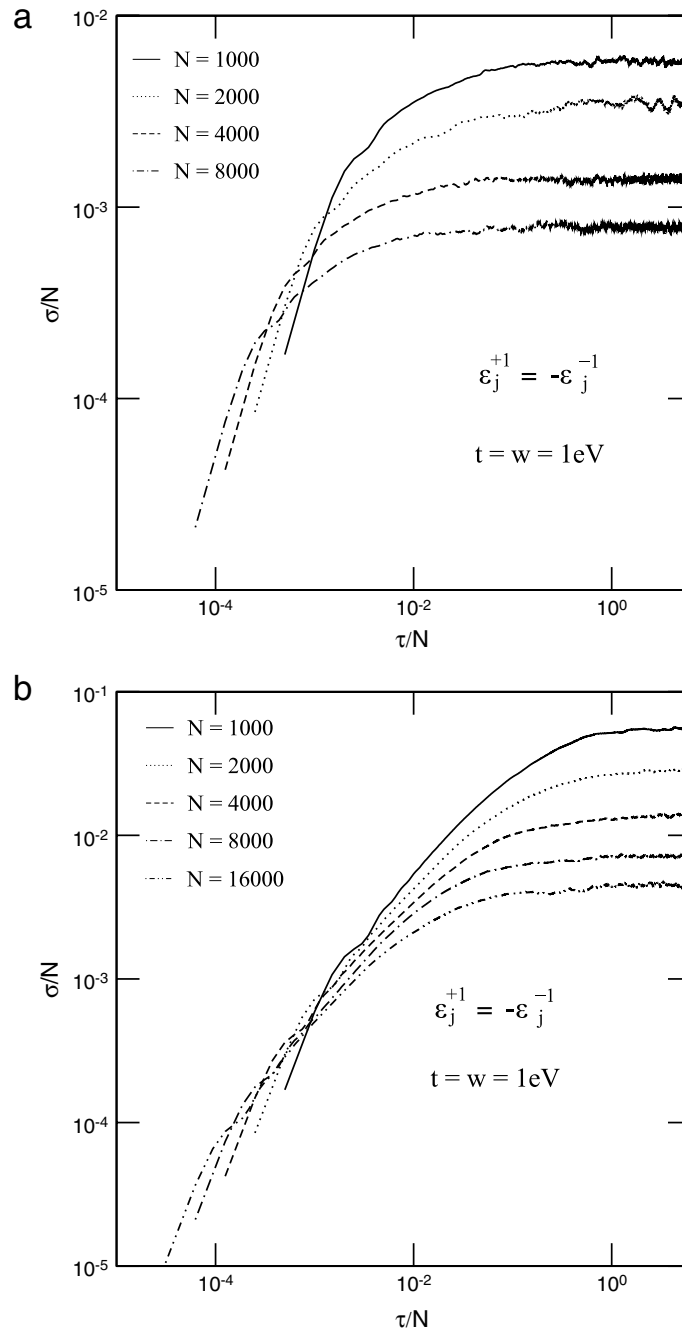
Fig. 5.2. Scaled wave-packet width $\sigma(\tau)/N$ versus the scaled time τ/N. Calculations were done using $t = w = 1$ eV and the number of base-pairs $N = 1000$ up to 16,000 sites. Our calculations indicate that the asymptotic scaled wave-packet width $\sigma(\tau)/N \to 0$ as N increases for both cross correlations used here, a typical signature of localized wave-packets.

However, it is clear from both Figs. 5.1 and 5.2 that the antisymmetric cross correlation ($\epsilon_j^{-1} = -\epsilon_j^{+1}$) leads to a wave-packet spread much larger than the symmetric one ($\epsilon_j^{-1} = \epsilon_j^{+1}$). Let us stress that antisymmetric cross correlation contains the same ingredients used in the generic DNA model studied in Ref. [177], i.e., when $\langle \epsilon_j^{-1} + \epsilon_j^{+1} \rangle = 0$. Additional data and theoretical arguments unveiled the origin of the substantial decrease of the degree of localization, and the apparent phase transition found in the two-channel model with antisymmetric diagonal cross correlations [177].

In the two-channel model with symmetric cross correlated disorder, the Hamiltonian model of an isolated dimer pair has eigenvalues given by $\epsilon_j \pm w$. In the regime of strong inter-chain coupling, these two modes cannot be efficiently mixed by the intra-chain coupling. Therefore the system shall behave as two uncoupled random chains with energy offset given by $\pm w$ and the disorder strength is simply the one originally present in the on-site energies. Within this scenario, the degree of localization shall be similar to the one present in the system without cross correlations.

On the other hand, the Hamiltonian model of an isolated dimer pair with antisymmetric diagonal terms has eigenvalues given by $\pm[\epsilon_j^2 + w^2]^{1/2}$. In the regime of strong inter-chain coupling, these can be written as $(\epsilon_j^2/2\omega) \pm w$. These modes
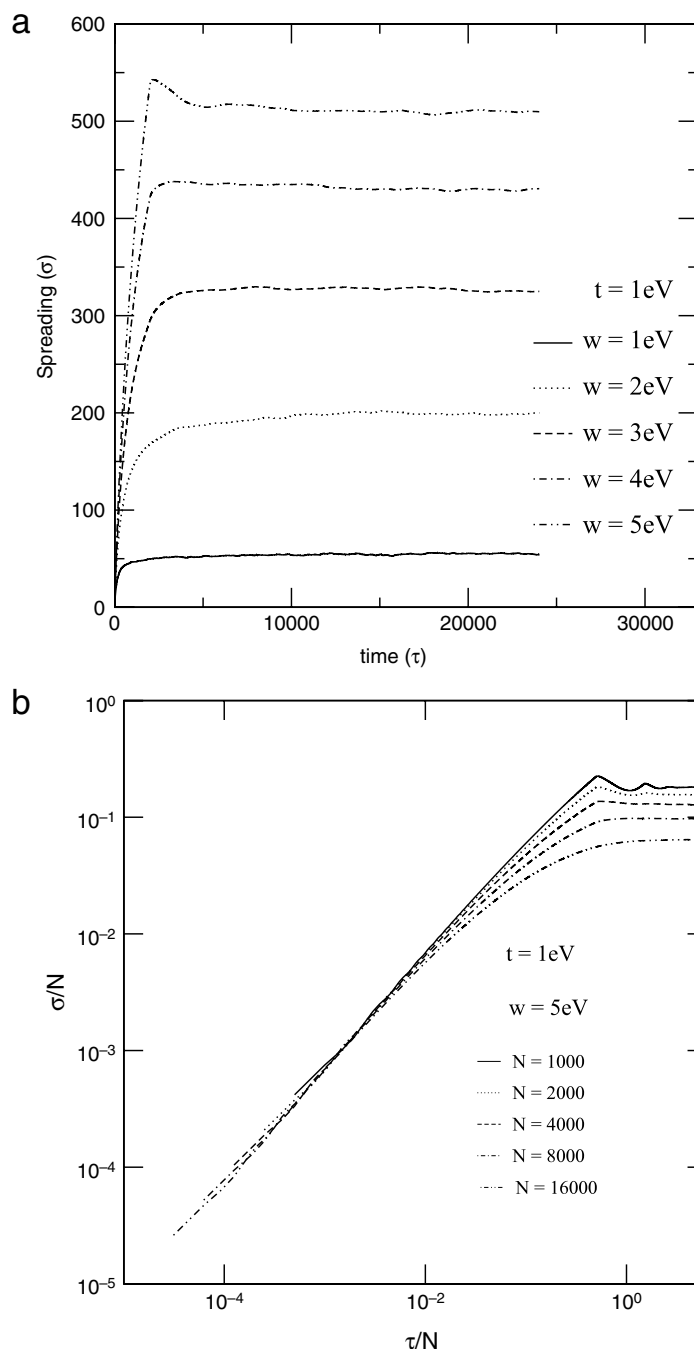
Fig. 5.3. (a) The wave-packet width $\sigma(\tau)$ versus the time τ for the number of base-pairs $N = 4000$, $\epsilon_j^{-1} = -\epsilon_j^{+1}$, intra-chain hopping $t = 1$ eV and inter-chain hopping $w = 1$ up to 5 eV. When the inter-chain hopping w is increased in the two-channel systems with antisymmetric cross correlations $\langle \epsilon_j^{-1} + \epsilon_j^{+1} \rangle = 0$, the local effective disorder along the quasi-unidimensional system goes to zero, thus increasing the localization length. (b) Scaled spread $\sigma(\tau)/N$ versus the scaled time τ/N for $t = 1$ eV, $N = 1000$ up to 16,000 sites and $w = 1$ up to 5 eV. In spite of the fact that antisymmetric cross correlations favor the increase of the localization length, it does not lead to truly extended wave-packets once $\sigma(\tau)/N \rightarrow 0$ as N increases.

also are not effectively mixed by the intra-chain coupling, and the system shall behave as two independent random chains. However, the effective disorder is rescaled, and becomes of the order of $1/w$. Recalling that the localization length in random chains is proportional to the square of the inverse disorder width, antisymmetric cross correlations shall have exponentially localized states, whose localization length grows with w^2 in the regime of strongly coupled chains.

The above picture is corroborated by additional numerical data of the wave-packet width, density of states and localization length of the energy eigenmodes for both models with cross correlated disorder, as well as for the two-channel model with uncorrelated disorder.

In Fig. 5.3(a), the wave-packet width $\sigma(\tau)$ is plotted versus the time τ for $N = 4000$, and the following physical parameters: antisymmetric cross correlations $\epsilon_j^{-1} = -\epsilon_j^{+1}$; $t = 1$ eV; and $w = 1$ up to 5 eV. The results show that the wave-packet spread increases as the inter-chain coupling w is also increased. However, even in the regime of strong

a

b
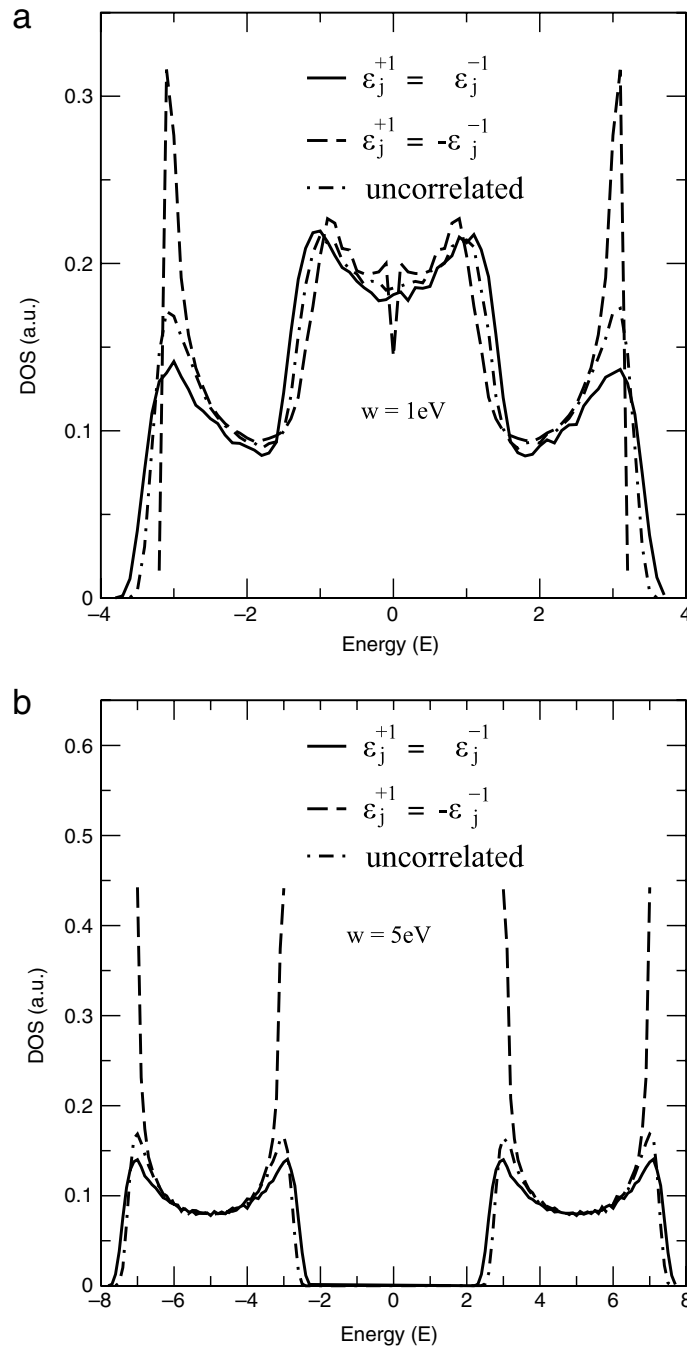
Fig. 5.4. (a) The normalized density of states DOS(E) versus the energy E computed using the number of base-pairs $N = 5000$ sites, 500 disorder configurations and (a) inter-chain hopping $w = 1$ eV, (b) inter-chain hopping $w = 5$ eV. When the inter-chain hopping w is increased in the two-channel systems with antisymmetric cross correlations $\langle \epsilon_j^{-1} + \epsilon_j^{+1} \rangle = 0$, the density of states becomes similar to the DOS of two uncoupled perfect chains with on-site energies w and $-w$. Symmetric cross correlations produce a DOS with rounded band edges, signaling that the underlying disorder remains relevant even in the regime of strong interchain coupling.

inter-chain coupling (w), the asymptotic scaled spread $\sigma(\tau)/N$ decreases with the system size, indicating an ultimate localization in the thermodynamic limit. Therefore, the reduction on the degree of localization reported in Ref. [177] actually reflects the weakening of the effective disorder in the two-channel system with antisymmetric cross correlations and strong intra-chain hopping. This specific cross correlation does not promote the emergence of truly extended states.

To reinforce the above picture, Fig. 5.4 shows the normalized density of states (DOS)

$$\rho(E) = \sum_{E_n} \delta(E - E_n), \tag{82}$$

E_n being the eigenvalues obtained from numerical diagonalization. Calculations were done using $N = 5000$ sites and 500 disorder configurations, with $w = 1$ eV (see Fig. 5.4(a)) and $w = 5$ eV (see Fig. 5.4(a) and (b)). When the intra-chain (t)
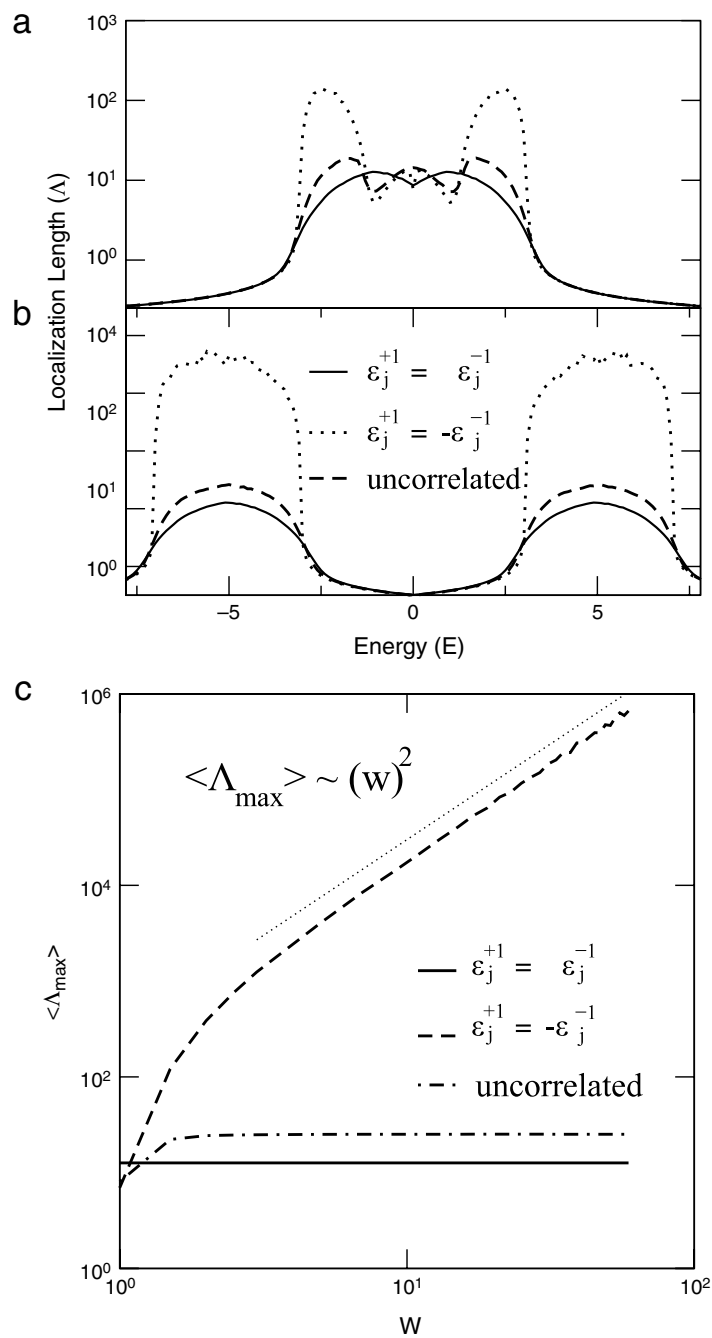
Fig. 5.5. The localization length $\Lambda(E)$ versus the energy E computed using the number of base-pairs $N = 10^7$ sites, considering both kinds of cross correlations and a standard uncorrelated random two-channel system. Calculations were done using the intra-chain hopping $t = 1$ eV: (a) inter-chain hopping $w = 1$ eV; (b) inter-chain hopping $w = 5$ eV. (c) The largest localization length $\Lambda_{max}(E)$ versus the inter-chain hopping w. The localization length diverges with w^2 in the two-channel systems with antisymmetric cross correlations, while it remains finite in the other two cases.

and the inter-chain (w) couplings are of the same order, the DOS displays a single band which start to split in a two band structure when the intra-chain coupling t is increased. Even in this regime of intermediate intra-chain coupling, the band edges in the presence of antisymmetric cross correlations are sharper than in the other cases. For large intra-chain coupling, the density of states of the two-channel systems with symmetric cross correlations is quite similar to the one displayed by the corresponding uncorrelated model. The DOS in these two cases resembles the one of two uncoupled chains with a finite disorder width, signaled by the rounding of the band edges. On the other hand, the DOS of the model with antisymmetric cross correlations displays quite sharp band edges in the limit of strong intra-chain coupling, which is consistent with the vanishing of the effective disorder.

Finally, Fig. 5.5 shows the localization length $\Lambda(E)$ as a function of energy computed using $N = 10^7$ sites, for both kinds of cross correlations, and a standard uncorrelated random two-channel system, considering the same values for the hopping terms t and w, as in the previous example. Even in the regime of intermediate intra-chain coupling, the localization length

near the band edges is one order of magnitude larger in the presence of antisymmetric cross correlations when compared with the other two cases. This effect becomes much more pronounced in strongly coupled channels.

In Fig. 5.5(c), the largest localization length Λ_{max} versus the inter-chain hopping w is plotted. The localization length diverges as w^2 in the two-channel systems with antisymmetric cross correlations, while the symmetric correlations have a small influence on the degree of localization.

In summary, quasi-unidimensional structures with diagonal disorder displaying local correlations do not support truly extended states. Symmetric cross correlations ($\epsilon_j^{-1} = \epsilon_j^{+1}$) have a very limited influence on the degree of localization, although antisymmetric correlations ($\epsilon_j^{-1} = -\epsilon_j^{+1}$) substantially inhibit the Anderson localization, specially in the regime of strongly coupled chains.

6. Nonlinearity and field effects

In low-dimensional systems, the effect of nonlinearity seems to be dominant over the role played by disorder. Considering a discrete nonlinear Schrödinger and quartic Klein–Gordon equations with disorder, it was recently proved that the second moment and the participation number of the wave-packet do not diverge simultaneously [182,183]. The spreading of a wave-packet in a 1D discrete nonlinear Schrödinger lattice with disorder was also recently studied, and it was observed that Anderson localization is suppressed and a subdiffusive dynamics takes place above a certain critical nonlinearity strength [184]. Moreover, analytical and numerical calculations for a reduced Fermi–Pasta–Ulam chain indicate that energy localization does not require more than one conserved quantity [185]. From the experimental point of view, investigations were made to clarify the interplay between disorder and nonlinearity, by means of the evolution of linear and nonlinear waves in coupled optical waveguides patterned on AlGaAs substrate. It was also observed that nonlinear perturbations enhance localization of linear waves, while inducing delocalization of the nonlinear one [186].

Nonlinearity, disorder and correlations will be investigated in this section, once they are particularly important for the description of DNA-like segments. A systematic *ab initio* study of the DNA conformational modes and their possible interactions with the electron motion was already provided together with an effective Hamiltonian for distinct kinds of DNA polarons [187]. The electron–phonon interaction can also be taken within the adiabatic approximation proposed in Refs. [188–190]. The effective third order electron–phonon contribution was pointed out as a possible mechanism to break-down the localization rules in disordered chains [191]. Recently, the competition between nonlinearity and a perpendicular electric field has been investigated, suggesting that disordered ladder models, with a topology similar to the effective Hamiltonian models of DNA molecules (see Section 3), display a subdiffusive spread of the electronic wave-packet induced by a weak nonlinearity, while a partial self-trapping of the wave-packet is achieved in the strongly nonlinear regime [192]. Further, the wave-packet subdiffusive spreading can be suppressed by an external electric field applied perpendicular to the ladder helicity axis.

6.1. Adiabatic electron–phonon interaction

In this approach, one makes use of an adiabatic electron–phonon interaction, within an effective nonlinear tight-binding model Hamiltonian, describing an electron moving in a twisted ladder geometry with correlated disorder. This structure mimics the topology and the inter-strand correlations presented in DNA segments.

Consider now the time dependent Schrödinger equation given by Eq. (73), provided the term ϵ_j^s is replaced by $\epsilon_j^s + \chi |\psi_j^s|^2$, χ being the nonlinear coupling associated with an underlying local electron–phonon interaction. The electron is taken as initially localized at the orbital $|j_0, s_0\rangle$. The wave-packet dynamics is probed by following the temporal evolution of the square root of the mean-square displacement $\sigma(\tau)$, given by Eq. (81), as well as the participation function $\xi(\tau)$ and the return probability $R(\tau)$ defined by

$$\xi(\tau) = \left[\sum_{j,s} |\psi_j^s(\tau)|^4 \right]^{-1}, \tag{83}$$

$$R(\tau) = |\psi_{j_0}^{s_0}(\tau)|^2. \tag{84}$$

The participation function $\xi(\tau)$ gives an estimate of the number of sites over which the wave-packet is spread at time τ. In the long-time regime, its scaling behavior can also be used to distinguish between localized and delocalized wave-packets. In addition, in a regime of strong localization, the probability of finding the particle at the initial site at long times $R_\infty \equiv \lim_{\tau\to\infty} R(\tau)$ is always nonzero [193].

Uncorrelated random sequences, containing four distinct values of the on-site potentials, were generated mimicking the sequence of the four nucleotides present in DNA segments (A, G, T, C). Further, the generated sequences had the same fraction of each nucleotide found in the human chromosome Ch22. In DNA molecules, the intra-strand hopping amplitude is smaller than the disorder width due to the variability of the on-site energies. The inter-strand coupling mediated by the hydrogen bonds between complementary sequences is weaker than the intra-strand one. In order to reproduce some specific features of real DNA molecules, it would be important to consider both inter- and intra-strand hopping variability.
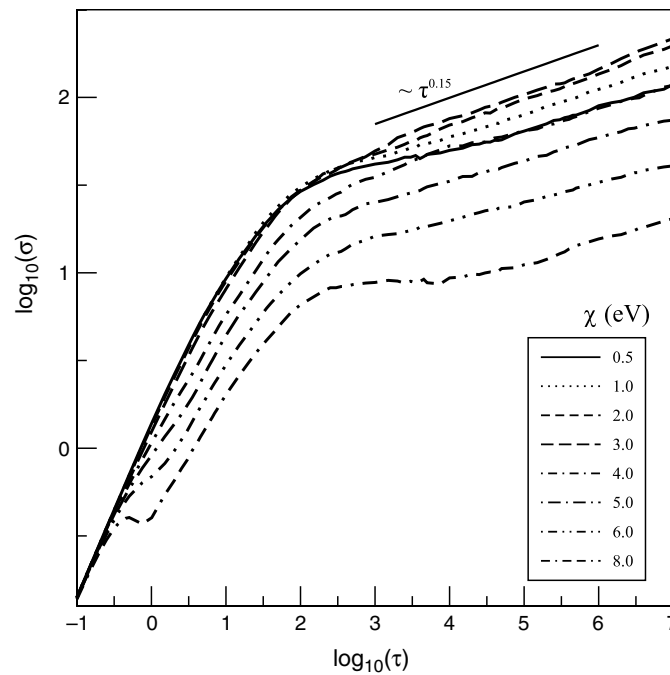
Fig. 6.1. Log–log plot of the wave-packet width $\sigma(\tau)$ for several values of the nonlinear coupling constant χ. At long times $\sigma(\tau) \propto \tau^{0.15(2)}$, irrespective to the nonlinear strength.

Although the following numerical results were obtained for a particular parameter set motivated by the previous effective Hamiltonian descriptions of DNA-segments, discussed in Section 3, the overall physical properties do not depend on the specific choice of the Hamiltonian physical parameters.

6.2. Wave-packet dynamics

A wave-packet initially localized at the guanine closer to the center of the double-strand segment was considered. In order to avoid finite-size effects, large segments with $N = 1000$ base-pairs were used. All quantities were averaged over 20 distinct segments to account for configurational variability. Fig. 6.1 shows the mean-square displacement $\sigma(\tau)$ for several values of the electron–phonon coupling constant χ. In the absence of nonlinearity ($\chi = 0$) the wave-packet spreads over a segment of finite length. This is the well-defined Anderson localization regime in low-dimensional systems with uncorrelated disorder.

For nonlinear double-strand chains, a subdiffusive regime $\sigma(\tau) \propto \tau^{0.15(2)}$ is observed. This exponent agrees with the numerical calculations for 1D nonlinear chains with uncorrelated disorder [184]. However, two distinct trends in the regime of weak and strong nonlinearities are observed. For $\chi < 3$ eV, the wave-packet width in the asymptotic sub-diffusive regime increases as χ is increased. On the other hand, a reverse trend sets up for stronger nonlinearities. Although the wave-packet width remains subdiffusive in these two regimes, such non-monotonic dependence on the nonlinearity points to distinct dynamical properties, as explored below.

Fig. 6.2 depicts the time dependence of the participation function $\xi(\tau)$ computed considering $N = 1000$ base-pairs. The nonlinear coupling ranged from $\chi = 0.5$ up to 8 eV. The wave-packet displays a subdiffusive dynamics in the regime of weak nonlinear couplings ($\chi < 3$ eV), in which the time dependent participation function behaves like $\xi(\tau) \propto \tau^{0.25(2)}$. However, the participation function remains finite in the regime of strong nonlinearities and, as a consequence, the divergences of the wave-packet width and participation number are not simultaneous. This feature has already been pointed out in disordered nonlinear systems [182]. The regime of weak nonlinearity corresponds to a true delocalized phase for which the wave-packet spatial extension diverges as the wave-packet continuously spreads over the system. For strong nonlinearities, the wave-packet extension remains finite, although the second moment of the distribution continues to increase sub-diffusively. This feature is related to a partial self-trapping of the wave-packet while the rest subdiffuses [183].

In order to have a more precise estimation of the critical nonlinearity delimiting the regimes of delocalized and partially self-trapped wave-packets, we plot in Fig. 6.3 the return probability at very long times $R(\tau \to \infty)$ versus the strength of the nonlinear coupling χ (after reflection at the chain boundaries). A clear transition is signaled at $\chi_c \simeq 2.5$–3.0 eV. Below χ_c the return probability decays as $1/N$, as stressed in the inset. For $\chi > \chi_c$ the return probability becomes roughly size independent. This result gives further support to the below claims, namely:

(i) For weak nonlinear couplings $\chi < \chi_c$, the asymptotic return probability $R(\tau \to \infty)$ approaches zero, in agreement with the delocalized subdiffusive dynamics exhibited by both the wave-packet width and participation function.
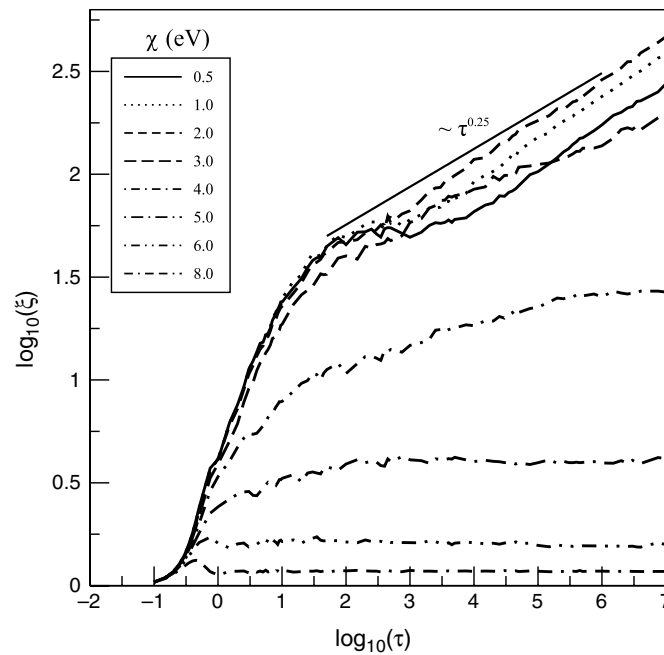
Fig. 6.2. Log–log plot of the time dependent participation function $\xi(\tau)$ for several values of the nonlinear coupling χ. At moderate electron–phonon couplings the participation function displays clear signatures of an asymptotic dynamics with $\xi(\tau) \propto \tau^{0.25(2)}$. For large couplings ($\chi > 3$ eV) the participation function saturates, thus indicating partial spatial localization of the wave-packet.
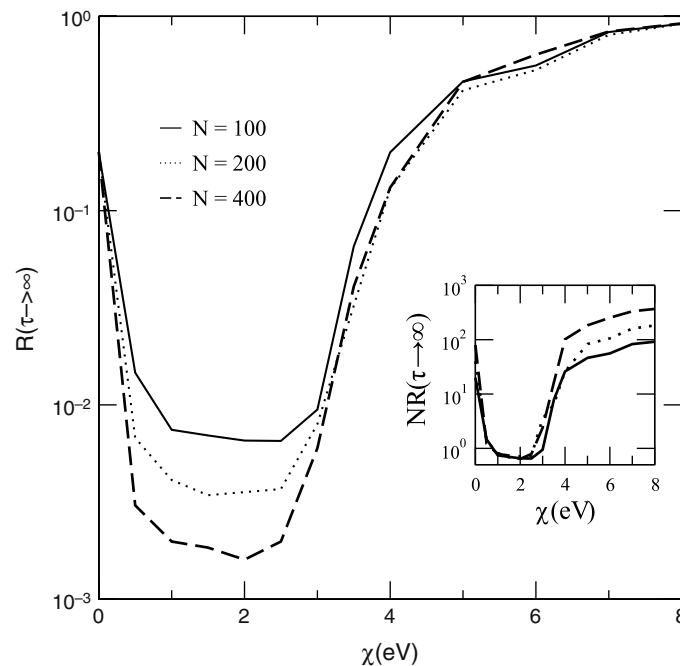
Fig. 6.3. Asymptotic return probability $R(\tau \to \infty)$ as a function of the nonlinear coupling χ in eV. For $0 < \chi < 2.5 - 3.0$ eV, the asymptotic return probability approaches zero as the system size increases, in agreement with the subdiffusive regime of the participation function shown in Fig. 6.2. For larger nonlinearities, the return probability remains finite and size independent. The inset shows the re-scaled asymptotic return probability $NR(\tau \to \infty)$ as a function of the nonlinear coupling χ in eV. The collapse of data at small nonlinearities signals the $1/N$ scaling of $R(\tau \to \infty)$ in the partially trapped regime.

(ii) For strong nonlinear couplings $\chi > \chi_c$, there is a localized regime where $R(\tau \to \infty) \neq 0$ corresponding to the self-trapping phenomenon already reported in 1D nonlinear chains. However, due to the subdiffusive growth of the wave-packet width, such self-trapping is only partial [188,193].

An external electric field $\mathcal{E}$ applied perpendicular to the ladder main axis can be used to manipulate the trapped electronic density. In this case, the helix conformation of the strands becomes important. This is equivalent to take into account a gate voltage drop across the double helix. A $N = 10$ base-pairs full-twist period is considered which is similar to the one exhibited by the B form of the DNA. Neglecting the difference between the major and the minor grooves, the site energies under the
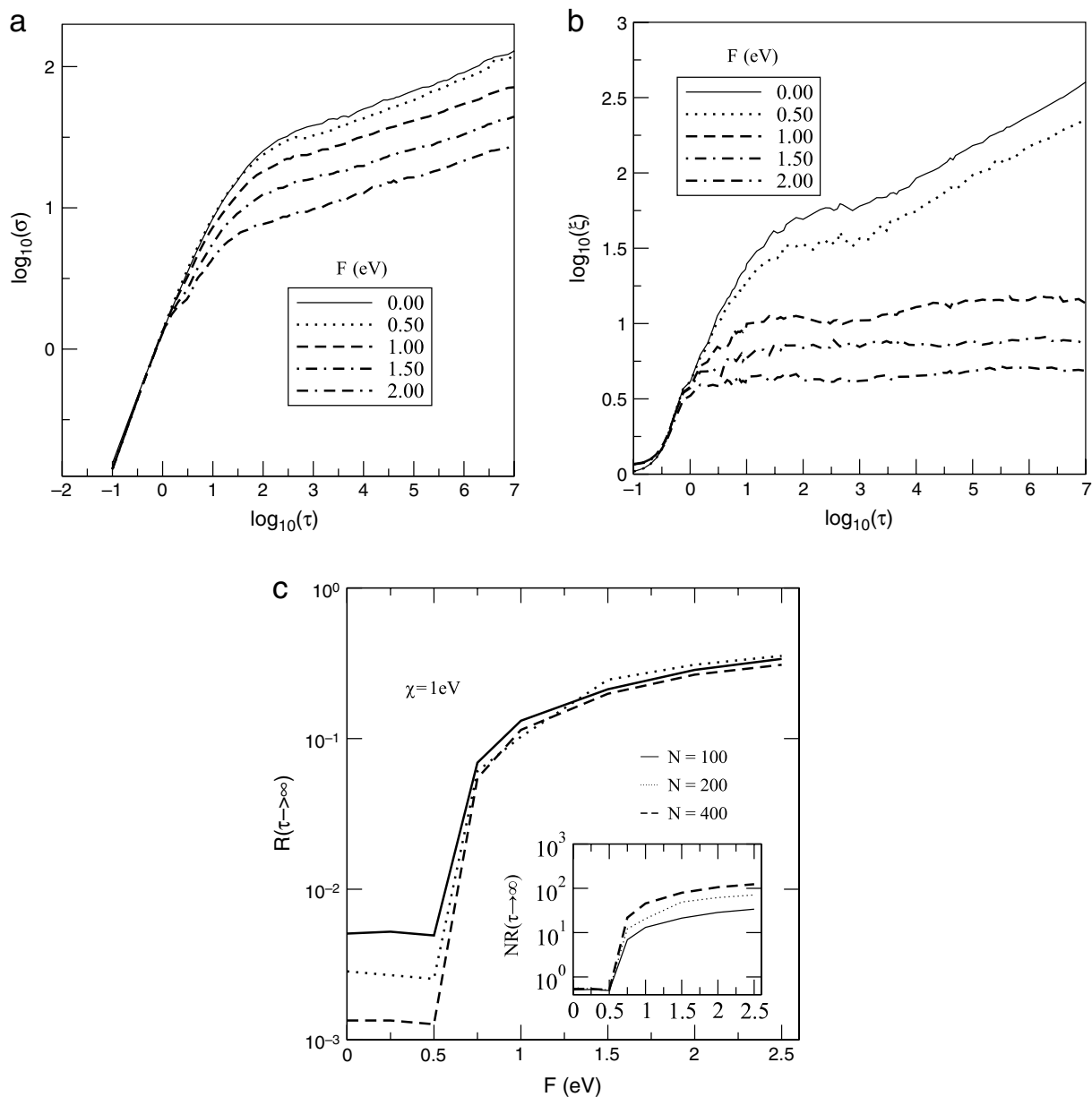
Fig. 6.4. (a) The wave-packet width $\sigma(\tau)$ and (b) the participation function $\xi(\tau)$ as a function of time at the nonlinear coupling constant $\chi = 1$ eV and several values of the perpendicular gating energy F, indicated on the labels. Notice that a partial self-trapping is attained at strong fields, signaled by the subdiffusive wave-packet width spread together with a saturated participation function. (c) Asymptotic return probability $R(\tau \to \infty)$ versus the perpendicular gating energy F, indicating that the partial self-trapping takes place for gating energies $F > 0.5$ eV. The inset shows the re-scaled asymptotic return probability $NR(\tau \to \infty)$ as a function of F, which exhibits a data collapse in the delocalized regime.

gating electric field $\mathcal{E}$ are taken as [194]:

$$\mathcal{E} = \epsilon_j^s + F_j \cos(2\pi j/10), \tag{85}$$

with ϵ_j^s being the site energy of the jth base at the strand s of the DNA molecule at zero field. Also, F_j is the perpendicular gating energy, defined by $F_j \equiv F = e\mathcal{E}r$ (considered homogeneous for simplicity), where $r \sim 1$ nm is the strand radius.

In Fig. 6.4(a) and (b), the wave-packet width $\sigma(\tau)$ and the participation function $\xi(\tau)$ are plotted as a function of time, for several values of the perpendicular gating energy F. For these values of F, the wave-packet spreads continuously over the lattice in the absence of the external field, with both the wave-packet width and participation function growing subdiffusively, showing that the perpendicular gating electric field F reduces the wave-packet spreading. However, the subdiffusive character of both wave-packet width and participation function seems to remain for weak fields. This feature can be associated with the effective increase of the disorder width introduced by the perpendicular external electric field $\mathcal{E}$.

On the other hand, the external electric field $\mathcal{E}$ has a strong impact in the self-trapping phenomenon. Fig. 6.4(b) clearly show that the participation function saturates at stronger fields even though the wave-packet width still keeps its subdiffusive character. For completeness, Fig. 6.4(c) shows the asymptotic return probability versus the perpendicular gating energy F. While the return probability vanishes as the number of base-pairs N increases in the absence of the external field,

a finite fraction of the electronic wave-packet becomes trapped on its initial location when the perpendicular gating energy exceeds a critical value of the order of $F_c = 0.5$ eV. The fraction of the electronic density that becomes trapped increases as the electric field is increased.

In summary, the dynamics of an electron wave-packet in a double-stranded DNA chain with a random sequence of on-site potentials and a cubic nonlinearity associated with an adiabatic electron–phonon interaction can be manipulated by using a transverse electric field $\mathcal{E}$. In the absence of nonlinearity the system shows a well defined Anderson localization regime. However, when the electron–phonon coupling is turned on, a subdiffusive regime arises in the regime of small nonlinearities, and the electronic wave-packet completely escapes from its initial location. In the regime of strong nonlinearities, a partial self-trapping emerges. In this regime a finite portion of the wave-packet remains trapped near its initial position while the other part spreads subdiffusively. Furthermore, the gating electric field $\mathcal{E}$ reduces the wave-packet spreading, being able to trap a finite fraction of the electronic density of states near its initial location, a phenomenon that is controlled by its intensity. It is important to stress that field-controlled devices play a mayor role in conventional electronics, and therefore, the mechanism for trapping electrons in helical double-strands described above opens up the possibility of tailoring new field-controlled nanoscale bio-electronic devices.

7. Thermodynamic properties

One important issue worthy of attention, and so far little explored in quasiperiodic structures, is the connection between the scale invariance of their energy spectra and their thermodynamic properties. In order to fill this gap, it is our intention in this section to pay close attention to this issue, considering the thermodynamics properties of the DNA molecule as described by quasiperiodic systems in the classical (Maxwell–Boltzmann), quantum (Fermi–Dirac) and the so-called extensive statics.

Simplified fractals based on the Cantor sequence [195,196], as well as the critical attractor of the logistic and circle maps at the onset of chaos [197–199], have been used recently to model the energy spectrum of quasiperiodic systems. The thermodynamic behavior derived from such self-similar spectra display some anomalous features, with the most prominent one being related to the emergence of log-periodic oscillations in the low-temperature behavior of the specific heat.

A series of recent works looking for connections with the quasiperiodic aspects of these spectra (scaling laws, fractal dimension, etc.), as well as for some kind of common behavior in the specific heat spectra, have shown, among other things, that the average low-temperature specific heat is intimately connected with some underlying fractal dimension characterizing the energy spectrum [200].

The unique structure of DNA also allows various alterations of its material properties, which could modify its electrical, optical, and thermodynamic properties, revealing additional features. Early theoretical and experimental works on the low-temperature heat capacity of DNA primarily took into account the phonon contributions, specifically the redundant low-energy density of the vibrational states, concluding that the low-energy of the DNA is not unique among biopolymers, and that its specific heat possesses a combination of the properties similar to those of glasses and other disordered materials [201].

Another important issue concerns the relationship between the low-temperature thermodynamic properties and the multi-fractal character of the energy spectra of a sequence dependent finite segment of a DNA molecule. More specifically, what happens to the specific heat spectra profile in these cases? Does it present log-periodic oscillations as a function of the temperature T in the low temperature region, around a mean value given by a characteristic dimension of the energy spectrum? The answers for these and other questions are the main purposes of this section. Our principal intent is to compare the different spectra profiles, seeking possible differences and similarities among them, with the objective to establish some kind of standard behavior.

7.1. Maxwell–Boltzmann statistics: the single-strand DNA structure

Consider the effective tight-binding Hamiltonian with a single orbital per site, ϵ_n, at the orbital ψ_n, and nearest-neighbor interactions describing a single-strand DNA structure, as depicted in Eq. (11). This (discrete) Schrödinger equation can be also written (like in Section 3.3 for the double-strand case) as [202]

$$\begin{pmatrix} \psi_{n+1} \\ \psi_n \end{pmatrix} = M(n) \begin{pmatrix} \psi_n \\ \psi_{n-1} \end{pmatrix}, \tag{86}$$

where $M(n)$ is the transfer matrix

$$M(n) = \begin{pmatrix} t - \epsilon_n & -1 \\ 1 & 0 \end{pmatrix}. \tag{87}$$

After successive applications of the transfer matrices we have

$$\begin{pmatrix} \psi_{n+1} \\ \psi_n \end{pmatrix} = M(n)M(n-1) \cdots M(2)M(1) \begin{pmatrix} \psi_1 \\ \psi_0 \end{pmatrix}. \tag{88}$$
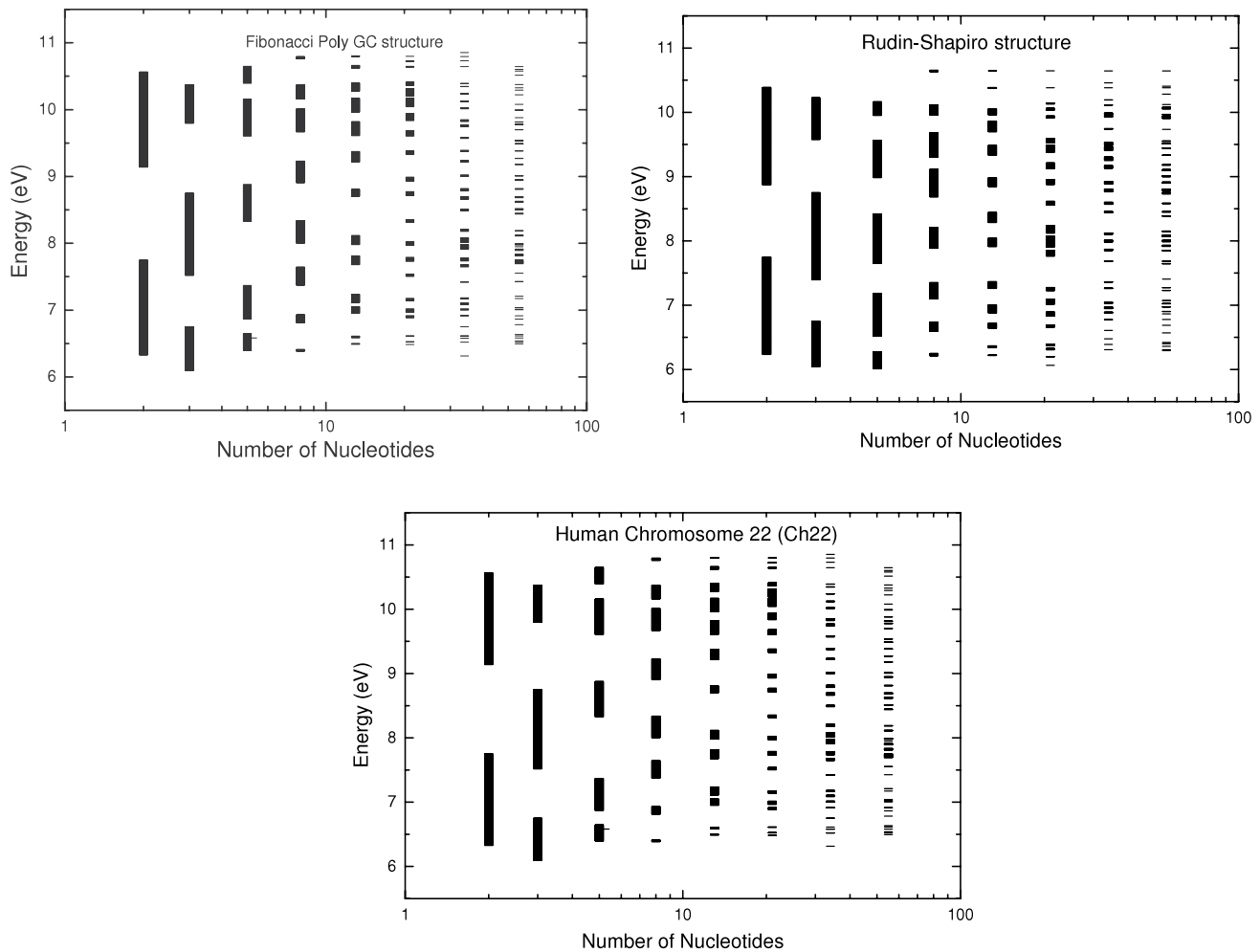
Fig. 7.1. Energy spectrum for finite segment of a single-strand DNA molecule following: (a) Fibonacci sequence; (b) Rudin–Shapiro sequence; (c) DNA sequenced human chromosome 22 (Ch22).

In this way, we have the wave function at an arbitrary site. As before, calculating the product of transfer matrices is completely equivalent to solve the Schrödinger equation for the system. The criterium for allowed energy is when $(1/2)\text{Tr}[T_n] < 1$, with Tr meaning the trace of the transfer matrix T_n, and $T_n = M(n)M(n-1)\cdots M(2)M(1)$.

Fig. 7.1 shows the electron energy spectra, as measured by their equivalent bandwidth Δ (the sum of all allowed energy regions in the band structures), as a function of the number of nucleotides n, for the quasiperiodic sequences of (a) Fibonacci, (b) Rudin–Shapiro, and (c) the genomic Ch22 DNA structure.

We have also investigate their multifractal behavior which is, in general, a common property of strange attractors in nonlinear systems [203]. In order to characterize these objects, it is convenient to introduce the function $f(\alpha)$, known as the multifractal spectrum or the spectrum of scaling indices. Loosely, one may think of the multifractal as an interwoven set of fractals of different dimensions $f(\alpha)$, where α is a measure of their relative strength [204]. The formalism relies on the fact that highly nonuniform probability distributions arise from the nonuniformity of the system. Usually, the singularity spectrum has a parabolic-like shape, distributed in a finite range $[\alpha_{min}, \alpha_{max}]$, which are the minimum and maximum singularity strengths of the intensity measure, respectively. They correspond also to the exponents governing the scaling behavior in the most concentrated (α_{min}) and rarefied (α_{max}) regions of the attractor. The value $\Delta\alpha = \alpha_{max} - \alpha_{min}$ may be used as a parameter to measure the degree of randomness of the band width distribution.

The most powerful method to calculate the $f(\alpha)$ function was developed by Chhabra [205], and is described as follows: let us define a measure ζ_i by normalizing the local energy band widths Δ_i, i.e., $\zeta_i = \Delta_i / \sum_i \Delta_i$ (here i characterize a particular value of the number of nucleotides in Fig. 7.1). Then we construct a parametrized family of normalized measures defined by $\mu_i = \zeta_i^v / \sum_i \zeta_i^v$, which represents a generalization of the original measure ζ_i. The $f(\alpha)$ function is obtained by varying the parameter v and calculating

$$f(\alpha_v) = \lim_{B\to\infty}\left[-\sum_i \mu_i \ln \mu_i / \ln B\right], \tag{89}$$

$$\alpha_v = \lim_{B\to\infty}\left[-\sum_i \mu_i \ln \zeta_i / \ln B\right], \tag{90}$$

where B is the number of boxes (bands in Fig. 7.1). The value of $\Delta\alpha = \alpha_{max} - \alpha_{min}$ could be used as a parameter to measure the degree of randomness of the band width distribution. The values of α_{min} and α_{max} for the energy spectra of the quasiperiodic structures (Fibonacci and Rudin–Shapiro) as well as of the genomic Ch22 modeling the DNA molecules, can be found below:

(a) for the Fibonacci quasiperiodic sequence, with the number of nucleotides $n_{FB} = 377$, we have $\alpha_{min} = 0.82577$ and $\alpha_{max} = 1.65676$ ($\Delta\alpha = 0.83099$);
(b) for the Rudin–Shapiro quasiperiodic sequence, with the number of nucleotides $n_{RS} = 64$, we have $\alpha_{min} = 0.57357$ and $\alpha_{max} = 3.61395$ ($\Delta\alpha = 3.04038$);
(c) for the DNA Ch22 sequence, with the number of nucleotides $n_{Ch22} = 64$, we have $\alpha_{min} = 0.39656$ and $\alpha_{max} = 2.78862$ ($\Delta\alpha = 2.3920$).

Therefore, from the values of $\Delta\alpha$ shown above, the Fibonacci structures is the less randomic when it is compared with the Rudin–Shapiro and the Ch22 one.

Let us consider again the energy spectra depicted in Fig. 7.1. The bandwidth Δ_i for the nth number of nucleotides is given by

$$\Delta_1 = E_2 - E1 \Longrightarrow E_2 = E_1 + \Delta_1, \tag{91}$$

$$\Delta_2 = E_4 - E_3 \Longrightarrow E_4 = E_3 + \Delta_2, \tag{92}$$

$$\vdots$$

$$\Delta_i = E_{2i} - E_{2i-1} \Longrightarrow E_{2i} = E_{2i-1} + \Delta_i, \tag{93}$$

where E_1 and E_2 are the energy values of the bottom and the top of the first band of energy (counting from the smallest to the largest value of the energy). Also, E_3 and E_4 are the energy value of the bottom and the top of the second band of energy, and so on, for increase n. We take the level density inside each band to be constant, and the same for all bands in a given hierarchy. In this case, a fractal or multifractal emerges at the $n \to \infty$ limit. Obviously the number of bands depends on the number of nucleotides as it is shown in Fig. 7.1. In what follows, we consider a normalization in the frequency spectrum, in such a way that the bands stay within the limits 0 and 1.

Within a classical Maxwell–Boltzmann statistics, the partition function Z_{MB} is given by:

$$Z_{MB} = \int_0^\infty \rho(E) \exp(-\beta E_i) dE \tag{94}$$

where we have considered a unit Boltzmann's constant, i.e. β equal to $1/T$. Also, we take the density of states $\rho(E) = 1$. We justify the use of the classical Maxwell–Boltzmann statistics, as ours first example, instead of the one appropriated for a fermionic system because, as explained in Ref. [206], the electrons behave as Boltzmann particles once the gaps in their energy spectra are becoming smaller than the Fermi temperature T_F (which is our case). The Fermi–Dirac statistics case will be the topic of a later Sections 7.3 and 7.4.

After some calculations, it is easy to write the partition function Z_{MB} as

$$Z_{MB} = \frac{1}{\beta} \sum_{i=1,3,\ldots}^{2N-1} (1 - e^{-\beta\Delta_i}) \exp(-\beta E_i). \tag{95}$$

Note that it is only necessary to know the distribution of the energy spectrum of a given multifractal system to calculate the partition function [200]. Once we know the partition function, it is possible to calculate the specific heat using:

$$C(T) = \frac{\partial}{\partial T} \left[T^2 \frac{\partial \ln Z_{MB}}{\partial T} \right], \tag{96}$$

which can be written as

$$C(T) = 1 + \frac{\beta f_n}{Z_{MB}} - \frac{g_n^2}{Z_{MB}^2}. \tag{97}$$
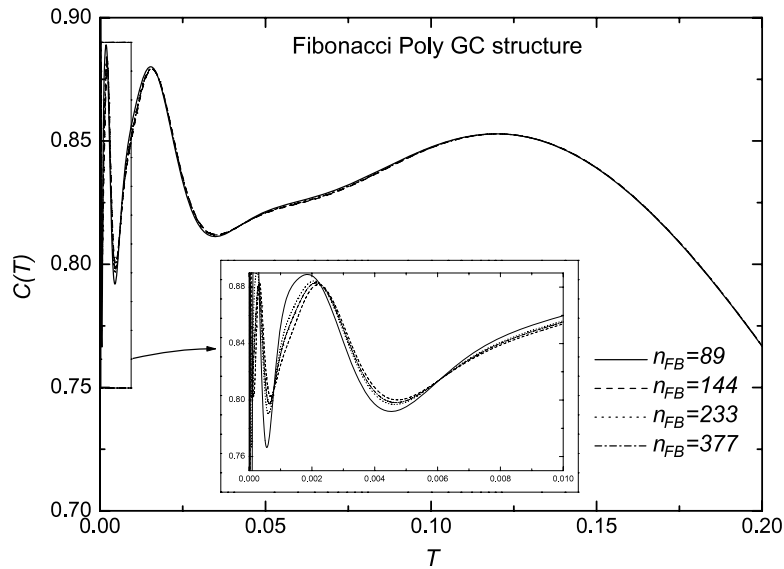
Here

$$f_n = \sum_{i=1,3,\ldots}^{2m-1} [E_i^2 e^{-\beta E_i} - E_{i+1}^2 e^{-\beta E_{i+1}}], \tag{98}$$

and

$$g_n = \sum_{i=1,3,\ldots}^{2m-1} [E_i e^{-\beta E_i} - E_{i+1} e^{-\beta E_{i+1}}]. \tag{99}$$

Fig. 7.2. Specific heat spectra $C(T)$ vs temperature (T) plot corresponding to the 10th, 11th, 12th and 13th (89, 144, 233, and 377) Fibonacci poly(GC) sequence generation (number of nucleotides) DNA models. The inset shows the rather interesting oscillatory behavior of the specific heat spectra.

Therefore, once we know the electronic energy spectra of a given DNA chain, we can determine the associated specific heat by using (97).

Fig. 7.2 shows the electrons' specific heat $C(T)$ as a function of the temperature T for the Fibonacci poly(CG) DNA structure. It is possible to see that these spectra are almost independent of the Fibonacci's generation number n_{FB}. More important, the inset of this figure shows the oscillatory behavior of the specific heat for low temperatures, with two classes of oscillations, one for the *even* and the other for the *odd* generation numbers of the sequence, the amplitude of the even oscillations being slight bigger than the amplitude of the odd one. The number of times that the specific heat oscillate for a given generation number n_{FB} is $(n_{FB} - 2)/2$ for n_{FB} even, and $(n_{FB} - 1)/2$ for n_{FB} odd.

These behaviors are illustrated in Fig. 7.3(a) and Fig. 7.3(b), where are depicted *log* plots of the specific heat against the temperature, corresponding to the even and odd generation numbers of the Fibonacci sequence, respectively. This peculiar behavior is some kind of signature, with no counterpart in the other quasiperiodic structures, and should be connected to the properties found for other Fibonacci spectra [200]. The log-periodic behavior of the specific heat shows a mean value d, around it $C(T)$ oscillates log-periodically, although this value is not related with the fractal dimension of the Fibonacci quasiperiodic structure because our specific heat spectra are not strictly invariant under changes of scales. Instead, this mean value d can be given approximately by the so-called spectral dimension (the exponent of a power law fit of the integrated density of states), which in this case is approximately equal to 0.8. It is also associated to the minimum singularity exponent α_{min} in the Fibonacci multifractal $f(\alpha)$ spectrum. Furthermore, the self similarity of the specific heat spectra is bigger for sequences with a difference of two in the generation process. Note that the specific heat properties in log-scale are basically controlled by the behavior of the low energy region at the scale considered (i.e., each oscillation can be considered as a change of scale in the spectrum). In this sense, at a high scale defined by the Fibonacci's generation number n_{FB}, the low energy region would be controlled by the generation number $(n_{FB} - 2)$; at a smaller scale, the low energy region would be controlled by the generation number $(n_{FB} - 2) - 2 = n_{FB} - 4$ and so on.

Fig. 7.4 shows the specific heat spectrum against the temperature for a DNA molecular structure modeled by the Rudin–Shapiro sequence. In this case there are oscillations with amplitude very superior to those found in the Fibonacci case. Moreover, the number of oscillations is not directly proportional to the number of generations, and there is no well-defined parity behavior, as in the Fibonacci model. The inset of this figure clearly shows these facts. A similar spectra was found for the genomic Ch22 DNA structure, as it is depicted in Fig. 7.5, which shows random oscillations with amplitudes slightly bigger to those obtained for the Rudin–Shapiro chain.

In all situations studied here, for high temperatures $(T \to \infty)$, the specific heat for all generation numbers n_{FB} converges and decays as T^{-2}. This asymptotic behavior is mainly due to the fact that we have considered our system bounded. On the other hand, when $(T \to 0)$, the specific heat display an oscillation profile, no matter the model is considered.

7.2. Maxwell–Boltzmann statistics: the double-strand DNA structure

Consider the tight-binding Hamiltonian appropriated to the double-strand DNA molecule, as described in Section 3.3, whose energy spectrum, as measured by their equivalent bandwidth Δ, is depicted in Fig. 3.5(a) (Fibonacci case), 3.5(b) (Rudin–Shapiro case) and 3.5(c) (Ch22 human chromosome) [207]. Their multifractal behavior, obtained from the analysis of the function $f(\alpha)$ as in the previous section, can be summarized as follows:
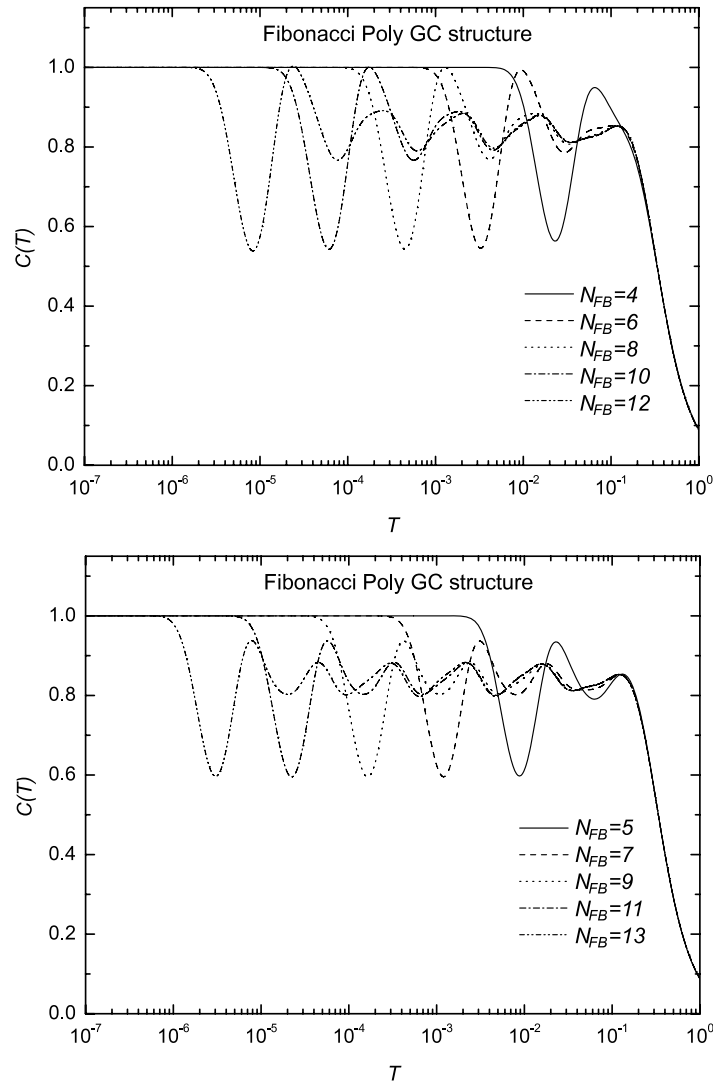
Fig. 7.3. Specific heat log-periodic spectra for the Fibonacci poly(GC) DNA model: (a) even Fibonacci generation number (n_{FB} = 4, 6, 8, 10, and 12); (b) odd Fibonacci generation number (n_{FB} = 5, 7, 9, 11, and 13).
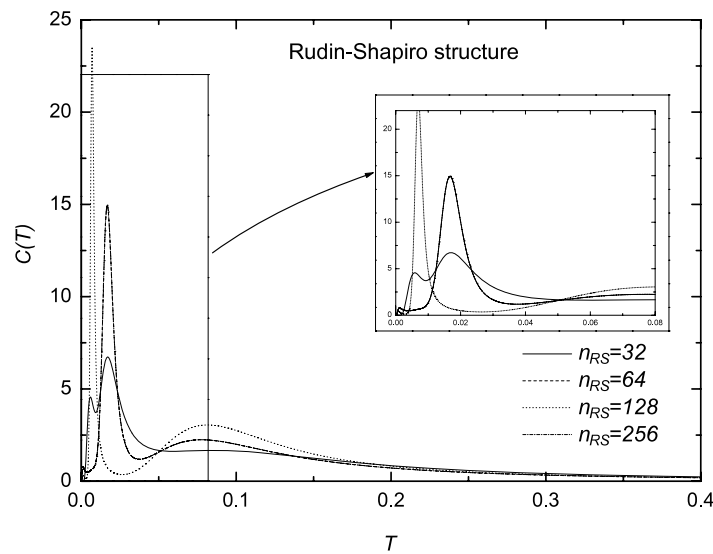
Fig. 7.4. Specific heat for the Rudin–Shapiro quasiperiodic DNA model as a $C(T)$ vs temperature (T) plot for n_{RS} = 32, 64, 128, and 256 nucleotides. The inset shows the oscillatory behavior of the specific heat spectra.
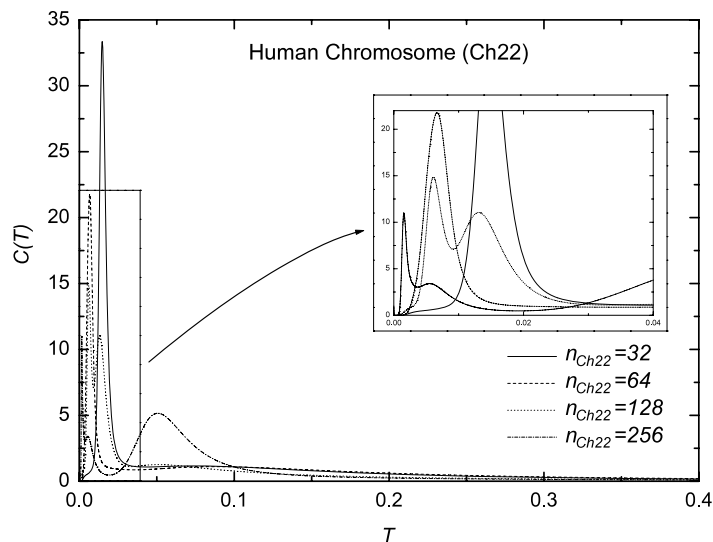
Fig. 7.5. The same as in Fig. 7.1, but for the Ch22 genomic DNA model.

(a) for the quasiperiodic Fibonacci sequence, we have $\alpha_{min} = 0.835$ and $\alpha_{max} = 1.858$ ($\Delta\alpha = 1.023$);
(b) for the quasiperiodic Rudin–Shapiro sequence, we have $\alpha_{min} = 0.743$ and $\alpha_{max} = 3.821$ ($\Delta\alpha = 3.078$);
(c) for the human chromosome 22 (Ch22) DNA chain, we have $\alpha_{min} = 0.414$ and $\alpha_{max} = 3.612$ ($\Delta\alpha = 3.198$).

From the above, we can infer that regarding the degree of randomness of the band width distribution for each structure, the RS sequence is more close related to the Ch22 structure than the FB one for this DNA model.

We address now the specific heat obtained from the spectra shown in Fig. 3.5, following the lines of the previous section, after calculating the partition function for n nucleotides spectrum, using a Maxwell–Boltzmann statistics as yielded by Eq. (95). In Fig. 3.5 each spectrum, for a fixed number of nucleotides n, has m allowed continuous bands. We consider the level density within each band to be constant.

Fig. 7.6(a) shows the electronic specific heat spectra for the Fibonacci DNA chains, corresponding to its 10th (number of nucleotides $n_{FB} = 89$), 11th (number of nucleotides $n_{FB} = 144$), 12th (number of nucleotides $n_{FB} = 233$), and 13th (number of nucleotides $n_{FB} = 377$) generation numbers, as a function of the temperature. As expected, for the high-temperature limit ($T \rightarrow \infty$), the specific heat for all cases converges and decays as T^{-2}, as a consequence of the existence of a maximum energy value in the spectrum (once the spectrum is bounded). As the temperature decreases, the specific heat increases up to a maximum value. The corresponding temperature for this maximum value depends on the number of nucleotides n_{FB}, although one can see a clear tendency for a common temperature value as n_{FB} increases. After the maximum value, the specific heat falls into the low temperature region. In this region it starts to present a non-harmonic small oscillation behavior, as shown in the inset of Fig. 7.6(a). This can be interpreted as a superposition of Schottky anomalies corresponding to the scales of the energy spectrum. Furthermore, the profiles of these oscillations define also two classes of oscillations, as far as the parity (even or odd) of the generation number of the Fibonacci sequence is concern, as in the single-strand case. These behaviors are better illustrated in 7.6(b) and (c), where are depicted log-plots of the specific heat against the temperature, showing clearly a log-periodic behavior, i.e., $C_n(T) = AC_n(aT)$, where A is a constant, and a an arbitrary number. The mean value d, around it $C(T)$ oscillates log-periodically, can be given approximately, as in the previous case, by the so-called spectral dimension associated to the minimum singularity exponent α in the multifractal curve $f(\alpha)$, namely $\alpha_{min} = 0.835$. Of course, the number of oscillations observed in the specific heat spectra is related to the number of nucleotides n_{FB}, once n_{FB} depends on the hierarchical generation of the Fibonacci sequence (more oscillations appear as n_{FB} increases).

A different scenario appears when one consider the other quasiperiodic structure studied here (i.e., modeling the DNA molecule by the RS sequence), which is depicted in Fig. 7.7. Similarly to the Fibonacci case, in the limit when $T \rightarrow \infty$, the specific heat goes to zero as T^{-2} for all values of n_{RS}. Also there are oscillations in the region near to $T \rightarrow 0$ (which are better shown by the inset of the figure). Although these oscillations can be interpreted as Schottky anomalies, as in the Fibonacci case, they do not have the same standard of behavior, i.e., two groups of oscillations corresponding to even and odd generation numbers of the sequence. Additional differences should be pointed out. In this case there are oscillations with amplitude very superior to those found in the Fibonacci case. More important, the log-plot does not show a log-periodic behavior. Instead, it shows an erratic-like profile, which can be attributed to the more disordered structure of the Rudin–Shapiro sequence. Therefore, apart of the common asymptotic behavior of the specific heat when $T \rightarrow \infty$ and $T \rightarrow 0$, there is no other connection between the Fibonacci and Rudin–Shapiro DNA chains considered here, regarding their specific heat spectra.

Finally, for comparison purposes, we present in Fig. 7.8 the specific heat behavior of the human chromosome Ch22 chain. As in the two previous cases, in the limit when $T \rightarrow \infty$, the specific heat goes to zero as T^{-2} and also there are oscillations in
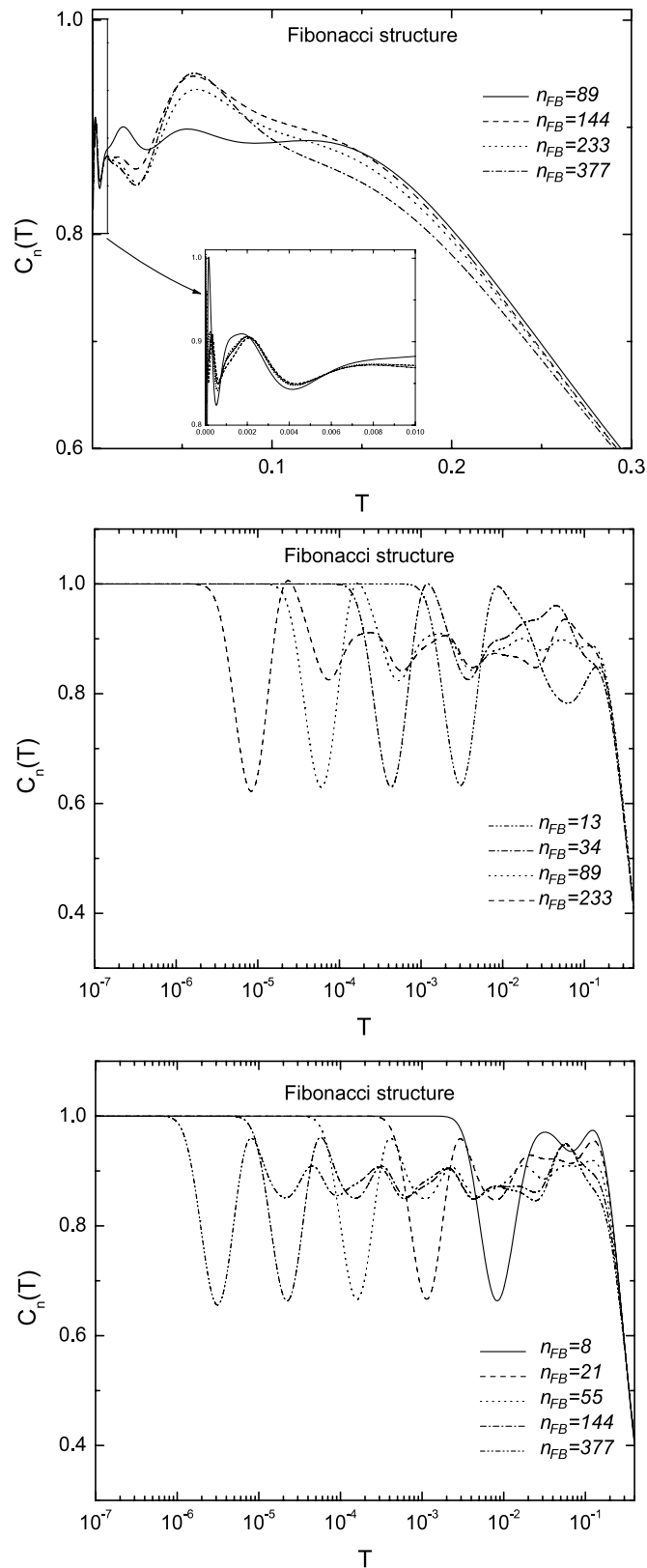
Fig. 7.6. (a) Specific heat (in units of k_B) versus temperature (in units of Δ, the sum of all allowed energy regions in the band structures) for the Fibonacci DNA chain. The inset shows the low-temperature behavior of the specific heat. (b) Log-periodic behavior of the specific heat for the even (6th, 8th, 10th, and 12th generation, respectively) Fibonacci DNA chain. (c) Log-periodic behavior of the specific heat for the odd (5th, 7th, 9th, 11th, and 13th generation, respectively) Fibonacci DNA chain.

the low temperature region due to Schottky anomalies (which are better shown by the inset of the figure). One can see clearly that the overall behavior of the specific heat of Ch22 DNA chains is very close to the specific heat of the Rudin–Shapiro one,
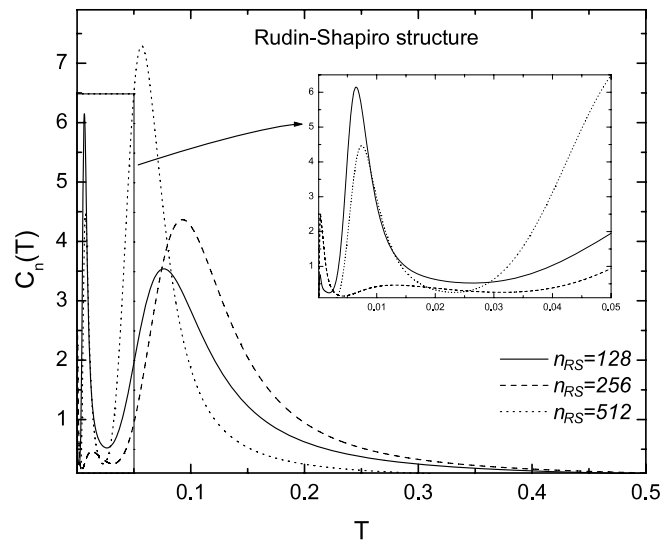
Fig. 7.7. Specific heat (in units of k_B) versus temperature (in units of Δ, the sum of all allowed energy regions in the band structures) for the Rudin–Shapiro DNA chain, corresponding to its 8th (number of nucleotides $n_{RS} = 128$), 9th (number of nucleotides $n_{RS} = 256$), and 10th (number of nucleotides $n_{RS} = 512$) generation number. The inset shows the low-temperature behavior of the specific heat.
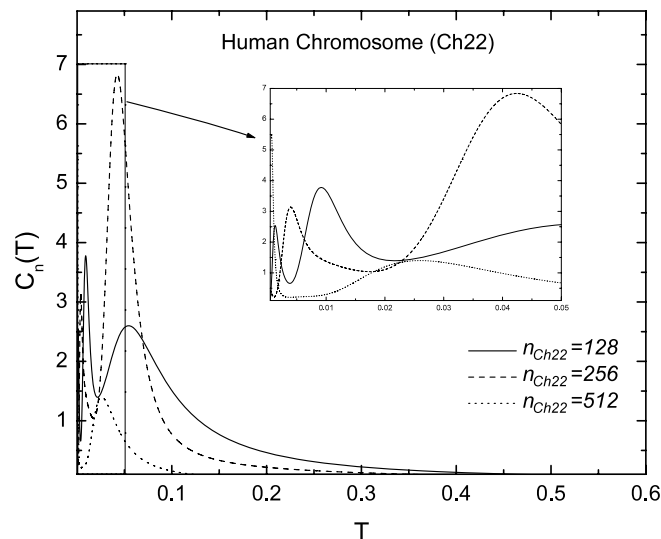

Fig. 7.8. Specific heat (in units of k_B) versus temperature (in units of Δ, the sum of all allowed energy regions in the band structures) for the Ch22 DNA chain, corresponding to the number of nucleotides $n_{Ch22} = 128$, 256, and 512. The inset shows the low-temperature behavior of the specific heat.

in contrast with the Fibonacci case. For example, Ch22 and Rudin–Shapiro specific heats both present similar amplitude of oscillations, as well as an erratic-like behavior in their log-plots, instead of the log-periodic behavior found in the Fibonacci case.

Before concluding, let us comment on a possible connection between this present results with those of Mrevlishvili and collaborators [208,209]. Their experimental data show oscillations of the specific heat at low temperature, which are qualitatively similar to our present numerical theoretical results. They attribute their results to the non-crystalline order of the DNA samples which may be modeled, as we have shown here, by quasiperiodic systems.

7.3. Fermi statistics: the single-strand DNA structure

The multifractal energy spectrum of the FB and RS sequences, for both single- and double-strands DNA-like sequences, was obtained in previous sections, and it will be taken into account to determine the specific heat spectra by using the quantum-mechanical Fermi–Dirac statistics. Since the spin degree will not be considered in this work, each occupied quantum state can support only one particle. According to the Fermi–Dirac statistics, the average occupation number of each state is given by

$$\langle n_i \rangle = \frac{1}{1 + \exp[\beta(E_i - \mu)]},$$
(100)
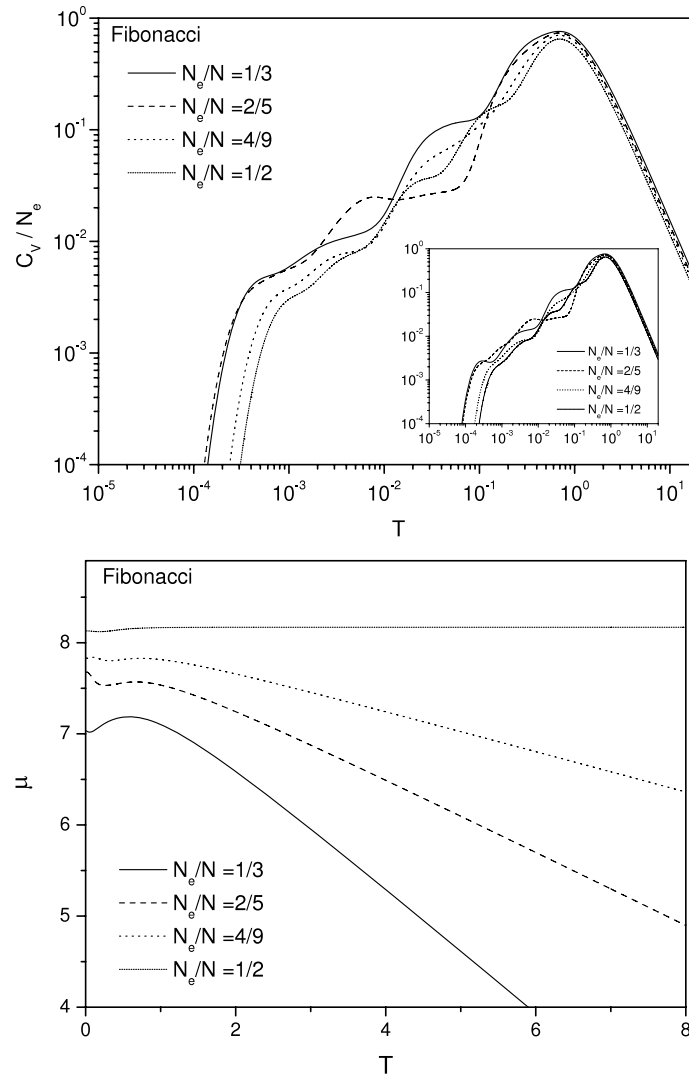
Fig. 7.9. (a) Log–log scale of the fermionic specific heat at constant volume (in units of N_e) versus the temperature T for the 14th generation of the Fibonacci DNA chain, corresponding to $n_{FB} = 610$ nucleotides. Four different concentrations are analyzed. The inset in Fig. 7.9(a) depicts the case for the 15th generation of the Fibonacci DNA chain, corresponding to $n_{FB} = 987$ nucleotides. (b) Chemical potential μ versus the temperature T.

where μ is the chemical potential, which can be computed as a function of temperature and band filling from

$$N_e = \sum_{i=1}^{N} \langle n_i \rangle, \tag{101}$$

from which $\mu(N_e/N, T)$ can be extracted by numerical methods. Here, N_e is the number of non-interacting Fermi particles (electrons), while N is the total number of one-particle accessible states (electrons and holes).

The average internal energy is obtained from

$$U(N_e/N, T) = \sum_{i=1}^{N} E_i \langle n_i \rangle, \tag{102}$$

where the temperature dependence of the chemical potential $\mu(N_e/N, T)$ is explicitly taken into account.

We compute the specific heat at constant volume by differentiating $U(N_e/N, T)$ with respect to the temperature T, i.e., $C_V = dU(N_e/N, T)/dT$. It is then straightforward to calculate the fermionic specific heat yielding [210]

$$C_V = \frac{1}{4T^2} \left[\sum_i E_i^2 \cosh^{-2}[(E_i - \mu)/2T] - \frac{\left[\sum_i E_i \cosh^{-2}[(E_i - \mu)/2T] \right]^2}{\sum_i \cosh^{-2}[(E_i - \mu)/2T]} \right]. \tag{103}$$

Fig. 7.9(a) shows a log–log plot of the electronic specific heat spectra at constant volume (in units of N_e, the number of non-interacting Fermi particles) versus the temperature T for the 14th generation of the Fibonacci DNA chain, corresponding
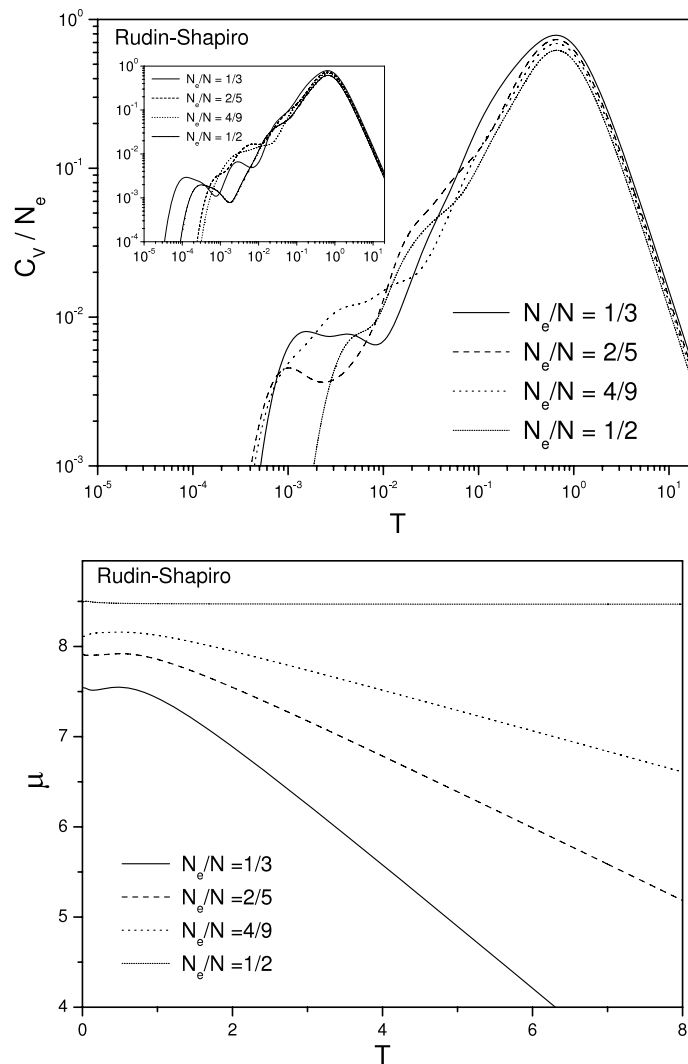
Fig. 7.10. Same as in Fig. 7.9, but for the 10th generation of the Rudin–Shapiro DNA chain, corresponding to $n_{RS} = 512$ nucleotides. The inset in Fig. 7.10(a) depicts the case for the 11th generation of the Rudin–Shapiro DNA chain, corresponding to $n_{RS} = 1024$ nucleotides.

to $n_{FB} = 610$ nucleotides. Several values of the band fillings N_e/N are considered, and indicated in the figure. For the high temperature limit ($T \to \infty$), the specific heat for all cases converges and decays with T^{-2}. As the temperature decreases, the specific heat increases up to a maximum value, the corresponding temperature for this maximum value depending on the number of band fillings N_e/N, although one can see a clear tendency for a common temperature value as N_e/N increases, independently of the occupation number ratio. After the maximum value, the specific heat falls into the low temperature region and starts, due to the fractality of the energy spectrum, a complex pattern of log-periodic oscillations which signals the discrete scale invariance of the spectrum at the vicinity of the Fermi energy. These oscillations occur around a linear trend (in log–log scale), whose power-law behavior is $C_V \propto T^{\phi_{FB}}$, with $\phi_{FB} = 0.7385$, lasting until the temperature reaches a value around 10^{-3}. At this point, a phase transition (in the sense of a oscillatory regime) occurs, and the specific heat falls again linearly with T. The inset of this figure considers the 15th generation of the Fibonacci DNA chain, corresponding to $n_{FB} = 987$ nucleotides. From there we can see a larger number of oscillations of the specific heat for low T (in general the number of oscillations of the specific heat for fractal spectra increases with the order of the generation of the fractal). Besides, the oscillatory regime disappears at a lower temperature, when compared to the 14th generation of the Fibonacci DNA chain.

In Fig. 7.9(b), the profile of the chemical potential $\mu(T, N_e/N)$ against the temperature T is presented, for a Fibonacci DNA chain, considering the occupation ratios $N_e/N = 1/2, 4/9, 2/5$ and $1/3$. For lower values of T, there is a transient period, on which the chemical potential reaches a maximum value, and then starts to decrease (in all cases but $N_e/N = 0.5$) linearly, as the ratio N_e/N decreases. For $N_e/N = 0.5$, the chemical potential has a constant value. This is an expected feature, since the chemical potential is a measure of the energy per particle, for a given entropy.

A similar scenario appears when one consider the other quasiperiodic structure studied, modeling the DNA molecule by the Rudin–Shapiro sequence, whose log–log plot of the specific heat at constant volume (in units of N_e) is depicted in Fig. 7.10(a), considering its 10th generation (which means 512 nucleotides). Its profile is very similar to those of Fig. 7.9, when

one consider the same band fillings N_e/N. There is a transient region where the C_V oscillates non-harmonically around an inclined straight line, $C_V \propto T^{\phi_{RS}}$, with $\phi_{RS} = 1.01$, and then suddenly it falls to zero, linearly with T. However, now this decrease depends more strongly on the band fillings N_e/N considered. The inset shows the case for the Rudin–Shapiro's 11th generation, corresponding to $n_{RS} = 1024$ nucleotides. The chemical potential for this sequence is shown in Fig. 7.10(b), with qualitative behavior similar to the FB case.

This work would not be complete if we did not compare our results with a real system. For this purpose, the log–log plot of the specific heat at constant volume (also in units of N_e) for the Ch22 chromosome, analyzed through a Fermi–Dirac statistics, is depicted in Fig. 7.11(a). Again, the specific heat falls to zero when $T \to \infty$, but now in a slightly higher ratio. Also, after the maximum value of C_V is reached, in the low temperature region the specific heat falls roughly linearly with T, and at $T = 0.5 \times 10^{-2}$, it falls more rapidly with T. Note that in this case there is less oscillations when $T \to 0$ when compared to the quasiperiodic structures. Probably this is due to the fact that, in contrast to a real fractal, human chromosomes present a common compositional structure with two characteristic scales, the large one corresponding to long, homogeneous DNA segments (the isochores), and the other one to small and medium scale genomic elements. The inset presents the case for the human chromosome Ch22 with 1024 nucleotides.

The chemical potential, depicted in Fig. 7.11(b), resembles strongly the RS one, which means that the energy distribution per particle is very similar in these two cases. This qualitative resemblance is an indication that a real DNA chain can, at least in principle, be modeled through substitutional sequences, like FB and RS. Also, the lack of an oscillatory behavior around a medium value (the spectral or fractal dimension of the system), a common feature presented in previous works, clearly indicates that the statistics considered (Fermi–Dirac), which forbid more than one particle per state (excluding the spin), plays a decisive role on the collective behavior of electrons propagating in real and modeled DNA chains.

7.4. Fermi statistics: the extended double-strand DNA structure

Consider now the extended double-strand DNA structure discussed in Section 3.4. The thermodynamic behavior can be now directly obtained from the electronic density of states depicted in Fig. 3.7, following the lines presented in the previous section.

Fig. 7.12 depicts a log–log plot of the normalized specific heat spectra at constant volume (in units of the number of non-interacting Fermi particles N_e times the Boltzmann's constant k_B) versus the temperature T for the Fibonacci sequence (solid line), the Rudin–Shapiro sequence (dashed line), and the DNA human chromosome 22—Ch22 (dotted line). Three values of the band fillings N_e/N are considered, namely $N_e/N = 0.9$ (Fig. 7.12(a)), 0.6 (Fig. 7.12(b)), and 0.4 (Fig. 7.12(c)), for all sequences studied.

Broadly speaking, Fig. 7.12 shows that an increased disorder (Fibonacci $\to$ Rudin–Shapiro $\to$ Ch22) gives rise to a structured specific heat C_V, with a different band filling N_e/N and temperature T dependence. Although the existence of a structure in the DNA heat capacity at low temperatures has already being demonstrated experimentally, it was strictly assigned to the difference in hydration and/or structural transitions related to the various DNA conformations. Our theoretical/computational analysis indicates that only the C_V behavior of a more disordered nucleotides arrangement can approach that of the human chromosome 22. This last finding supports the visionary and historical idea of Schrödinger [211], in which he predicted that a gene or perhaps a whole chromosome thread represents an aperiodic solid.

Furthermore, at these band fillings ($N_e/N = n/10, n = 4, 6, 9$) the Fermi energy falls in a dense region of the energy spectrum. Therefore, there are empty states closer to the ground state, and these can be thermally occupied even at very low temperatures. For a periodic infinite crystal, the energy spectrum yields a linear temperature dependence (in the low-temperature regime) of the electronic specific heat. However, although quasiperiodic systems may not being classifiable in the nonlinear physics context, they do exhibit a multifractality in their spectra and, instead of the expected linear temperature behavior, the internal energy scales as a power-law $U - U_0 \propto T^{1+\phi}$, and consequently $C_V \propto T^{\phi}$. In our case, these ϕ exponents are equal to 0.12 (Fibonacci sequence), 0.15 (Rudin–Shapiro sequence) and 0.23 (Ch22 DNA finite segment), no matter the value of the band fillings N_e/N. This universality class of the specific heat decay exponent at low-temperature, as far as the band fillings N_e/N are concerned, can be understood on basis of a simple multifractal scale argument. For small thermal excitations, each particle can absorb an energy of the order of T. The number of particles that can be excited corresponds to the number of states in an energy range of the order of T around the Fermi energy. Therefore, the observed specific heat exponents ϕ lies within the range of values of the singularity strength exponent $(\alpha_{min}, \alpha_{max})$ defined by the so-called multifractal $f(\alpha)$ spectrum [212], which in turn gives support to the above scaling analysis, unveiling a relationship between the low-temperature power-law decay of the electronic specific heat of a molecular system with multifractal spectrum and the underlying energy distribution singularities, disregarding the values of N_e/N and, of course, any finite size effect. This finding may provide a useful tool for the analysis of the low-temperature thermodynamic behavior of more robust protein models modeled by a quasiperiodic system.

There are some other features in the temperature dependence of the specific heat that deserve to be stressed:

(a) at temperatures around the normal human being temperature $T_{NHB} = 310$ K a striking difference is observed: while the electronic specific heat for the Fibonacci sequence shows a peak, regardless the value of the band filling N_e/N, the same do not occur for the RS and Ch22, which have similar behavior;

(b) the RS and Ch22 structures show a peak at the temperature around 100 K with similar profiles;
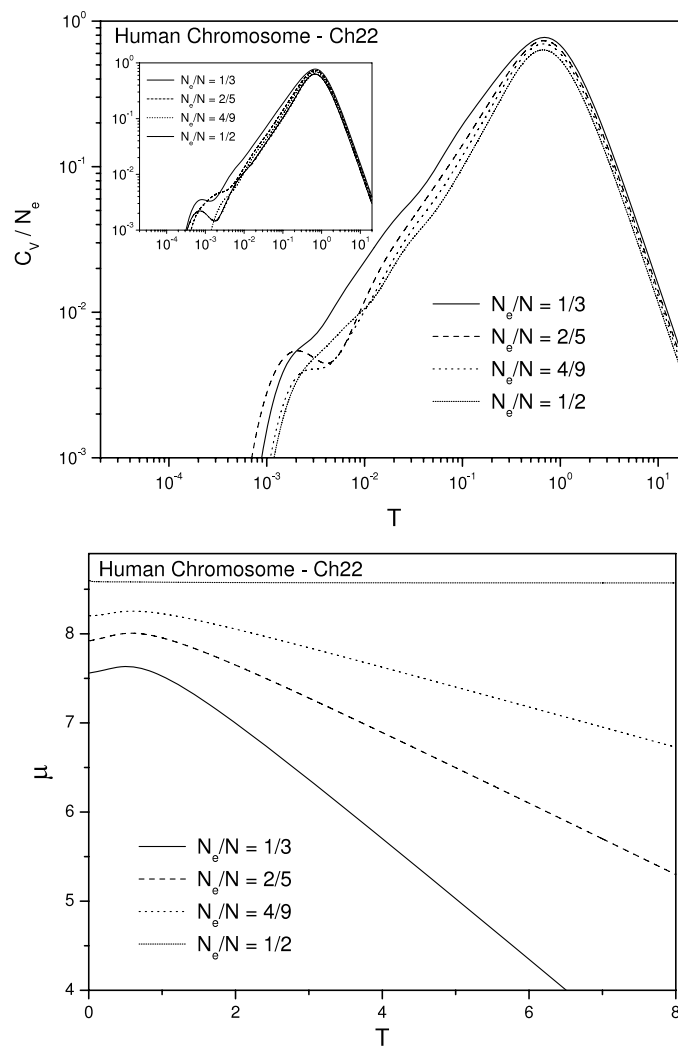
Fig. 7.11. Same as in Fig. 7.9, but now for the human chromosome Ch22 considering 512 nucleotides. The inset in Fig. 7.11(a) depicts the case for the human chromosome Ch22 with 1024 nucleotides.

(c) at low temperature the electronic specific heat falls linearly to zero, faster for the Fibonacci sequence than for the Rudin–Shapiro one, which in turn is faster than the DNA human chromosome 22.

7.5. Non-extensive thermodynamics

It is by now well established that the powerful standard Boltzmann–Gibbs (BG) statistical mechanics and the associated thermodynamics are valid when certain conditions are satisfied. The typical situation occurs for microscopic dynamics exhibiting strong chaos i.e., positive largest Lyapunov exponent and, consistently, the usual thermodynamic extensivity. This is the scenario which typically occurs for short-range-interacting many-body Hamiltonian systems.

On the other hand, a vast class of natural and artificial systems exists for which the largest Lyapunov exponent vanishes, situation which is referred to as weak chaos. Weak chaos is typically associated with power-law, instead of exponential, sensitivity to the initial conditions and relaxations, fractal or multifractal occupation of phase space and thermodynamic nonextensivity, i.e., phenomena involving long range interactions (see [213–215] for recent reviews).

Taking into account the above requirements, a possible generalization of BG statistical mechanics was proposed many years ago by Tsallis [216], on the basis of the following distribution

$$p_q(E) = \left[1 - (1 - q)\beta E \right]^{1/(1-q)}, \tag{104}$$

where p_q is the probability of the system has energy E, $\beta = 1/k_B T$, and q, the entropic index (intimately related to and determined by the microscopic dynamics), characterizes the degree of nonextensivity, a number which is believed to have some relationship to the intrinsic characteristics of the system. When $q \rightarrow 1$ that expression recover the well-known
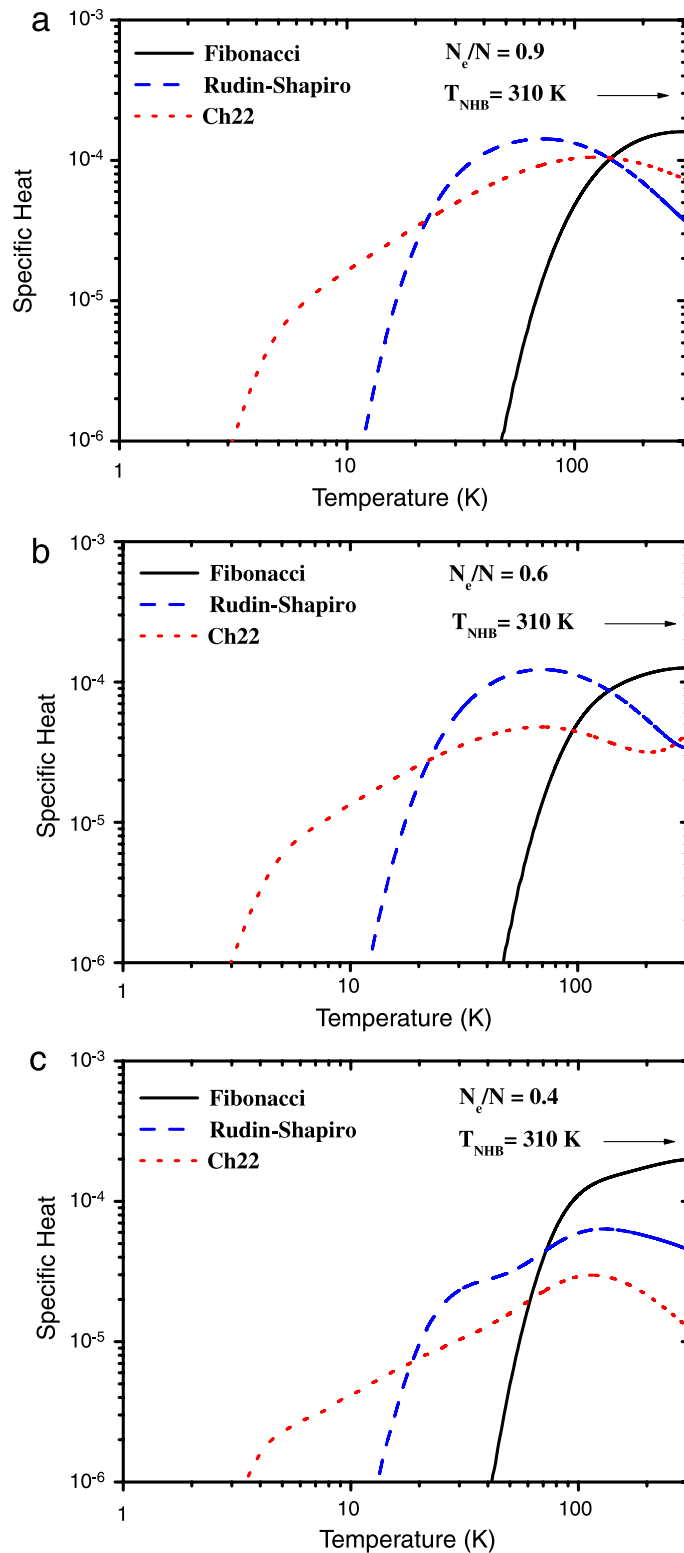
Fig. 7.12. (Color online) The log–log plot of the electronic specific heat spectra against the energy E (in eV) for the Fibonacci sequence (solid line), the Rudin–Shapiro sequence (dashed line), and the DNA human chromosome 22–Ch22 (dotted line). Three values of the band fillings N_e/N are considered, namely (a) $N_e/N = 0.9$; (b) $N_e/N = 0.6$; (c) $N_e/N = 0.4$. The limit of the temperature scale (right-hand side) represents the normal human body temperature $T_{NHB} = 310$ K.

Boltzmann–Gibson distribution. The entropy of the system follows [216]:

$$S_q(E) = k_B \frac{\sum_{i=1}^{W} p_i^q - 1}{1 - q}, \tag{105}$$

where W is the total number of microscopic possibilities of the system. Observe that for the $q < 0$ case, care must be taken to exclude all those possibilities whose probability is not strictly positive; otherwise $S_q(E)$ would diverge. Such care is not necessary for $q > 0$. This generalization of BG statistical mechanics is usually referred to as nonextensive statistical mechanics. Its denomination nonextensive comes from the following property: if we have two probabilistically independent systems A and B, i.e., $p_{ij}(A + B) = p_i(A)p_j(B)$, we straightforwardly verify that

$$S_q(A + B) = S_q(A) + S_q(B) + (1 - q)S_q(A)S_q(B). \tag{106}$$

Consequently, $q = 1$, the BG case, corresponds to extensivity, whereas $q < 1$ ($q > 1$) corresponds to superextensivity (subextensivity), where the nonnegativity of q has been taken into account.

Within nonextensive statistical mechanics, many of the above cited anomalous systems have found a frame of interpretation. In particular, several authors has recently reported investigation of thermodynamical properties associates with systems that exhibit long-range correlated structures, with hierarchical or fractal structure. The first results [217] showed that the specific heat of quasiperiodic spin chains presents logarithmic-periodic oscillations in the low temperature region. Similar results were found in the specific heat properties associated to hierarchical structures [218] or to the specific heat corresponding to the Heisenberg model with quasiperiodic exchange couplings at some circumstances [219]. All these examples share in common that the corresponding energy spectra show fractal properties.

The energy spectra with fractal structure present an additional interest: quasiperiodic sequences, often used to model quasicrystals, are known to have energy spectra with fractal properties, similar in structure to fractal sets of Cantor type. This is the reason why the results obtained from studies performed on energy spectra of Cantor type have been used to explain the properties of the specific heat of Fibonacci sequences, either modeled as one-dimensional (1D) tight-binding Hamiltonians (as discussed previously in this review) or as superlattices [220]. Also, the properties of the specific heat associated to fractal spectra presents similar properties when quantum, fermionic, or bosonic statistics are considered [221,222].

This sub-section reports the study of the electronic specific heat at low temperature, considering nonextensive distribution of long-range correlated quasiperiodic (Fibonacci and Rudin–Shapiro types) DNA molecules, as well as the real genomic DNA sequence. Our theoretical model is an effective tight-binding Hamiltonian describing one electron moving in a double-strand DNA molecule, with a single orbital per site and nearest-neighbor interactions, as discussed in Section 3.3.

Defining the internal energy as [223]

$$U \equiv \sum_{i}^{W} p_i^q E_i, \tag{107}$$

the optimization of the entropy defined as $S_q = k \ln_q \Omega$ (Ω is the number of accessible states) yields

$$p_i = \frac{e_q(-\beta E_i)}{Z_q}, \tag{108}$$

with the partition function written as

$$Z_q \equiv \sum_{j=1}^{W} e_q(-\beta E_j). \tag{109}$$

In the above expressions,

$$\ln_q(x) \equiv \frac{x^{1-q} - 1}{1 - q}; \qquad \ln_1 x = \ln x, \tag{110}$$

$$e_q(x) \equiv [1 + (1 - q)x]^{1/(1-q)}; \qquad e_1^x = e^x. \tag{111}$$

After a straightforward calculation, and taking the density of states $\rho(E) = 1$, we can write Z_q as

$$Z_q = \frac{1}{\beta(2 - q)} \sum_{i=1,3,\dots}^{2n-1} \left[e_q(-\beta E_i)^{2-q} - e_q(-\beta E_{i+1})^{2-q} \right], \tag{112}$$

where the index i with odd (even) value refers to the bottom (top) of the energy band. The specific heat can then been derived yielding:

$$C_q(T) = 1 + \frac{\beta f_q}{Z_q} - \frac{g_q^2}{Z_q^2}. \tag{113}$$

Here

$$f_q = \sum_{i=1,3,\dots}^{2n-1} \left[E_i^2 e_q(-\beta E_i)^q - E_{i+1}^2 e_q(-\beta E_{i+1})^q \right], \tag{114}$$

$$g_q = \sum_{i=1,3,\dots}^{2n-1} \left[-E_i e_q(-\beta E_i) + E_{i+1} e_q(-\beta E_{i+1}) \right]. \tag{115}$$
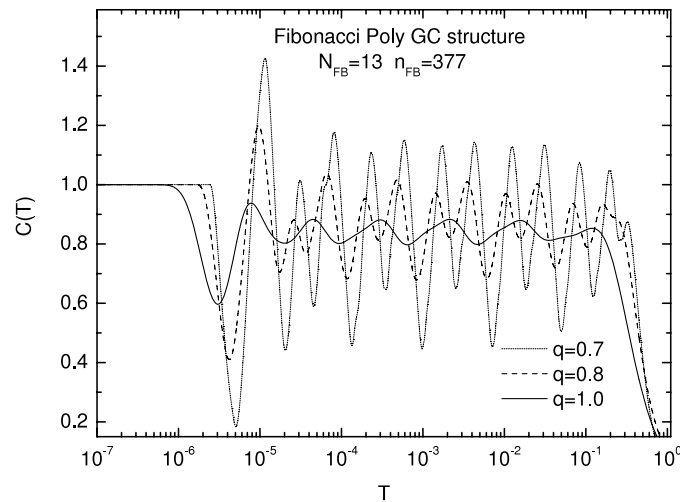
Fig. 7.13. Specific heat as a function of the temperature T in logarithmic scale corresponding to a Fibonacci quasiperiodic DNA obtained for different values of the entropic index q. We have considered energy spectra corresponding to the 13th Fibonacci generation, which means a number of nucleotides $n_{FB} = 377$.

We address now the specific heat spectra obtained in Eq. (113). In Fig. 7.13, we show several specific heats $C_q(T)$ for a Fibonacci quasiperiodic DNA obtained for different values of the entropic index q. We focus our attention in the low temperature region, where the specific heat spectra start to present an oscillatory behavior. This can be interpreted as a superposition of Schottky anomalies corresponding to the scales of the energy spectrum [224]. Although the number of oscillations observed in the spectra is related to the number of nucleotides n_{FB}, once n_{FB} depends on the hierarchical generation of the Fibonacci sequence (more oscillations appear as n_{FB} increases), we consider the energy spectra corresponding to the 13th Fibonacci generation, which means a number of nucleotides $n_{FB} = 377$. In general, we see that when q decreases, the oscillations become more pronounced, as expected. As a remark, we may notice that different values of q might corresponds to different (multi) fractal structures. An illustration of such behavior can be seen in nonlinear unimodal maps, where an analytic connection exists between the entropic index q and the multifractality [225,226]. A discussion of the effect of the fractal properties of the spectrum in the amplitude of the oscillations of the specific heats $C(T)$ can be found in Ref. [227].

Let us define the separation between consecutive local maxima (or minima) of the specific heat spectra for a given q as [228]:

$$\Delta_q = \log_{10} T_{i+1} - \log_{10} T_i, \tag{116}$$

where T_i stands for the temperature value for which $C(T)$ reaches its ith local maxima or minima. For $q \neq 1$ (the nonextensive case), the period is constant. As q becomes more and more different of the unity, more wider and well behaved is the distribution of scales presented in the oscillation spectrum, and therefore, one should expect a higher regularity in the corresponding specific heat. When $q = 1$ (the BG case), the period is not a constant value and depends on the particular oscillation considered. Furthermore, it leads to a wider distribution of periods, because of the presence of a larger diversity of scales.

Similarly, let us define the amplitude of the oscillations as [229]:

$$A_{\pm} = \pm C(T_{\pm}) \mp \langle C(T) \rangle, \tag{117}$$

where $C(T_{\pm})$ stands for a local maximum (minima) of $C(T)$, and $\langle C(T) \rangle$ is the mean value around it $C(T)$ oscillates log-periodically. The mean value $\langle C(T) \rangle$ can be given approximately by the minimum singularity exponent $\alpha_{min} = 0.835$ [207] (see Section 7.2). Besides, when deterministic fractal spectra are considered (like the Fibonacci one), the oscillations of the specific heat, although perfectly regular and periodic, are nonharmonic. This nonharmonicity is reflected in the amplitudes. For decreasing q, the amplitudes start to be nonconstant and depend on the particular oscillation considered. These results suggest that when $q \neq 1$, instead of single values of period and amplitude, we have distributions of these values. On the other hand, for $q = 1$ (the BG case), although the spectrum presents a nonperiodicity behavior, the amplitudes are almost constant, and independent on the particular oscillation considered.

A different scenario appears when one consider the other quasiperiodic structure studied here (i.e., the modeling the DNA molecule by the RS sequence), which is depicted in Fig. 7.14. Similarly to the Fibonacci case, there are oscillations in the region near to $T \to 0$ (which are better shown by the inset of the figure, where a log-plot curve is presented). Although these oscillations can be interpreted as Schottky anomalies, as in the Fibonacci case, the log-plot curve $C(T)$ versus T in the inset does not show a log-periodic behavior. Instead, it shows an erratic-like profile, which can be attributed to the more disordered structure of the Rudin–Shapiro sequence. For comparison purposes, we present in Fig. 7.15 the specific heat behavior of the human chromosome Ch22 chain. As in the two previous cases, the specific heat spectra show oscillations in the low temperature region due to Schottky anomalies (better shown by the inset of the figure), with an erratic-like behavior in their log-plots, instead of the log-periodic behavior found in the Fibonacci case.
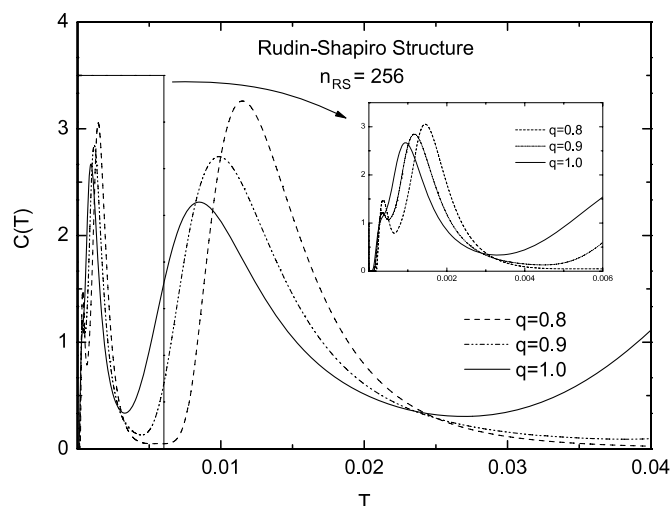
Fig. 7.14. Specific heat as a function of the temperature T corresponding to a Rudin–Shapiro quasiperiodic DNA structure obtained for different values of the entropic index q, and considering a number of nucleotides $n_{RS} = 256$. The inset shows a log-plot curve to emphasize the erratic oscillation profile.
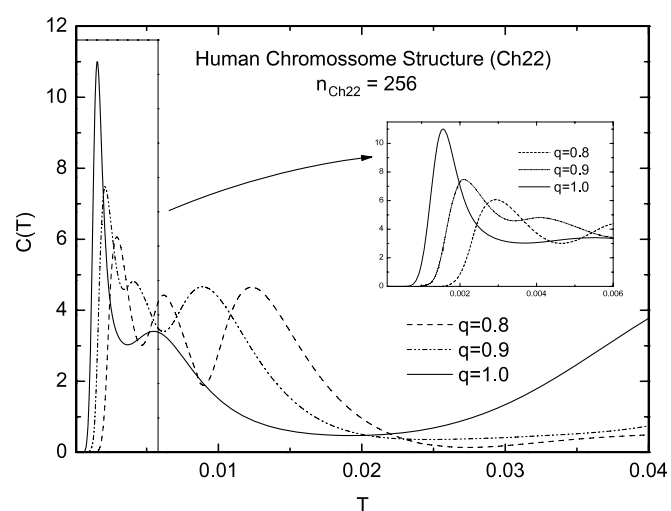
Fig. 7.15. Same as in Fig. 7.13, but for the human chromosome Ch22 sequence.

8. DNA bases crystals

Guanine (G), adenine (A), cytosine (C), and thymine (T) nucleotide bases are the essential building blocks of DNA, which contains the genetic information used to build living cells. Almost ten years after the elucidation of the helical DNA structure, where the coupling of nucleobases through hydrogen bonds and van der Walls forces has a fundamental role, Eley and Spivey [230] argued that $\pi - \pi$ interactions between stacked base pairs in double-stranded DNA could provide a pathway for rapid, one-dimensional charge separation.

London dispersion forces originated from electron correlation in π stacking [231,232] and hydrogen bonding [233–235] of DNA nucleobases affect the structural, electronic, optical, and transport properties of DNA strands and derived nanostructures, being determinant to obtain the features required for technological applications. The DNA nucleobases were mainly studied in vacuum [236–238] and aqueous environments [239–242], with few works being published on their crystals, some focusing on the structural, electronic, and transport properties of guanine crystals [243] and others investigating the dielectric function of anhydrous DNA films [244]. Recently, a new generation of exchange–correlation functionals within the density functional theory (DFT) approach has been employed to provide an improved description of hydrogen bonding and van der Waals interactions in π-stacked DNA systems [245–248].

In vacuum, earlier MP2/6-31G* *ab initio* calculations predict that the most stable stacked pair of DNA nucleobases (considering only $G \ldots G$, $C \ldots C$, and $A \ldots A$ dimers) is the $G \ldots G$ dimer, while the least stable is the $C \ldots C$ dimer [249], a result which was obtained considering a 3.3–3.4 Å vertical separation between bases, which agrees with the 3.3–3.5 Å value observed in crystals of DNA constituents [250] and in high-resolved oligonucleotide crystals [251]. MP2/6-31G* calculations in the complete basis set limit (CBS) corrected by the coupled-cluster method (abbreviated as CBS(T)) have shown a different stability ordering for the same set of stacked dimers [252], with guanine being the most stable dimer and adenine the

less stable one (replacing cytosine). The orientational dependence of the stacking energy is dominated by twist and rise contributions [252,253].

DFT calculations for guanine dimers in a supercell revealed that dimers connected by hydrogen bonds have dispersionless bands, which are not good for electronic transport, while stacked dimers have dispersive bands originated from $\pi - \pi$ interactions (dispersive bands create channels for charge migration) [231]. Band transport may also be partially responsible for the charge mobility in nucleotide aggregates characterized by a large base–base superposition. This scheme is probably complemented by a hopping mechanism connecting spatially different regions where such base superposition occurs. The *ab initio* Hartree–Fock crystal orbital method with a basis of atomic orbitals was employed by Ladik et al. [232] to study the electronic structure of stackings made from the four DNA nucleobases. For the valence bands, thymine and guanine (adenine and cytosine) stackings exhibited the widest (narrowest) band widths, favoring (unfavoring) the band transport of holes. For the conduction bands the picture is somewhat different, with the band widths of guanine and cytosine (adenine and thymine) stackings being the largest (smallest), aiding (opposing) the band transport of electrons. The DFT estimated energy gap of stacked guanine nucleobases is 7.20 eV, larger than the gap of stacked adenine nucleobases (6.87 eV), but smaller than the gaps for cytosine and thymine (both equal to 7.41 eV) [232].

Sugar–phosphate chains, water structures and counterions contribute to enhance DNA structural stability, and promote the formation of energy levels inside the energy gap of stacked nucleobases which strongly affect DNA electronic, optical, and charge transport properties. DFT calculations within the generalized gradient approximation (GGA) for the exchange–correlation energy using the BLYP functional were performed for A-type DNA with 11 base pairs and B-type DNA with 10 base pairs [254], including base molecule, sugar, phosphoric acid, and sodium. The geometries of the A- and B-DNA crystals used in these computations were estimated through classical molecular mechanics/molecular dynamics. The electronic band structures of A-DNA showed valence (conduction) band widths of 0.081 (0.133) eV for the Poly(dG)–Poly(dC) configuration and 0.244 (0.360) eV for Poly(dA)–Poly(dT) [254]. In the case of B-type DNA with 10 base pairs, the widths of the valence (conduction) bands were estimated as 0.045 (0.120) and 0.421 (0.143) eV for Poly(dA)–Poly(dT) and Poly(dG)–Poly(dC) strands, respectively. The calculated energy gaps were 1.249 eV (*A* Poly(dA)–Poly(dT)), 0.824 eV (*A* Poly(dG)–Poly(dC)), 2.743 eV (*B* Poly(dA)–Poly(dT)), and 1.448 eV (*B* Poly(dG)–Poly(dC)) [254].

On the other hand, other first principles studies suggest that significant charge transport in van der Waals bonded layered guanine crystals is possible along the stacking direction [243] due to a dispersive band energy along the $\pi - \pi$ stacking axis with predicted valence band width of 0.83 eV and a direct band gap of 2.73 eV, much smaller than the 3.90 eV HOMO–LUMO energy gap of the gas-phase guanine molecule. Finally, spectroscopic ellipsometry measurements were performed using synchrotron radiation to obtain the dielectric functions of *G*, *A*, *C*, *T* films grown on hydrogen terminated Si(111) surfaces under ultra-high vacuum conditions. Guanine and adenine films exhibited strong optical anisotropy, with the ordinary ($\perp$ [111]) component of the dielectric function being larger compared to the extraordinary ($\parallel$ [111]) component, while cytosine and thymine dielectric functions were shown to be isotropic [244].

Although the crystal structures of anhydrous thymine [255,256] and cytosine [257,258] were determined several years ago, it is remarkable that the crystal structures of anhydrous guanine and adenine were not obtained until recently, due to the lack of good quality crystals [259]. In this section, using the published crystallographic data for the four anhydrous DNA nucleobase crystals (ACrs) guanine, adenine, cytosine and thymine, we carry out, using DFT computations, a comparative study of their structural, electronic, and optical properties, looking for the determination of the effective masses of electrons and holes along directions parallel and perpendicular to the π-stacking planes, as well as the nature of the energy band gaps (if they are direct or indirect) [260]. In fact, considering that the carrier effective masses could be very useful to model the carrier transport in DNA-based films and nanostructures, it is surprising to note the absence in the literature of any estimates on their values for crystals of DNA nucleobases. Experimental measurements of optical absorption for each ACr are also performed, allowing the estimation of their band gaps, and showing that they resemble wide gap semiconductors. Finally, the dielectric function of each crystal is obtained for different polarization planes of incident radiation, and compared with available experimental data.

8.1. Crystal structures

Anhydrous guanine crystals are monoclinic with space group $P2_1/c$ [261], four $C_5H_5N_5O$ molecules per unit cell, and molecular stacking along (1 0 2) planes. The anhydrous adenine crystals, on the other hand, are monoclinic with eight $C_5H_5N_5$ molecules per unit cell, space group $P2_1/c$ [259] and (1 0 −1) stacking planes. The anhydrous cytosine crystals are orthorhombic with four $C_4H_5N_3O$ formulae in each unit cell, space group $P2_12_12_1$ [257,258] and two intercalated stacking planes (2 0 1) and (−2 0 1), which are symmetrically equivalent. Finally, anhydrous thymine crystals have four $C_5H_6N_6O_2$ molecules in each unit cell, being monoclinic with space group $P2_1/c$ [255,256] and (−1 0 1) stacking planes. Guanine and adenine molecules appear twisted along the stacking direction, cytosine molecules are slided and the thymine molecules are slided and shifted, as shown both in Fig. 8.1 and, more clearly, in the top part of Fig. 8.4. The orientation of the stacked bases in these crystals has an important role on their physical properties.

Nucleobase powders (guanine 98% (G11950), adenine 99% (A8626), cytosine 99% (C3506), thymine 99% (T0376)) were purchased from sigma-Aldrich and used with no further purification. They are mixed with KBr to form six pellets for each nucleobase. Experimental measurements of the UV absorption spectra for the anhydrous crystals were carried out on these pellets using a Varian Cary 5000 UV–visible NIR spectrophotometer, equipped with solid sample holders. The absorption
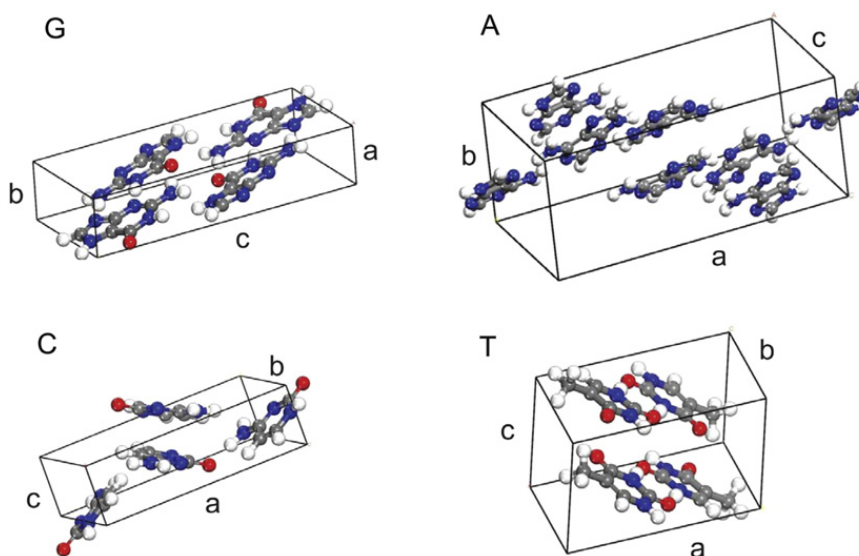
Fig. 8.1. (Color online) Unit cells of the *G* (guanine), *A* (adenine), *C* (cytosine), and *T* (thymine) anhydrous crystals.

spectrum of the samples was recorded in the 200–800 nm (50,000–12,500 cm^{-1}) wavelength range. The optical absorption measurements were accomplished by transmittance and the background removal was accomplished by comparison with the absorption spectrum of a KBr pellet. Baseline corrections were made when necessary.

8.2. Computational details

The computational simulations were performed using the CASTEP code [262,263], which is based on the DFT approach. The LDA exchange–correlation potential, developed by Ceperley and Alder [264] and parametrized by Perdew and Zunger [265], was adopted as well. With respect to our choice of functional, a note of caution must be made. The LDA approximation is not the best option to provide an accurate account of hydrogen bonds, the generalized gradient approximation (GGA) being preferable in this aspect. However, van der Waals interactions along the molecular stacking axis and hydrogen bonding between molecules in the same stacking plane are relevant to explain the structural features of anhydrous DNA bases crystals, and it is well known that pure DFT methods are unable to give a good description of dispersive forces. Even hybrid functionals, which predict improved band gaps in comparison with LDA and GGA approaches, do not significantly improve the electronic ground state. However, some DFT studies of crystals such as $CaCO_3$ [266], as well as guanine hydrated crystals [267,268] have shown that the local density approximation (LDA) gives reasonable values for atomic distances, notwithstanding the limitations of this functional. This and the relatively low cost of LDA computations have motivated us to adopt LDA instead of more sophisticated (and computationally expensive) means.

Vanderbilt ultrasoft pseudopotentials were used to describe the core electronic states of each atomic species [269], and the Kohn–Sham orbitals were evaluated using a plane wave basis set with a converged energy cutoff of 610 eV. Each unit cell was relaxed to attain a total energy minimum allowing for lattice parameter and atomic position adjustments. Convergence thresholds selected for all geometry optimizations were: total energy variation smaller than 0.10×10^{-4} eV/atom, maximum force per atom smaller than 0.03 eV/Å, maximum displacement smaller than 0.001 Å, and maximum stress component smaller than 0.05 GPa. A two steps convergence tolerance window was employed, and the optimization method used was the BFGS minimizer [270]. The basis set quality was kept fixed throughout unit cell volume changes. The self-consistent field steps have taken into account tolerances of 0.1×10^{-5} eV/atom for total energy and 0.4979×10^{-6} eV for the electronic Eigen-energies. From the valence band (VB) and conduction band (CB) curves at their critical points (maxima for VB and minima for CB) we have estimated the effective masses for electrons and holes for the anhydrous DNA bases crystals as follows: we take a band curve starting at some extremum in reciprocal space along a $\vec{k}$ direction of interest, and perform a parabolic fitting of this curve, which allows the determination of the corresponding effective mass through the relation $E(\vec{k}) = \hbar^2 k^2 / 2m$. For the band structure computations, paths formed from a set of high symmetry points in the first Brillouin zone were chosen, as shown in Fig. 8.2. However, we present here only the band structures near the valence band maxima.

8.3. Geometry optimization

From the LDA-DFT calculations, we have obtained the following formation energies for the anhydrous DNA base crystals: −60.5 kcal/mol for guanine, −42.8 kcal/mol for adenine, −47.6 kcal/mol for cytosine and −39.4 kcal/mol for thymine, which suggests that the stability of these crystals obeys the sequence $G > C > A > T$. This must be put in contrast with the result of Šponer et al. [249,252] for guanine, adenine, cytosine and uracil stacked dimers, which predicts a $G \ldots G$ dimer as the most

Table 2

Calculated a, b, c lattice parameters, β angle, unit cell volume V, and distance d between successive stacked molecular planes for the guanine, adenine, cytosine, and thymine anhydrous crystals. Experimental values are indicated between parentheses and were obtained from: guanine, Ref. [261]; adenine, Ref. [259]; cytosine, Refs. [257,258]; and thymine, Refs. [255,256].

	a (Å)	b (Å)	c (Å)	β (°)	V (Å^3)	d (Å)
G	3.45 (3.55)	9.46 (9.69)	16.03 (16.35)	96.23 (95.75)	519.01 (560.08)	2.53 (2.59)
A	7.66 (7.89)	21.52 (22.24)	6.97 (7.45)	112.44 (113.19)	1057.86 (1201.57)	2.99 (3.19)
C	12.60 (13.04)	9.24 (9.50)	3.60 (3.81)	-	419.01 (472.42)	3.21 (3.43)
T	10.70 (12.87)	6.71 (6.83)	6.87 (6.70)	97.00 (105.00)	489.88 (568.88)	2.99 (3.19)
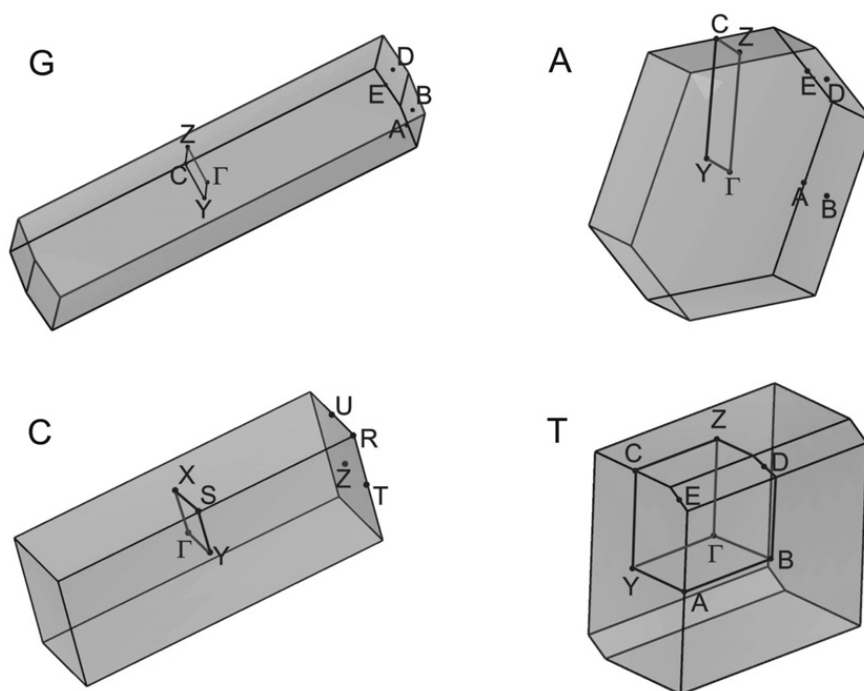
**Fig. 8.2.** First Brillouin zones of *G* (guanine), *A* (adenine), *C* (cytosine), and *T* (thymine) crystals. High-symmetry points are shown.

stable stacked DNA base pair in vacuum. Moreover, stacked cytosine dimers have larger binding energy in comparison with stacked adenine dimers [252], while our results point out that anhydrous cytosine crystals rank in second place of stability in comparison with the other crystals of DNA nucleobases (Refs. [249,252] have not dealt with thymine).

In order to check if the distinct boundary conditions of nucleobase dimers in comparison with the crystalline phase affect the results, we have carried out LDA calculations for the same dimers studied by Šponer et al. [249,252], using a 20 Å × 20 Å × 20 Å cubic supercell and the same basis set/convergence thresholds of the crystal simulations. The obtained LDA binding energies of the dimers were −10.8 kcal/mol ($G \ldots G$), −7.0 kcal/mol ($A \ldots A$), and −8.68 kcal/mol (A), which are close to the values obtained using the more accurate CBS(T) approach: −12.7 kcal/mol ($G \ldots G$), −8.5 kcal/mol ($A \ldots A$), and −10 kcal/mol ($C \ldots C$). Notwithstanding the limitations of the LDA method, its data reproduces the same ordering of dimer stabilities from the CBS(T) calculations: $G \ldots G > C \ldots C > A \ldots A$. A direct comparison with experiment, on the other hand, is very difficult as experimental errors can be originated from a series of factors, namely: limited resolution, averaged samples, poor refinement, averaged geometries, sensitivity of hydrogen bonds, etc. However, the values reported using the CBS(T) method, as it is discussed in [252], seem to be in fair agreement with the experimental data, and the LDA values obtained here are close to the CBS(T) values. One must consider, however, that even for high level methods the calculated energies may be highly sensitive to details of the method, as the CBS(T) results disagree with previous CBS simulations [252], so the proximity of the theoretical values to experimental data could be only coincidental. So we hope that our data will reproduce qualitative trends at least when compared with experiment.

The calculated lattice parameters of the ACrs are shown in Table 2 together with the experimental data. In order to perform an analysis of these results, we define here the relative difference between theory (LDA) and experiment (Exp) for a given parameter X, i.e., Δ(LDA–Exp) $= 100 \times (X \, \text{LDA} - X\text{Exp})/(X \, \text{Exp})$. It is usual for LDA computations to predict lattice parameters smaller (in comparison with Exp) by about 5% for organic crystals [271]. The figures presented here follow this trend. As a matter of fact, the guanine crystal has the smaller values for Δ(LDA–Exp), with LDA lattice parameters being at worst 2.9% smaller (for the a length) than the measured value. In the case of adenine, Δ(LDA–Exp) is more pronounced for the c length, which has a computed value Δ(LDA–Exp) of approximately −6.5%. For cytosine, the most pronounced difference between LDA and experiment is approximately −5.5% along c, while thymine presents the worst figures, with Δ(LDA–Exp)
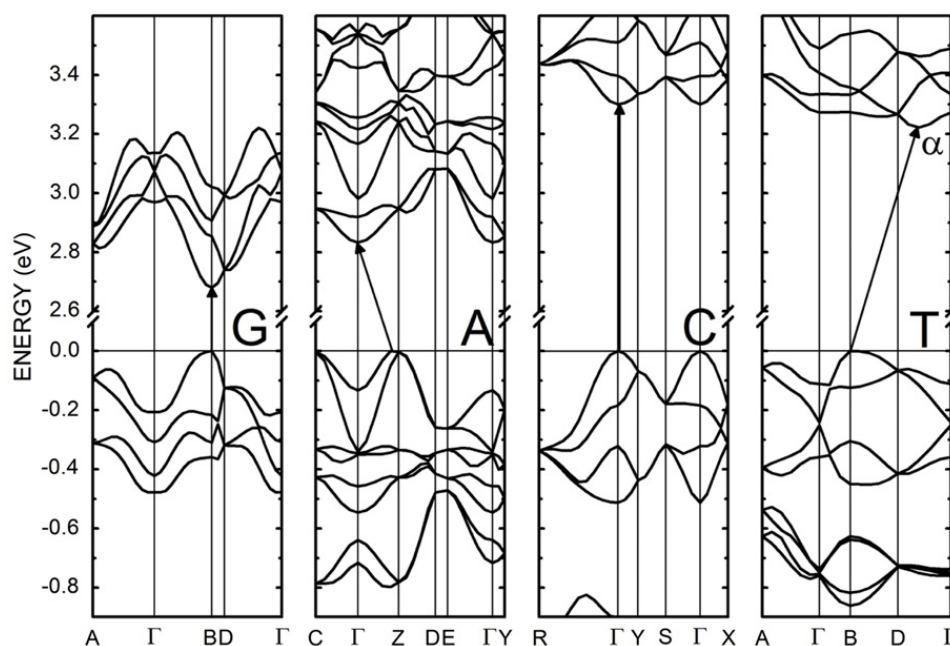
Fig. 8.3. Close-up of the electronic band structures of *G* (guanine), *A* (adenine), *C* (cytosine), and *T* (thymine) anhydrous crystals near their main band gaps. Direct and indirect transitions are indicated by the arrows.

of −16.9% for the *a* parameter (a result due to the LDA overestimation of the interaction energy between thymine molecules along a direction where van der Waals forces are dominant). Also for thymine, one observe that the *c* parameter predicted by the LDA computations is about 2.5% larger than the experimental value, in contrast with the typical overbind trend observed for this exchange–correlation functional.

The β angle for guanine, adenine and thymine (cytosine is orthorhombic) exhibits Δ(LDA–Exp) variations of 0.5%, −0.7%, and −7.6%, respectively (again, the worst figures are for thymine), while the unit cell volume *V* has Δ(LDA–Exp) of −7.3% for guanine, −12% for adenine, −11% for cytosine and −14% for thymine. The distance between stacking planes *d* for each crystal has Δ(LDA–Exp) of −2.3% for guanine, −6.3% for adenine and thymine (both have practically the same value of *d*), and −6.4% for cytosine. The calculated *d* values are in general smaller than the 3.29–3.30 Å interplanar spacing between stacked *G*, *A*, *C*, *T* dimers of <100 nm thick films grown on hydrogen terminated Si(111) surfaces under ultra-high vacuum conditions [244], and the 3.15 Å in LDA and 3.64 Å in GGA calculated intermolecular plane spacings of monohydrated guanine crystals, whose experimental value is 3.30 Å [272]. Furthermore, they are practically in the range defined by the average interplanar distance of 2.56 Å and 3.38 Å in A- and B-type DNA, respectively [254]. Thus, the role of interplanar base coupling in anhydrous crystals of DNA bases on their physical properties is as relevant as in the case of stacked DNA bases, non-relaxed thick nanofilms of DNA bases, and *A,B*-DNA strands.

8.4. Electronic band structures

Fig. 8.3 shows a close-up of the band structures for the ACrs at the main gap regions. Guanine and cytosine have direct band gaps, a $B \rightarrow B$ transition for the guanine crystal, and a $\Gamma \rightarrow \Gamma$ transition for cytosine. Adenine has its main band gap from a maximum at the valence band (very near to the *Z* point), to its conduction band minimum at the Γ point (not shown in Fig. 8.3), while thymine has its valence band maximum at the *B* point and conduction band minimum in a point in reciprocal space situated along the Γ–*D* direction (denoted here using the Greek letter α), both crystals being indirect band gap materials. The main contributions for the uppermost valence bands for guanine, adenine and cytosine originate from *N* 2p orbitals, while for thymine the electronic states at the top of the valence band are formed mainly from *C* 2p states. All nucleobases have the bottom of the conduction band formed mainly from *C* 2p states, with small contributions from *H* 1s orbitals.

Table 3 presents the LDA band gaps for the nucleobase crystals, together with the results of three sets of experimental results. It is necessary to remember that, as Kohn–Sham eigenvalues do not give correct excitation energies [273,274], DFT exchange–correlation functionals predict band gaps quite different from experimental values. The LDA exchange–correlation functional tends to underestimate the main gap of semiconductors and insulators by about 40%. However, some works suggest that a rigid shift in the LDA conduction bands is just enough to provide a reasonable agreement with more sophisticated approximations [273,275–277]. For this reason we believe that, despite the lack of accuracy of our band gap estimates, the shape of the uppermost valence band and lowermost conduction band curves (and the effective masses calculated from them) are meaningful. The ACrs ordered by increasing band gap, according with the LDA calculations, are $G < A < T < C$, ranging from 2.68 eV (guanine) to 3.30 eV (cytosine).

Table 3
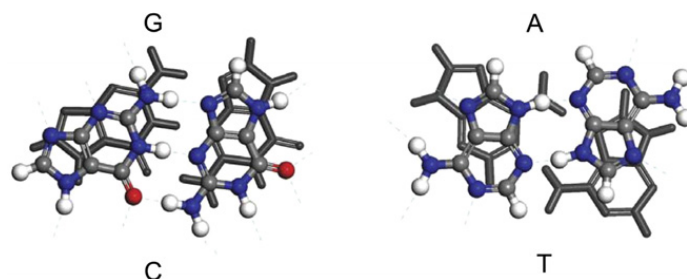Anhydrous crystals of DNA nucleobases: LDA and experimental energy gaps E_g with corresponding valence band → conduction band transition assigned. In the experimental section, I (D) stands for indirect (direct) gap. Effective masses of electrons and holes along directions parallel and perpendicular to the stacking planes (in units of the free electron mass m_0) are also shown.

|	E_g (LDA, eV)	E_g (Exp, eV)	m_e ∥	m_e ⊥	m_h ∥	m_h ⊥
G	2.68 ($B \to B$)	3.82–3.84[a] 2.6[b] 4.3–4.6[c]	11.5	4.0	9.2	4.0
A	2.83 ($\approx Z \to \Gamma$)	3.85–3.92[a] 4.7[b] 4.5–4.6[c]	>40	5.4	>40	3.8
C	3.30 ($\Gamma \to \Gamma$)	3.82–3.86[a] 3.6[b] 4.4–4.7[c]	>20	5.8	12	3.5
T	3.22 ($B \to \alpha$)	4.04–4.09[a] 5.2[b] 4.5–4.8[c]	3.8	6.3	6.9	15

[a] This work.
[b] Ref. [278].
[c] Ref. [244].

Fig. 8.4. (Color online) Top: Viewing stacked layers in the anhydrous crystals of DNA nucleobases: *G* (guanine), *A* (adenine), *C* (cytosine), and *T* (thymine). Middle: close-up of the *G*, *A*, *C*, and *T* band structures at the corresponding valence band maxima along directions parallel and perpendicular to the stacking planes. Bottom: *G*, *A*, *C*, and *T* valence (ΔV) and conduction (ΔC) bandwidths. In gray (black), bandwidths along the parallel (perpendicular) direction. The top two bars indicate ΔV and the two bottom bars indicate ΔC.

X-ray absorption and soft X-ray emission spectroscopy of the DNA nucleobases powders were performed by Mac-Naughton et al. [278], being obtained a HOMO–LUMO energy gap of 2.6 eV for guanine, 3.6 eV for cytosine, 4.7 eV for adenine, and 5.2 eV for thymine, leading to a $G < C < A < T$ ordering of increasing band gaps for the ACrs, which agrees with the LDA calculations only for the lowest gap guanine crystals. On the other hand, a survey of experimental measurements performed by Silaghi et al. [244] for DNA nucleobase films points to an energy gap of guanine in the 4.31–4.59 eV range, cytosine in the 4.40–4.70 eV range, adenine in the 4.45–4.63 eV range, and thymine in the 4.5–4.8 eV range. As these energy ranges are overlapped, it is not possible to present a list of crystals ordered by band gaps. Moreover, the electronic structure of these thin films (80–120 nm) must be affected by surface effects absent in bulk crystals.

Tight-binding transport models depend on the interaction of adjacent orbitals and the resulting band dispersion. In this approach, the description of band transport along DNA nucleobase stackings must take into account the bandwidth of the valence and conduction bands near the respective band extremes. Fig. 8.4 presents, at its bottom part, the valence (ΔV) and conduction (ΔC) bandwidths, calculated for the uppermost and lowermost overlapping valence and conduction bands, respectively. Nevertheless, an adequate description of the charge transport, even for organic crystals, can be also given through the effective mass approximation [279]. Indeed, there is a relationship between effective mass (m) and bandwidth (ΔE): the larger the first, smaller the latter (the effective mass is inversely proportional to band curvature and, therefore, to band dispersion).

The top part of Fig. 8.4 shows some views of the molecular layers in each ACr. Its middle part display another set of close-ups of the ACrs electronic band structures near their valence band extremes for two selected directions in reciprocal space: parallel (∥) and perpendicular (⊥) to the plane define by a nucleobase in an unit cell. The parallel directions were selected to be along some specific hydrogen bonds in order to give some information on the transport of charge carriers across them. These directions are shown in Fig. 8.5: N7-H...O6 for guanine (atomic numbering of [261]), N9-H...N3 for adenine (atomic numbering of [259]), N4-H4...O2 for cytosine (atomic numbering of [257]), and N3-H...O1 for thymine (atomic numbering of [256]). These directions were used to estimate effective masses for both electrons and holes. Starting from the conduction band minimum along a direction parallel to the plan of each nucleobase, we have calculated the smallest electron effective
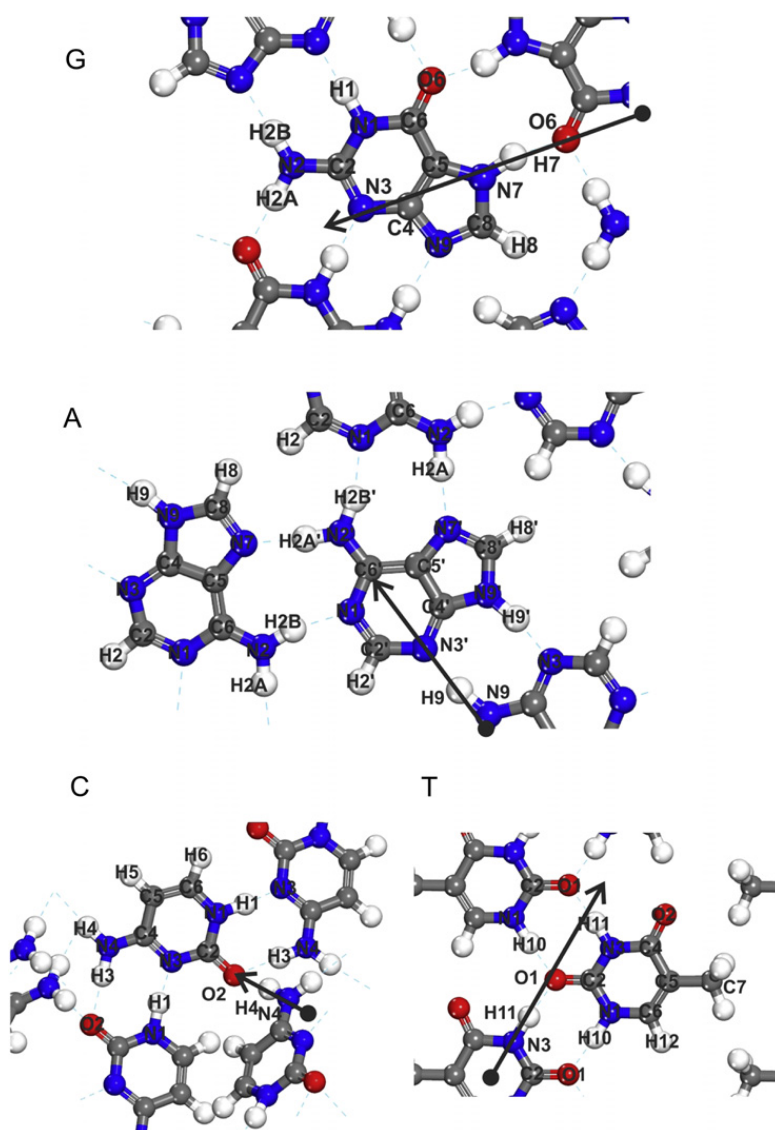
Fig. 8.5. (Color online) "Parallel" directions along with the carrier effective masses were calculated in this work. They were chosen to be aligned with selected hydrogen bonds.

mass for thymine (3.8 m_0, where m_0 is the free electron mass) and the largest for adenine ($>40\ m_0$). All in all, it seems that the hopping of electrons along hydrogen bonds is very small for anhydrous crystals of guanine, adenine and cytosine. In the perpendicular direction (along the π-stacking axis), however, all nucleobase crystals exhibit electron effective masses in the 4.0–6.3 m_0 range, signaling the possibility of semiconducting electronic transport in stacked nucleobases (for comparison, doped SrTiO$_3$ can achieve electronic effective masses as high as 7.7 m_0 [280]). Hole transport along the parallel direction involves very large effective masses for guanine, adenine and cytosine, while thymine has the smallest hole mass for hopping across hydrogen bonds, 6.9 m_0. For the perpendicular effective mass, this situation is reversed, with guanine, adenine and cytosine exhibiting hole effective masses in the 3.5–4.0 m_0 range, while thymine has a 15 m_0 effective mass. In general, one can presume from the results here presented that stacked nucleobases in anhydrous crystals (and possibly for linear chains) behave like wide gap semiconductors for electrons moving along the stacking direction, while the hole transport is somewhat limited in stackings involving thymine nucleobases.

Finally, it is possible to object that the use of static structures of anhydrous crystals to obtain the electronic band structures is inadequate, as it does not take into account thermal effects which are relevant, for example, for DNA strands. Indeed, it was shown that DNA strands have electronic properties highly sensitive to DNA conformation and temperature [281]. It is more difficult, however, to include thermal effects directly into DFT calculations. Inelastic effects caused by electron–phonon coupling cannot be computed, as DFT decouples the movements of electrons and atomic nuclei following the Born–Oppenheimer approximation. Nuclear configuration effects, on the other hand, can be estimated through the sampling and averaging of an appropriate set of conformations of the studied structure, and have a more relevant role on the electronic properties of DNA base crystals. In order to make a grounded guess of the vibrational effects on the electronic structure, we have performed DFT simulations on disturbed crystals, with atomic positions randomly changed along arbitrary directions by 0.3 Å in average. This displacement was chosen taking as reference published data for colossal thermal

expansion behavior of $Ag_3[Co(CN)_6]$ crystals, which exhibit a lattice parameter variation of about 0.3 Å in the temperature range 20–500 K [282]. In comparison, thermal nuclear motions in 10–15 base pair molecules at room temperature are larger by about one order of magnitude. For all sets of crystals investigated, we noted that the shape of the valence and conduction band curves do not change significantly, at least not to the point of invalidating our conclusions on the semiconducting character of the ACrs for low temperatures, as all effective masses smaller than 7 m_0 of Table 3 vary by less than 1.2 m_0. One can contrast our results with those of Ortmann et al. [243], who investigated the charge transport in anhydrous guanine crystals using the Kubo formalism obtaining the mobility of holes using data from DFT calculations. They have shown that the polaron concept is required to understand the temperature dependence of the hole transport in guanine systems, the hole transport at room temperature having a small contribution from coherent transport and being very anisotropic. For temperatures below about 70 K, the effective mass of hole polarons in guanine anhydrous crystals is practically constant and about 1.5 times larger than the bare hole effective mass. Beyond this limit, the hole polaron mass increases almost linearly with temperature, reaching about 10 times the bare hole mass at 300 K. In another more recent work, the same authors have endorsed the use of DFT-LDA simulations to parametrize the charge transport in organic crystals for more sophisticated methods of approximation including temperature [283]. On the other hand, the band dispersion in highly ordered hydrated multilayer films of guanine was measured recently using photoelectron spectroscopy [284], the results showing a small hole effective mass of about 1.1 m_0, suggesting the existence of band-like charge transport even at room temperature. All in all, we believe that the effective masses we obtained are useful in the description of the low temperature charge transport (below 70 K, if we follow Ref. [283]) in anhydrous DNA nucleobase crystals. Finally, besides thermal effects we could mention boundary effects, crystal defects, impurities, etc., which can also affect the electronic properties of the crystals and are not addressed here.

8.5. Optical properties

The averaged experimental absorption spectra of the anhydrous nucleobase crystal powders are shown in Fig. 8.6. For each nucleobase, six samples were prepared and the average spectrum was obtained, together with the standard deviations at selected photon energies, which were used to draw the error bars. It is easy to perceive that all ACrs present two broad maxima in the energy range between about 4 and 6 eV, with the cytosine crystal exhibiting a small hump below 4 eV. As one can see, the error bars are small in general, being significant only for energies larger than 6 eV, well above the onset of optical absorption. In order to estimate the energy gaps from absorption experiments, one must perform a linear fitting of the square (square root) of the absorption coefficient near the absorption onset for direct (indirect) band gap materials [285]. Here we used the indications given by the LDA calculations, considering that guanine and cytosine have direct band gap, while adenine and thymine have indirect band gaps. The values estimated from this interpolation (shown in Table 3) comprise different, but in general small, energy ranges when one looks to the set of samples used in the measurements: 3.82–3.84 eV for guanine, 3.85–3.92 eV for adenine, 3.82–3.86 eV for cytosine, and 4.04–4.09 eV for thymine (the difference between the maximum and minimum gap for each energy range is smaller than 0.1 eV). So, the sequence of increasing gaps is $G \approx C < A < T$. Comparing this result with the order of gaps predicted by LDA computations, $G < A < T < C$, we see that both data predict guanine with smallest band gap and adenine having a gap smaller than thymine, but the largest LDA band gap occurs for cytosine instead of thymine. However, taking into account the limited description of band gaps using pure DFT functionals, these differences were not surprising (one must note also that the found LDA gaps are always smaller than the optical absorption estimates by 0.5–1 eV). Observe that the gap value found in [278] for guanine is slightly smaller than the LDA prediction, and much smaller than the values found from optical absorption and the energy range proposed here and in [244]. Contrasting the experimental ordering of gaps $G < A < C < T$ obtained in [278] with ours, we see a good agreement, except that the average band gap of guanine from our absorption measurements is slightly smaller than adenine (the difference being only 10 meV), which does not allow us to affirm conclusively that guanine has the smallest band gap. The band gap of cytosine predicted here (average 3.84 eV) is not far from the 3.6 eV value found in [278], although the other values are very different, reaching a difference of 1.1 eV between the gaps for thymine and 1.2 eV for guanine. We believe that these differences are due to the difficulties inherent to the X-ray absorption–emission spectroscopy method employed in [278].

Fig. 8.7 depicts the complex dielectric function for the ACrs for incident light with distinct polarizations, the real part (η_1) being calculated from the imaginary part (η_2) via the Kramers–Kronig relationship [286]. The work of Lebègue et al. [287] suggests that LDA dielectric functions, in comparison with more sophisticated methods, differ mainly by a scaling factor plus some energy shift. This can be checked out from our calculated curves, which after some scaling and energy shifting, compare reasonably well with the experimental data of [244]. For guanine, there is a very pronounced anisotropy for both η_1 and η_2 along the polarization planes (010) (parallel to the plane of a guanine molecule), ($10\bar{2}$) (perpendicular), and ($1\bar{2}8$) (which contains the N7-H...O6 hydrogen bond). For adenine, the dielectric function components for light polarized along the parallel (010) and perpendicular ($10\bar{1}$) molecular planes are very anisotropic as well, with the perpendicular components exhibiting very small variation as the energy increases, which is odd, as the expected result should be a dominance of the perpendicular polarization in the optical absorption due to the transfer of electrons between neighbor π molecular orbitals. This result is probably due to the inability of the DFT-LDA functional to describe π stacking interactions. The cytosine crystal dielectric function components, on the other hand, are practically the same for light polarized along the parallel (911), containing the N4-H4...O2 hydrogen bond, and perpendicular ($20\bar{1}$) molecular planes. Finally, the thymine crystals show a pronounced anisotropy for the dielectric function components when one compares the cases where the incident light is
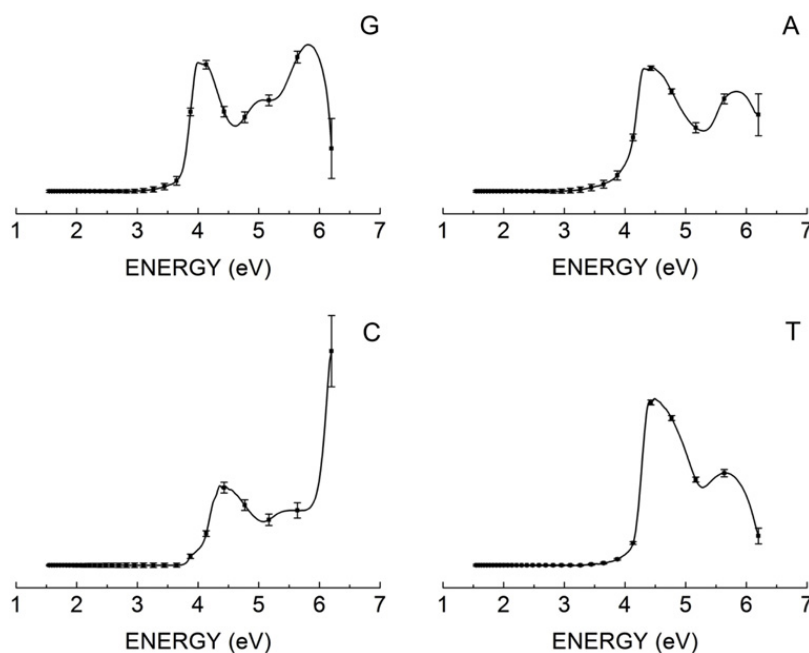
Fig. 8.6. Measured optical absorption spectra of the nucleobase anhydrous crystals (in arbitrary units): *G* (guanine), *A* (adenine), *C* (cytosine), and *T* (thymine). Error bars are shown for the six samples used in the experiment. Each curve is formed from 600 experimental data points.
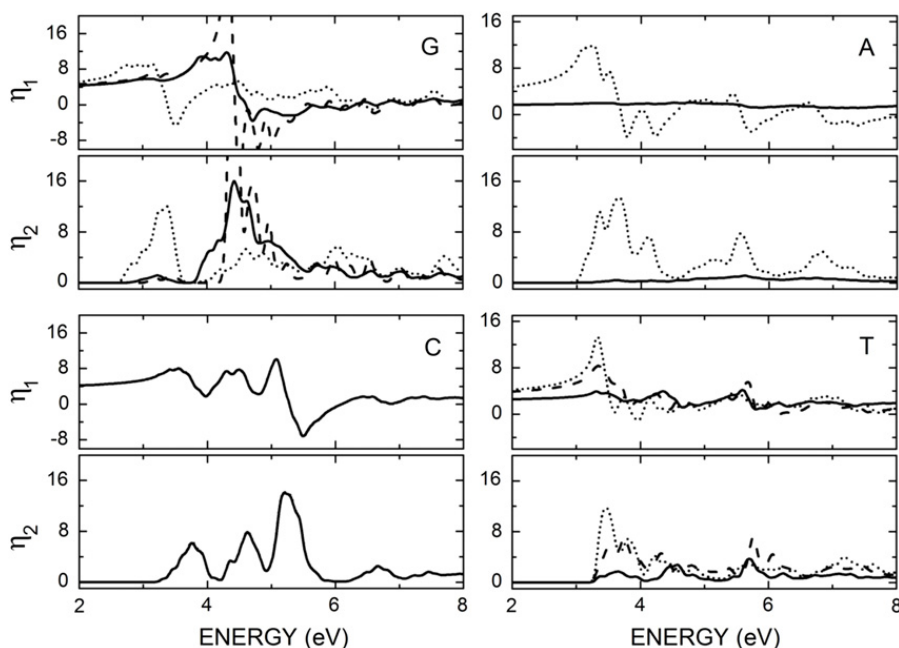
Fig. 8.7. Complex dielectric function, $\eta = \eta_1 + i\eta_2$, of the anhydrous crystals of DNA bases. Solid lines: incident light with polarization plane perpendicular to the molecular plane of a single nucleobase in each ACr unit cell; dotted lines: incident light with polarization plane parallel to the nucleobase plane. Dashed lines correspond to light polarization along the $12\bar{8}$ plane for guanine (which contains the N7-H...O6 hydrogen bond) and along the $5\bar{5}2$ plane for thymine (containing the N3-H...O1 hydrogen bond).

polarized parallel (010) and perpendicular ($10\bar{1}$) to the molecular plane, and parallel to the ($5\bar{5}2$) plane, which contains the N3-H...O1 hydrogen bond. The anisotropy of the optical properties of guanine, thymine and adenine (specially the latter) can be useful for applications in the field of nonlinear optics, for example.

In summary, in this section we have performed DFT calculations to obtain optimized geometries for the anhydrous crystals of the four DNA nucleobases, guanine (*G*), adenine (*A*), cytosine (*C*) and thymine (*T*) using the local density approximation (LDA) for the exchange–correlation functional, and have estimated the band gaps of these crystals from optical absorption measurements. The LDA optimized crystals have lattice parameters smaller than the experimental values, with the smallest (*b* parameter, −1.7%) and largest (*a* parameter, ≈−17%, resulting from the LDA overestimation of the interaction along a direction where van der Waals forces are prevalent) differences observed for the thymine crystal. The distance between molecular planes *d* is 2.3% smaller than experiment for guanine, and 6.4% smaller for cytosine. The

difference between experimental data and the optimized unit cell volumes increases in the order $G < C < A < T$. This same ordering is followed by the formation energies of the crystals, suggesting that guanine is the most stable structure, while thymine is the less stable one. Analysis of the electronic band structures of the ACrs revealed that guanine and cytosine are direct band gap materials, while adenine and thymine have indirect band gaps. LDA values for the energy gaps are smaller than the experimental values, as expected, and the gaps estimated from the optical absorption measurements presented in this work are in general smaller than the experimental data available in the literature (except for guanine). The LDA ordering of increasing band gaps is $G < A < C < T$, while the ordering obtained from the optical absorption measurements is $G \approx C < A < T$. Band dispersions, which are crucial to model the electronic transport properties using the tight-binding model, are related with the effective masses, which were also calculated here. For electrons and holes moving along selected hydrogen bonds (parallel to the molecular plane of a given nucleobase), effective masses are in general large, exception made to thymine. When the same electrons move along the π-stacking axis, however, effective masses stay in the 4.0–6.3 m_0 range, which suggests that stackings of nucleobases at low temperature behave like wide band gap semiconductors for electrons. The transport of holes is also favored for nucleobase stackings without thymine. Finally, the complex dielectric function was calculated for each ACr, and a very pronounced anisotropy was observed for polarized incident light in the cases of guanine, thymine and for adenine (specially), but not for cytosine.

9. Prospecting future trends and concluding remarks

To conclude, we present in this section a survey of some relevant findings discussed in the recent literature, reporting on either novel designs or new conceptual DNA's approaches that will likely deserve closer attention in the years to come. Major challenges to be overcome in order to improve the theoretical modeling of DNA electronic properties will also be discussed.

9.1. Applications of DNA charge transport in nanobiotechnology and molecular electronics

DNA-binding proteins involved in genome maintenance can be linked to long-range signaling across the genome, which raises the possibility of charge transport processes being used not only to activate the genome to respond to stress, but also to protect it through signaling among proteins [288]. Effective tight-binding models were applied to study theoretically the effects of point mutations on charge transfer properties in the DNA sequence of the tumor-suppressor p53 gene [109]. It was shown that, in contrast with noncancerous mutations, cancer related mutations produce significantly weaker changes of transmission properties, which indicates that charge transport can affect the DNA-repairing capabilities and induce carcinogenesis. These results, however, must be further investigated because the electron–phonon coupling and the long-range interactions effect were not taken into account. By the way, it has been also demonstrated a contractile DNA nanoswitch which can be turned on (contracted) and off (extended) with a 40-fold conductivity difference between the two states [289]. The nanoswitch can be activated repeatedly, being suitable to develop prototypes for more sophisticated and complex electronic DNA-based electronic nanodevices, such as DNA transistors, if one can figure out how to electronically gate the nanoswitches. Contractile duplexes could also function as sensitive, chip-based electronic biosensors for the identification of quadruplex-interactive compounds to inhibit the enzyme telomerase and repress some oncogenes. Medicinal use of DNA and carbon nanotubes (CNTs) for an efficient and nontoxic transport through the cell membranes was also investigated, as carbon nanotubes have large surface areas, unique surface properties and needle-like shapes, allowing for the delivery of large amounts of therapeutical agents for gene therapy and imaging [290]. However, *in vivo* studies involving the use of carbon nanotubes for gene delivery are just beginning, being necessary to investigate systematically the stability, blood circulation and pharmacokinetics of DNA–CNT conjugates and complexes. The fabrication of nanodevices using a single-walled carbon nanotube (SWCNT) passing through a barrier between two fluid reservoirs has allowed the translocation of small single-stranded DNA oligomers through the SWCNT [291], opening new avenues for control of DNA translocation.

When a DNA electron is removed from DNA, a hole, mostly located at the nucleobases, migrates reversibly through duplex DNA via a hopping mechanism for long distances until it is trapped in an irreversible chemical reaction (typically at guanine sites) which damages the nucleobases and can lead to mutagenesis, carcinogenesis and aging. The efficiency of hopping depends on the particular sequence of nucleobases and the nature of the damaging chemical reaction. Counterions to the phosphate groups have an important role in helping the hopping mechanism and the eventual reaction with water molecules. A complete description of DNA oxidation demands more studies on the structural, kinetic and dynamic properties of DNA [292]. Damaged bases in DNA can be identified using DNA charge transport, based on a reduction in the number of sites to search by a localization of protein in the vicinity of lesions [293]. Analysis of 162 disease-related genes from several medical databases, with a total of almost 20,000 pathogenic mutations, revealed a significant difference in the electronic properties of the population of observed mutations in comparison with the set of all possible mutations [294], implying that the electronic properties of DNA have an important role in cellular processes, and leading to the possibility of using them to predict, detect, and diagnose mutation sites. Experiments and theoretical simulations have demonstrated that the critical first step in the oxidative mutation of adenine–thymine rich DNA regions, which are involved in the genomic instability during the early stages of cancer development, is proton-coupled electron transfer occurring in thymine nucleobases [295].

Incorporating metals into DNA can result in new types of materials which could take advantage of the DNA programmability and nanoscale rigidity. Metal ions can be added to natural DNA, full metal complexes can be incorporated into DNA

strands, or metallated DNA can be formed after the placement of free ligands in the nucleic acid [296]. One can imagine, for example, metal complexes with distinct geometries being used to build branching DNA junctions with distinct spatial configurations that would be very difficult to achieve otherwise [297]. Metal complexes can also modulate the stability of DNA, affecting its robustness for use in nanomaterials [298]. The electronic, optical and photochemical properties of DNA doped with metals can be relevant for materials science and biotechnology as well, and DNA can work as a scaffold to create asymmetric structures with diverse transition metals being placed at specific sites, giving rise to 2D and 3D patterns [299]. Reversible and switchable DNA assemblies allow for the manipulation of metal–metal distances in a nanoscale structure, to produce detection assays and catalysis [300]. Some issues, however, must be addressed, such as the development of robust devices to measure directly charge transport or magnetic interactions in metal–DNA structures, and the incorporation of multiple different metals. With respect to the first difficulty, a quantitative measurement of the charge transfer which occurs when an organic molecule was excited by light was recently achieved by Fleisher et al. [301], and their technique could be adapted for the characterization of charge transport in pure and metal doped DNA chains. Energy gap characterization of single double-stranded DNA molecules complexed with metal ions [302] showed that the gaps in the I–V characteristics are associated with the molecular HOMO–LUMO gap, while the difference between the gaps for systems with and without the ions is actually due to the metal ion, which couple the energy levels of the DNA bases, and not to thermal or single electron tunneling effects. A recent work [303] has shown that excitation can be coupled from the localized surface plasmon polaritons resonance modes of a silver nanoparticle excited through multiphoton absorption by a femtosecond laser pulse to an attached DNA nanowire. The excitation can be transferred along the nanowire through several micrometers and from a nanoparticle to another through the DNA nanowire, combining the advantages of both molecular assemblies and plasmonics to establish a link between nanostructures, providing a communication channel between molecular devices.

Silicon chips with DNA modified electrodes (DMEs) employing DNA-mediated charge transport for multiplexed detection of DNA and DNA-binding protein targets were demonstrated by Slinker et al. [304]. Four DNA sequences were differentiated at the same time on a single DME chip, including one with a single base mismatch, emphasizing the high selectivity of these detectors. Protein activity from the restriction enzyme Alu1 was also investigated, with the chip exhibiting sequence-specific recognition. Other researchers have employed a tetrahedral DNA nanostructure to study charge transport through-space and through-duplex of small redox molecules bound to specific positions above the surface of a gold electrode [305]. The charge transport measurements shed new light on DNA-based molecular electronics and on the design of high-performance biosensor devices, suggesting that DNA nanostructures can be used for the rational design of switchable DNA nanodevices for electronic, biosensor, and computational applications. Functionalization of DNA with surfactants allows the production of good optical quality thin films from waste produced in food processing industries, with applications in electronics and photonics, obtaining more efficient materials with higher chromophore concentration for organic light emitting diodes (OLEDS) [306]. Electrical conductivity of DNA thin films can be tailored by doping and doped DNA can be transformed into a solid electrolyte which could be used in smart windows, solar energy conversion and batteries. Pheeney et al. [307] have shown that hemoglobin can be a robust and effective electron sink for electrocatalysis in DNA sensing on low-density DNA films, enhancing its sensitivity to the point of being able to perform femtomole DNA sampling.

Negative differential resistance (NDR) is a theme of interest for the development of molecular electronics due to potential applications in the development of logic devices and memory circuits. The charge transport through suspended DNA junctions was investigated by using the mechanically controllable break junction technique [308], with the current–voltage (I–V) characteristics in an aqueous solution revealing NDR and hysteresis. When the measurements were carried out in a high-vacuum environment, the peak positions of NDR were shifted to lower voltage with a sharp amplitude decrease. It is worth to note as well that simulations on the charge transfer between DNA and proteins in nucleosomes were carried out using combined solid state physical and chemical methods for a polythymidine–poly(lysine–triglycine) and a polythymidine–poly(arginine–triglycine) idealized system, revealing that the gap between the valence band of the polythymidine chain and the conduction bands of the model protein chains are very large to allow for a direct charge transfer between them [309]. It was also shown that electron excess can move through RNA π-stacks over a significant distance with dual distance dependence, which could be useful to design fluorescent RNA probes and RNA-based devices [310].

9.2. Water and counterion effects on DNA charge transport

Experiments on DNA bundles manipulated with silicon-based actuated tweezers have shown that the electrical conduction in DNA is ruled mainly by humidity [311]. Adsorption of water on the DNA backbone explains the quasi-Ohmic behavior and exponential dependence of conductivity with relative humidity observed in DNA strands. *Ab initio* density functional theory and classical molecular dynamics studies were employed to analyze the electrical structure and transmission probability in four DNA sequences taking into account water and counterion interactions [312], being shown that their conductance is primarily ruled by interstrand and interstrand coupling between low-energy guanine orbitals. When adenine–thymine base pairs were inserted between the guanine–cytosine rich domains, the first acted as a tunneling barrier. A hybrid method combining classical molecular dynamics, quantum chemical calculations and a tight-binding Hamiltonian, taking into account the time fluctuating electronic structure along a molecular dynamics trajectory with solvent effects, was also used to describe charge transport through DNA [313]. It supports the view that charge transport across solvated DNA wires is dominated by conformational fluctuations, implying that transport approaches based on band-like coherent transport or on static geometries, cannot give a good description of charge motion in these systems.

The conductance of DNA duplexes in a water-Na$^+$ solution for deformations along DNA acoustic modes was investigated using classical molecular dynamics and the Kubo technique [314]. Each lowest-frequency acoustic mode influence the DNA charge transmission in a quite different way, with the mode capable of enhancing the DNA duplex transmission being determined by the length and base sequence of the biopolymers, while the "hydration water backbone" can have a noticeable effect on the charge transfer/transport properties of some DNA types. Leveritt et al. [315], have designed an electrostatic model to investigate the effect of humidity on the ionic conductivity of DNA assemblies, treating each DNA molecule independently and assuming that each one is surrounded by a layer of water where ions are confined. Their results indicate that the dramatic increase in DNA conductance of six orders of magnitude with increasing humidity is due to the change in ion binding energy induced by the electric field confinement within the water layer, thus leading to a very high sensitivity to the thickness of the water layer. As a matter of fact, single-molecule sensing based on solvation effects surrounding a current-carrying organic backbone molecule has been proposed based on a nonequilibrium Green's function calculations [316].

Effects of water wetting on the transport properties of molecular nanojunctions made from organic molecules and carbon nanotubes were investigated by Rungger et al. [317] using a combination of empirical-potential molecular dynamics and quantum electronic-transport calculations within the density functional theory and Green's function theory. Their calculations showed that water effectively produces electrostatic gating to the molecular junction, with a gating potential due to the time-averaged water dipole field. For DNA, quantum mechanical calculations revealed that water molecules in the first hydration shell around guanine–cytosine radical anion pairs (RAPs) facilitate the proton-transfer reaction [318]. The water arrangement around an embedded GC RAP is different from that around an isolated GC RAP, which can result in a very different solvent effect on the energetics of the proton transfer. Base stacking and hydration in these systems are much more important than the effects of the sugar–phosphate backbone and counterions. Multiscale calculations, combining quantum mechanics and molecular mechanics (QM/MM) [319], with the quantum calculations being performed using density functional theory, have shown that the hole transfer across adenine bridges in double-stranded DNA is codetermined by the large fluctuations of site energies induced by the solvent degrees of freedom, reducing drastically the barrier for the hole transfer. An accurate description of solvent effects and a proper sampling of molecular configurations is required to describe the gating of charge transfer in DNA. It was also proposed a DFT/classical molecular dynamics model to model DNA charge conductivity including effects from temperature, hole-hopping charge transfer and time-dependent nonequilibrium interaction of DNA with its molecular environment [320]. This approach predicted a significant hole-transfer slowdown when one switches from dry to wet DNA with and without electric field bias and, in agreement with experiments, an insulating behavior of guanine–cytosine oligomers depending on the experimental setup and on the number of base pairs. Finally, Car–Parrinello molecular dynamics (CPMD) simulations were carried out to investigate the interactions between nucleic acid bases and bulk water [321], providing details on the average number, lifetimes and mobility of water molecules, as well as the orientation and 3D distribution of hydrogen bonds in the first hydration shell of adenine, guanine, cytosine and thymine. Differences in hydration studied using CPMD and quantum chemistry suggest a significant effect of the second hydration shell on the structure and properties of the first hydration shell for the solvated nucleobases.

9.3. Modeling DNA charge transport: advances and challenges

DNA structural disorder and dynamic fluctuations make the measurement of the conductivity of DNA strands a daunting task for experimentalists. In particular, dynamic fluctuations occurring on the picosecond and nanosecond time scales are expected to have a strong effect on the ability of DNA to transport charge. Any model of charge transport in DNA must consider effects of static and dynamic disorder, as static disorder attenuates long-range charge transport, and dynamic disorder allows the formation of transient pathways [322]. After measurements of quantum yields for charge transport across adenine chains of increasing length [323], contributions of single- and multistep channels to DNA charge transport were isolated, establishing that coherent transport through DNA occurs mainly across 10 base pairs due to the delocalization of electronic states over a full helix turn, showing that models of charge migration in DNA must take into account the contribution of coherent transfer over long distances. Besides, biological polymers have a very complicate composition of their subunits, and can support long-living nonlinear excitations. Modulation instability can activate solitons in DNA, and recently a study has showed that the nonlinear dynamics of charge transport in the DNA helix can be described using a modified discrete nonlinear Schrödinger equation [324]. Even so, thermal fluctuations and dissipation effects on the solitonic patterns must be addressed.

A computational search for DNA π-stacked structures with high electric conductance was carried out by Berlin et al. [325] using semiempirical calculations (INDO/S Hamiltonian). The identification of guanine–cytosine (G–C) and adenine–thymine (A–T) neighboring configurations, that allow strong electronic coupling and molecular electric conductance much larger than equivalent reference systems in the literature, provides guidance for the fabrication of DNA devices and DNA-based elements for nanoscale molecular circuits. A new model to explain the role of electrons at the lowest unoccupied molecular orbitals (LUMO) in the electrical conduction through the DNA molecule was proposed by Abdalla [326], with a good fitting of calculated DC and AC conductivities and dielectric permittivity of a DNA molecule to experimental data. Its results were presented as evidence that free carriers in the LUMO and HOMO are responsible to make the DNA molecule a conductor, insulator or semiconductor.

While model Hamiltonians are a powerful tool to investigate DNA charge transport, oversimplified parameters are still an issue to be addressed. Fragment orbital basis techniques can be useful to improve them, avoiding the need to adjust experimental parameters in approaches such as DFT, to estimate site energies and hopping terms [327]. Unfortunately, pure

DFT functionals have limitations: they do not describe well excited states and dispersion forces such as van der Waals interactions. However, DFT-based results can be used as a guide to predict trends in DNA conductivity. As an example, we mention the electrical conductivity of dry and hydrated DNA duplexes between two Au electrodes investigated by Maeda et al. [328] using the Green's function method coupled with DFT computations. When explicit water molecules were included in their modeling, the calculated electrical currents for two different duplexes were increased by about an order of magnitude, in qualitative agreement with experimental data. The same approach was also employed to investigate the electrical conducting properties of artificial DNA duplexes, which use artificial nucleobases based on adenine to prevent oxidative damage [329]. The results describe well the origin of the experimentally observed high conductivity through artificial DNA duplexes, while the simulations allow the design of novel artificial DNA bases with low ionization energies to build novel artificial DNA duplexes for potential use as highly conductive nanowires.

The bias-dependent transport properties of short poly(G)–poly(C) A-DNA strands coupled to Au electrodes were investigated using first-principles electronic transport methods and the nonequilibrium Green's function approach with self-interaction corrected DFT. As a result, a full self-consistent coherent *I–V* curve of various DNA fragments were obtained, indicating that electron transport through DNA is due to a sequence-specific short-range tunneling across a few bases, in combination with diffusive/inelastic mechanisms [330]. The zero-bias conductance of dry DNA was calculated using density functional theory and phenomenological Büttiker probes to account for decoherence effects [331]. The results suggest that, while the phenomenological Büttiker probes are able to describe experiments qualitatively at low bias, a more accurate treatment of vibronic coupling is necessary to explain experimental data at larger biases, which requires a better knowledge of vibronic modes and coupling strengths for DNA strands.

A computational analysis on how the electronic properties of nucleobase stacks depend on the sequence and conformation was performed by Rooman and Wintjens [332], by using the M06-2X hybrid exchange–correlation functional, showing that the charge and spin density vary at each site of the DNA molecule according with the conformation. This means that conformational variations occurring in biological systems due to the flexibility of the DNA molecule can affect these electronic properties, as many transcription factors alter the structure of DNA upon binding. On the other hand, recent developments in Coupled-Cluster (CC) excited states theory have allowed the application of computationally expensive methods to the study of nucleobases and even their complexes, with encouraging results [333–336]. These developments suggest the feasibility of extending these types of calculations to simulate vibronic spectra, model environmental effects and electron transfer. They also can be useful to find out the mechanism behind the relaxation dynamics of excited states: if it is ruled by intra-strand or inter-strand processes. CC theory can also provide accurate values for site energies and electronic couplings for charge transport models, providing a benchmark parametrization and allowing the comparison of the charge transport probability between stacked and Watson–Crick pairs. The implementation of approximate CC methods, however, is necessary to investigate larger systems, and a comparison between them can be very useful to understand the role of different contributions included or neglected across different approximations.

A periodic modeling of DNA double helices in nucleosomes at different temperatures was carried out by Bende et al. [337] using the Hartree–Fock crystal orbital method, in order to obtain the electronic band structures and evaluate hole mobilities. The results for poly(G–G) structures were shown to be in good agreement with equivalent tight-binding calculations and the method can also be useful to describe the charge transport in DNA of 34 nm (more than 100 pairs) observed by Barton et al. [338], which have proposed an explanation based on a charge transport coherent mechanism (implying the existence of energy bands). A model for hole migration in short DNA hairpins, based on the numerical solution of the Liouville equation with the Hamiltonian including some molecular vibration modes explicitly, was recently formulated and applied to poly(A)–poly(T) with less than seven base pairs [339]. The results suggest that superexchange can be responsible for the hole transfer from donor to acceptor in poly(A)–poly(T) hairpins with one or two base pairs, while for longer hairpins a high degree of delocalization of the positive charge along the entire system was observed. However, partial localization present in the latter mechanism indicates that charge transfer in short DNA hairpins proceeds through an intermediate mechanism distinct from both superexchange and hopping.

Adsorption of DNA nucleosides on metallic surfaces, on the other hand, is valuable to understand the wrapping of adsorbed DNA in vacuum and in solution, crucial for the design of DNA-based nanodevices. Classical molecular dynamics was used as a tool to understand the self-assembly mechanism of DNA nucleobases on the Au(111) surface, with optimized geometries and electrostatic point charges being calculated using the hybrid B3LYP exchange–correlation functional [340]. The results provided detailed useful information to improve the stability and activity of nucleotide captured layers. Afterwards, the structural and electronic properties of DNA nucleosides adsorbed on Au(100) and Cu(111) were investigated [341,342], the latter using DFT calculations including van der Waals interactions through the LMKLL exchange–correlation functional, which allows for the study of long-range interactions in a rigorous manner [343]. While the standard PBE exchange–correlation functional underestimates the binding energy to about 30% of LMKLL, it has been shown that van der Waals interactions compete with the formation of specific bonds, and favor a parallel orientation of the DNA bases with respect to the surface, as well as promoting the shortening of the molecule-surface distance. Significant differences in the electronic density of states can also be noted if one compares the van der Waals-corrected functional with the pure PBE functional results, affecting the molecule-surface charge transfer. Hence, it is necessary to take into account van der Waals effects in DFT calculations if one wants to obtain a correct description of DNA nucleosides adsorbed in metallic surfaces.

A phenomenological statistical model based on a tight-binding description of DNA was developed to understand the influence of decoherence and bonding on the linear conductance of single double-stranded DNA molecules with

tight-binding parameters obtained from DFT computations, the results exhibiting a good fit to experimental data [137]. The properties of static and dynamic polarons were investigated using a modified tight-binding Su–Schrieffer–Heeger (SSH) model, with the dynamics being obtained for different order calculations [344]. These theoretical calculations revealed that a polaron can tunnel through a potential barrier of at most 3 bases, which was also observed in experiments. The effect of phonons and backbone disorder on electronic transport in DNA molecules was investigated using a two-channel tight-binding model and transfer matrix to obtain the localization length of a charge carrier within the molecule [345]. It was shown that above (below) a threshold frequency, phonons can improve (prevent) the electron transport in DNA with backbone disorder. In order to improve the tight-binding approach to simulate charge transport in DNA strands, an advanced tight-binding model was proposed [346], which includes hopping integrals of the next-nearest-neighbor (*nnn*) nucleobases, and takes into account how the curved helical structure affects the on-site energies. The calculated transmission and current–voltage characteristics, as a function of the electron energy and source–drain voltage, with a variation of the contact coupling between the leads and the DNA's molecule and tilt angle were obtained, and the results reveal that the electron transmission and current flow are enhanced by including *nnn* effects, while increasing the helical tilting angle decreases the electron current across the DNA strand. Nevertheless, the development of new methods to address charge transport in complex molecules demands more sophisticated approaches, including combining molecular dynamics simulations with electronic structure calculations to estimate the parameters to be used in effective model Hamiltonians capable to deal with distinct charge transport scenarios in DNA and similar systems. This approach has the advantage to allow the development of a controlled coarse-graining of the electronic structure and, consequently, a tuning of the degree of complexity of the Hamiltonians for transport modeling. Besides, it also allows the study of other polymers and organic crystals. The reliability of quantum simulations using classical trajectories and injected charge effects, however, must be addressed as well [346].

9.4. Summary

In the last few years, many promising developments have occurred in the field of DNA charge transport toward the development of DNA-based nanostructures and nanodevices. In order to account to some of these achievements, we have provided here a review text on the state of the art of the DNA's unique physical properties. As the field of nanotechnology is nowadays one of the most important area of research, DNA-mediated self-assembly has the potential to profoundly impact this field, since its ability to choose the sequence of nucleotides, and hence provide addressability during the self-assembly processes, makes DNA an ideal molecule for nanobiostructured devices.

The possibility of developing new sophisticated nanodevices integrating man-made nanostructures with biomolecules such as the nucleic acid analogs [347], as well as the integration of three-dimensional DNA arrays, nanoparticles and nano-electronic components [348] with some precision, is seeking for new theoretical analysis of the emerging physical properties of these complex structures, similar to those discussed in this review article. By the way, the direct electrical interfacing at the biomolecular level discussed here surely opens the possibility of monitoring and controlling critical biological functions and processes in unprecedented ways, giving rise to a vast array of possibilities such as medical monitoring devices, drug delivery systems, and patient monitoring systems, to cite just a few.

Among its main features, we have discussed several important topics related with the DNA's molecule, including the electronic density of state, energy profiles, thermodynamic properties, localization, scale laws, fractal and multifractal analysis and anhydrous crystals. Some related emerging topics, that should deserve attention in the years to come, are highlighted above in this section, keeping in mind that, since this subject is rapidly changing, a good comprehension of the concepts developed so far should be worthwhile to open up new avenues for technological innovations. This includes experimental techniques taking into account that, since experimental reality is approaching theoretical models and assumptions, detailed analysis and precise predictions are being made possible nowadays.

Acknowledgments

References

[1] S. Luryi, J.M. Xu, A. Zaslavsky (Eds.), Future Trends in Microelectronics: The Road Ahead, Wiley, New York, 1999.
[2] R.G. Endres, D.L. Cox, R.R.P. Singh, Rev. Modern Phys. 76 (2004) 195.
[3] S. Datta, Quantum Transport: Atom to Transistor, Cambridge University Press, Cambridge, 2005.
[4] E. Braun, K. Keren, Adv. Phys. 53 (2004) 441.
[5] C. Nicoloni, Molecular Bioelectronics, World Scientific, Singapore, 1996.
[6] G. Cuniberti, G. Fagas, G. Richter (Eds.), Introducing Molecular Electronics, in: Lecture Notes in Physics, Vol. 680, Springer, Berlin, 2005.
[7] S.O. Kelley, J.K. Barton, Science 283 (1999) 375.
[8] L.T. Cai, H. Tabata, T. Kawai, Appl. Phys. Lett. 77 (2000) 3105.
[9] A.Y. Kasumov, M. Kociak, S. Guron, B. Reulet, V.T. Volkov, D.V. Klinov, H. Bouchiat, Science 291 (2001) 280.
[10] K.W. Hipps, Science 294 (2001) 536.
[11] M. Taniguchi, T. Kawai, Phys. Rev. E 70 (2004) 11913.

[12] C. Joachim, M.A. Ratner, Proc. Natl. Acad. Sci. USA 102 (2005) 8801.
[13] J. Park, A.N. Pasupathy, J.I. Goldsmith, C. Chang, Y. Yaish, J.R. Petta, M. Rinkoski, J.P. Sethna, H.D. Abrua, P.L. McEuen, D.C. Ralph, Nature 417 (2002) 722.
[14] W.J. Liang, M.P. Shores, M. Bockrath, J.R. Long, H. Park, Nature 417 (2002) 725.
[15] J.D. Watson, F.H.C. Crick, Nature 171 (1953) 737.
[16] J.D. Watson, F.H.C. Crick, Nature 171 (1953) 964.
[17] F.H.C. Crick, J.D. Watson, Proc. R. Soc. Lond. 223 (1954) 80.
[18] H. Lodish, D. Baltimore, A. Berk, S.L. Zipursky, P. Matsudaira, J. Darnell, Molecular Cell Biology, Scientific American Books Inc., 1995.
[19] E. Vischer, E. Chargaff, J. Biol. Chem. 176 (1948) 703.
[20] E. Chargaff, S. Zamenhof, C. Green, Nature 165 (1950) 756.
[21] H.-A. Wagenknecht (Ed.), Charge Transfer in DNA: From Mechanism to Application, Wiley, New York, 2005.
[22] F.D. Lewis, T. Wu, Y. Zhang, R.L. Letsinger, S.R. Greenfield, M.R. Wasielewski, Science 277 (1997) 673.
[23] K. Keren, R.S. Berman, E. Buchstab, U. Sivan, E. Braun, Science 302 (2003) 1380.
[24] Y. Zhang, R.H. Austin, J. Kraeft, E.C. Cox, N.P. Ong, Phys. Rev. Lett. 89 (2002) 198102.
[25] E. Winfree, F. Liu, L.A. Wenzler, N.C. Seeman, Nature 394 (1998) 539.
[26] D. Porath, A. Bezryadin, S. De Vries, C. Dekker, Nature 403 (2000) 635.
[27] B. Xu, P. Zhang, X. Li, N. Tao, Nano Lett. 4 (2004) 1105.
[28] Yu. Kasumov, D.V. Klinov, P.-E. Roche, S. Guéron, H. Bouchiat, Appl. Phys. Lett. 84 (2004) 1007.
[29] F. Ortmann, K. Hannewald, F. Bechstedt, J. Phys. Chem. B 112 (2008) 1540.
[30] N.C. Seeman, Annu. Rev. Biophys. Biomol. Struct. 27 (1998) 225.
[31] N.C. Seeman, J. Theoret. Biol. 99 (1982) 237.
[32] N.C. Seeman, Nature 421 (2003) 427.
[33] J. Chen, N.C. Seeman, Nature 350 (1991) 631.
[34] Y. Zhang, N.C. Seeman, J. Am. Chem. Soc. 116 (1994) 1661.
[35] P.W.K. Rothemund, Nature 440 (2006) 297.
[36] H. Gu, J. Chao, S.J. Xiao, N.C. Seeman, Nat. Nanotechnol. 4 (2009) 245.
[37] J. Zheng, J.J. Birktoft, Y. Chen, T. Wang, R. Sha, P.E. Constantinou, S.L. Ginell, C.D. Mao, N.C. Seeman, Nature 461 (2009) 74.
[38] N.C. Seeman, Annu. Rev. Biochem. 79 (2010) 65.
[39] E. Shapir, H. Cohen, A. Calzolari, C. Cavazzoni, D.A. Ryndyk, G. Cuniberti, A. Kotlyar, R. Di Felice, D. Porath, Nature Mater. 7 (2008) 68.
[40] A. Malishev, Phys. Rev. Lett. 98 (2007) 096801.
[41] E.L. Albuquerque, M.G. Cottam, Phys. Rep. 233 (1993) 67.
[42] E.L. Albuquerque, M.G. Cottam, Polaritons in Periodic and Quasiperiodic Structures, Elsevier, Amsterdam, 2004.
[43] E. Maciá, Rep. Progr. Phys. 69 (2006) 397.
[44] E. Braun, Y. Eichen, U. Sivan, G. Ben-Yoseph, Nature (London) 391 (1998) 775.
[45] C. Treadway, M.G. Hill, J.K. Barton, Chem. Phys. 281 (2002) 409.
[46] P. Carpena, P.B-. Galván, P.Ch. Ivanov, H.E. Stanley, Nature 418 (2002) 955. 421 (E) (2003) 764.
[47] P. O'Neill, A.W. Parker, M.A. Plumb, L.D.A. Siebbeles, J. Phys. Chem. B 105 (2001) 5283.
[48] G. Weber, Europhys. Lett. 73 (2006) 806.
[49] M. Zoli, Phys. Rev. E 81 (2010) 051910.
[50] M. Zoli, J. Chem. Phys. 135 (2011) 115101.
[51] M. Peyrard, A.R. Bishop, Phys. Rev. Lett. 62 (1989) 2755.
[52] T. Dauxois, M. Peyrard, Phys. Rev. E 51 (1995) 4027.
[53] G. Cuniberti, L. Craco, D. Porath, C. Dekker, Phys. Rev. B 65 (2002) 241314 (R).
[54] D. Schechtman, I. Blech, D. Gratias, J.W. Cahn, Phys. Rev. Lett. 53 (1984) 1951.
[55] P.J. Steinhard, S. Ostlund, The Physics of Quasicrystals, World Scientific, Singapore, 1987.
[56] C. Janot, Quasicrystals, A Primer, Oxford Univ. Press, Oxford, 1993.
[57] F. Hippert, D. Gratias (Eds.), Lectures on Quasicrystals, Les Editions de Physique, Les Ulis, 1994.
[58] M. Senechal, Quasicrystals and Geometry, Cambridge University Press, Cambridge, 1995.
[59] D.P. DiVincenzo, P.J. Steinhardt (Eds.), Quasicrystals: The State of the Art, second ed., World Scientific, Singapore, 1999.
[60] D. Levine, P.J. Steinhardt, Phys. Rev. Lett. 53 (1984) 2477.
[61] R. Penrose, Bull. Inst. Math. Appl. 10 (1974) 266.
[62] C.G. Bezerra, E.L. Albuquerque, Physica A 255 (1998) 285.
[63] C.G. Bezerra, J.M. de Araujo, C. Chesman, E.L. Albuquerque, Phys. Rev. B 60 (1999) 9264.
[64] D.H.A.L. Anselmo, M.G. Cottam, E.L. Albuquerque, J. Phys.: Condens. Matter 12 (2000) 1041.
[65] A. Bovier, J.-M. Ghez, Comm. Math. Phys. 158 (1993) 45.
[66] F. Axel, J. Peyriére, C. R. Acad. Sci. de Paris 306 (1988) 179.
[67] F. Axel, H. Terauchi, Phys. Rev. Lett. 66 (1991) 2223.
[68] F. Axel, J.P. Allouche, Z.Y. Wen, J. Phys.: Condens. Matter 4 (1992) 8713.
[69] E.L. Albuquerque, M.G. Cottam, Solid State Commun. 81 (1992) 383.
[70] L.E. Reichl, A Modern Course in Statistical Physics, Texas University Press, Austin, 1980.
[71] H.E. Stanley, Introduction to Phase Transitions and Critical Phenomena, Oxford University Press, Oxford, 1971.
[72] M.S. Vasconcelos, P.W. Mauriz, F.F. de Medeiros, E.L. Albuquerque, Phys. Rev. B 76 (2007) 165117.
[73] R.E. Prange, D.R. Grempel, S. Fishman, Phys. Rev. B 29 (1984) 6500.
[74] J.M. Luck, D. Petritis, J. Stat. Phys. 42 (1986) 289.
[75] J. Bellisard, D. Bessis, P. Moussa, Phys. Rev. Lett. 49 (1982) 701.
[76] S. Ostlund, R. Pandit, D. Rand, H.J. Schellnhuber, E.D. Siggia, Phys. Rev. Lett. 50 (1983) 1873.
[77] M. Kohmoto, L.P. Kadanoff, C. Tang, Phys. Rev. Lett. 50 (1983) 1870.
[78] K. Nakamura, Quantum Chaos: A New Paradigm of Nonlinear Dynamics, Cambridge University Press, Cambridge, 1993.
[79] P.A. Lee, T.V. Ramakrishnan, Rev. Modern Phys. 57 (1985) 287.
[80] J.B. Sokoloff, Phys. Rep. 126 (1985) 189.
[81] S. Ostlund, R. Pandit, Phys. Rev. B 29 (1984) 1394.
[82] J.P. Lu, T. Odagaki, J.L. Birman, Phys. Rev. B 33 (1986) 4809.
[83] F. Nori, J.P. Rodriguez, Phys. Rev. B 34 (1984) 2207.
[84] F.M. Dekking, J. Combin. Theory 27A (1976) 292.
[85] F.M. Dekking, C. R. Acad. Sci. de Paris 285 (1977) 157.
[86] G. Christol, T. Kamae, M. Mendes-France, G. Rauzy, Bull. Soc. Math. (France) 108 (1980) 401.
[87] A. Cobham, Math. Syst. Theory 3 (1969) 186.
[88] A. Cobham, Math. Syst. Theory 6 (1972) 164.
[89] G.T. Herman, G. Hozenberg, Developmental Systems and Languages, North-Holland, Amsterdam, 1975.
[90] M. Queffélec, Substitution Dynamical Systems: Spectral Analysis, in: Lecture Notes in Mathematics, Vol. 1294, Springer-Verlag, Heidelberg, 1987.
[91] B.B. Mandelbrot, The Fractal Geometry of Nature, Freeman, New York, 1982.

[92] P.G. Drazin, Nonlinear Systems, Cambridge University Press, Cambridge, 1992.
[93] S.H. Strogatz, Nonlinear Dynamics and Chaos, Addison-Wesley, Reading, 1994.
[94] U. Grimm, M. Baake, Aperiodic Ising Models, in: R.V. Moody (Ed.), The Mathematics of Long-Range Aperiodic Order, Kluwer, Dordrecht, 1997.
[95] P.W. Mauriz, M.S. Vasconcelos, E.L. Albuquerque, Physica A 329 (2003) 101.
[96] J.A. McCammon, S. Harvey, Dynamics of Proteins and Nucleic Acids, Cambridge University Press, Cambridge, 1987.
[97] M.A. Stroscio, M. Dutta (Eds.), Biological Nanostructures and Applications of Nanostructures in Biology: Electrical, Mechanical and Optical Properties, Kluwer, New York, 2004.
[98] T.G. Drummond, M.G. Hill, J.K. Barton, Nat. Biotechnol. 21 (2003) 1192.
[99] C. Nogues, S.R. Cohen, S. Daube, N. Apter, R. Naaman, J. Phys. Chem. B 110 (2006) 8910.
[100] I.L. Garzon, E. Artacho, M.R. Beltran, A. Garcia, J. Junquera, K. Michaelian, P. Ordejon, C. Rovira, D. Sanchez-Portal, J.M. Soler, Nanotechnology 12 (2001) 126.
[101] A. Rakitin, P. Aich, C. Papadopoulos, Y. Kobzar, A. Vendeneev, J. Lee, J. Xu, Phys. Rev. Lett. 86 (2001) 3670.
[102] B. Alberts, D. Bray, J. Lewis, M. Raff, K. Roberts, J. Watson, Molecular Biology of the Cell, Garland, New York, 1994.
[103] E. Boon, A. Livingston, N. Chmiel, S. David, J. Barton, Proc. Natl. Acad. Sci. USA 100 (2003) 12543.
[104] R.N. Barnett, C.L. Cleveland, U. Landman, E. Boone, S. Kanvah, G.B. Schuster, J. Phys. Chem. A 107 (2003) 3525.
[105] R. Di Felice, A. Calzolari, H. Zhang, Nanotecnology 15 (2004) 1256.
[106] A.A. Voityuk, J. Chem. Phys. 128 (2008) 115101.
[107] E. Maciá, S. Roche, Nanotechnoloy 17 (2006) 3002.
[108] R. Gutiérrez, S. Mandal, G. Cuniberti, Nano Lett. 5 (2005) 1093.
[109] C.T. Shih, S. Roche, R.A. Römer, Phys. Rev. Lett. 100 (2008) 018105.
[110] Y.S. Joe, S.H. Lee, E.R. Hedin, Phys. Lett. A 374 (2010) 2367.
[111] S. Roche, Phys. Rev. Lett. 91 (2003) 108101.
[112] S. Roche, S.D. Bicout, E. Maciá, E. Kats, Phys. Rev. Lett. 91 (2003) 228101.
[113] H. Yamada, Phys. Lett. A 332 (2004) 65.
[114] G. Xiong, X.R. Wang, Phys. Lett. A 344 (2005) 64.
[115] N.W. Ashcroft, N.D. Mermin, Solid State Physics, Saunders College Publishing, New York, 1976.
[116] C. Kittel, Quantum Theory of Solids, second ed., Wiley, New York, 1987.
[117] J. Callaway, Energy Band Theory, Academic Press, New York, 1964.
[118] W. Harrison, Electronic Structure and the Properties of Solids: The Physics of the Chemical Bond, Dover, New York, 1989.
[119] P. Hohenberg, W. Kohn, Phys. Rev. 136 (1964) B864.
[120] W. Kohn, L.J. Sham, Phys. Rev. 140 (1965) A1133.
[121] W. Kohn, Rev. Modern Phys. 71 (1999) 1253.
[122] T. Terao, Phys. Rev. B 56 (1997) 975.
[123] G. Gumbs, G.S. Dubey, A. Salman, B.S. Mahmoud, D. Huang, Phys. Rev. B 52 (1995) 210.
[124] P.W. Mauriz, M.S. Vasconcelos, E.L. Albuquerque, Physica A 294 (2001) 403.
[125] H.Q. Yuan, U. Grimm, P. Repetowicz, M. Schreiber, Phys. Rev. B 62 (2000) 15569.
[126] M. Kohmoto, J.R. Banavar, Phys. Rev. B 34 (1986) 563.
[127] E.L. Albuquerque, M.S. Vasconcelos, M.L. Lyra, F.A.B.F. de Moura, Phys. Rev. E 71 (2005) 021910.
[128] F. Dyson, Phys. Rev. 75 (1949) 1736.
[129] J. Schwinger, PNAS 37 (1951) 452.
[130] B.P.W. de Oliveira, E.L. Albuquerque, M.S. Vasconcelos, Surf. Sci. 600 (2006) 3770.
[131] H. Sugiyama, I. Saito, J. Am. Chem. Soc. 118 (1996) 7063.
[132] A.A. Voityuk, J. Jortner, M. Bixon, N. Rsch, J. Chem. Phys. 114 (2001) 5614.
[133] E. Maciá, F. Triozon, S. Roche, Phys. Rev. B 71 (2005) 113106.
[134] Y.A. Berlin, A.L. Burin, M.A. Ratner, Chem. Phys. 275 (2002) 61.
[135] A.-M. Guo, S.-J. Xiong, Phys. Rev. E 79 (2009) 041924.
[136] J.H. Wei, K.S. Chan, J. Phys.: Condens. Matter 19 (2007) 286101.
[137] M. Zilly, O. Ujsághy, D.E. Wolf, Phys. Rev. B 82 (2010) 125125.
[138] K. Senthilkumar, F.C. Grozema, C.F. Guerra, F.M. Bickelhaupt, F.D. Lewis, Y.A. Berlim, M.A. Ratner, L.D.A. Siebbeles, J. Am. Chem. Soc. 127 (2005) 14894.
[139] T. Kubar, P.B. Woiczikowski, G. Cuniberti, M. Elstner, J. Phys. Chem. B 112 (2008) 7937.
[140] H. Zhang, X.-Q. Li, P. Han, X.Y. Yu, Y. Yan, J. Chem. Phys. 117 (2002) 4578.
[141] R.G. Sarmento, G.A. Mendes, E.L. Albuquerque, U.L. Fulco, M.S. Vasconcelos, O. Ujsághy, V.N. Freire, E.W.S. Caetano, Phys. Lett. A 376 (2012) 2413.
[142] P. Dean, Rev. Modern Phys. 44 (1972) 127.
[143] R.G. Sarmento, E.L. Albuquerque, P.D. Session Jr., U.L. Fulco, B.P.W. de Oliveira, Phys. Lett. A 373 (2009) 1486.
[144] E. Maciá, Phys. Rev. B. 74 (2006) 245105.
[145] G. Cuniberti, E. Maciá, A. Rodriguez, R.A. Römer, Charge Migration, in: DNA: Perspectives from Physics Chemistry and Biology, NanoScience and Technology, Springer, Berlin, 2007.
[146] D. Klotsa, R.A. Römer, M.S. Turner, Biophys. J. 89 (2005) 2187.
[147] E. Díaz, J. Chem. Phys. 128 (2008) 175101.
[148] R.G. Sarmento, U.L. Fulco, E.L. Albuquerque, E.W.S. Caetano, V.N. Freire, Phys. Lett. A 375 (2011) 3993.
[149] F.A.B.F. de Moura, M.L. Lyra, Phys. Rev. Lett. 81 (1998) 3735.
[150] A. Nitzan, Annu. Rev. Phys. Chem. 52 (2001) 681.
[151] J.P. Lewis, T.E. Cheatham III, E.B. Strikov, H. Wang, O.F. Sarkey, J. Phys. Chem. B 107 (2003) 2581.
[152] Y. Asai, J. Phys. Chem. B 107 (2003) 4647.
[153] V.M. Kucherov, C.D. Kinz-Thompson, E.M. Conwell, J. Phys. Chem. C 114 (2010) 1663.
[154] A.D. Stone, J.D. Joannopoulos, D.J. Chadi, Phys. Rev. B 24 (1981) 5583.
[155] R. Gutiérrez, S. Mohapatra, H. Cohen, D. Porath, G. Cuniberti, Phys. Rev. 74 (2006) 235105.
[156] J.S. Hwang, K.J. Kong, D. Ahn, G.S. Lee, D.J. Ahn, S.W. Hwang, Appl. Phys. Lett. 81 (2002) 1134.
[157] R. Landauer, IBM J. Res. Dev. 1 (1957) 223; Phil. Mag. 21 (1970) 863; J. Math. Phys. 37 (1996) 223–231.
[158] M. Büttiker, Phys. Rev. B 35 (1987) 4123.
[159] H.Y. Zhang, X.Q. Li, P. Han, X.Y. Yu, Y.J. Yan, J. Chem. Phys. 117 (2002) 4578.
[160] L.M. Bezerril, D.A. Moreira, E.L. Albuquerque, U.L. Fulco, E.L. de Oliveira, J.S. de Sousa, Phys. Lett. A 373 (2009) 3381.
[161] M.S. Xu, S. Tsukamoto, S. Ishida, M. Kitamura, Y. Arakawa, R.G. Endres, M. Shimoda, Appl. Phys. Lett. 87 (2005) 083902.
[162] V. Mugica, M. Kemp, A. Roitberg, M.A. Ratner, J. Chem. Phys 104 (1996) 7296.
[163] F.A.B.F. de Moura, M.L. Lyra, E.L. Albuquerque, J. Phys.: Condens. Matter 20 (2008) 075109.
[164] M. Hilke, J. Phys. A 30 (1997) L367.
[165] E. Lazo, M.E. Onell, Phys. Lett. A 283 (2001) 376.
[166] F.A.B.F. de Moura, M.N.B. Santos, U.L. Fulco, M.L. Lyra, E. Lazo, M.E. Onell, Eur. Phys. J. B 36 (2003) 81.
[167] M. Hilke, Phys. Rev. Lett. 91 (2003) 226403.
[168] A. MacKinnon, B. Kramer, Phys. Rev. Lett. 47 (1981) 1546.
[169] A. Mookerjee, I. Dasgupta, T. Saha, Internat. J. Modern Phys. B 9 (1995) 2989.

[170] T. Natsume, K. Dedachi, S. Tanaka, T. Higuchi, N. Kurita, Chem. Phys. Lett. 408 (2005) 381.
[171] H. Mehrez, M.P. Anantram, Phys. Rev. B 71 (2005) 115405.
[172] B.L. Altshuler, Jpn. J. Appl. Phys. Suppl. 26 (1987) 1938.
[173] S.N. Evangelou, P. Argyrakis, Phys. Rev. B 51 (1995) 3489.
[174] S. Sil, S.K. Maiti, A. Chakrabarti, Phys. Rev. Lett. 101 (2008) 076803.
[175] S. Sil, S.K. Maiti, A. Chakrabarti, Phys. Rev. B 78 (2008) 113103.
[176] F.A.B.F. de Moura, R.A. Caetano, M.L. Lyra, Phys. Rev. B 81 (2010) 125104.
[177] R.A. Caetano, P.A. Schulz, Phys. Rev. Lett. 95 (2005) 126601.
[178] R.C.P. Carvalho, M.L. Lyra, F.A.B.F. de Moura, F. Domínguez-Adame, J. Phys.: Condens. Matter 23 (2011) 175304.
[179] A. Sedrakyan, F. Domínguez-Adame, Phys. Rev. Lett. 96 (2006) 059703.
[180] E. Díaz, A. Sedrakyan, D. Sedrakyan, F. Domínguez-Adame, Phys. Rev. B 75 (2007) 014201.
[181] V.M.K. Bagci, A.A. Krokhin, Phys. Rev. B 76 (2007) 134202.
[182] G. Kopidakis, S. Komineas, S. Flach, S. Aubry, Phys. Rev. Lett. 100 (2008) 084103.
[183] Ch. Skokos, D.O. Krimer, S. Komineas, S. Flach, Phys. Rev. E 79 (2009) 056211.
[184] A.S. Pikovsky, D.L. Shepelyansky, Phys. Rev. Lett. 100 (2008) 094101.
[185] D. Hajnal, R. Schilling, Phys. Rev. Lett. 101 (2008) 124101.
[186] Y. Lahini, A. Avidan, F. Pozzi, M. Sorel, R. Morandotti, D.N. Christodoulides, Y. Silberberg, Phys. Rev. Lett. 100 (2008) 013906.
[187] E.B. Starikov, Phil. Mag. 85 (2005) 3435.
[188] M. Johansson, M. Hörnquist, R. Riklund, Phys. Rev. B 52 (1995) 231.
[189] P.K. Datta, K. Kundu, Phys. Rev. B 53 (1996) 14929.
[190] F.A.B.F. de Moura, I. Gléria, I.F. dos Santos, M.L. Lyra, Phys. Rev. Lett. 103 (2009) 096401.
[191] S. Flach, D.O. Krimer, C. Skokos, Phys. Rev. Lett. 102 (2009) 024101.
[192] F.A.B.F. de Moura, U.L. Fulco, M.L. Lyra, F. Domínguez-Adame, E.L. Albuquerque, Physica A 390 (2011) 535.
[193] Z. Pan, S. Xiong, C. Gong, Phys. Rev. E 56 (1997) 4744.
[194] A.V. Malyshev, Phys. Rev. Lett. 98 (2007) 096801.
[195] C. Tsallis, L.R. da Silva, R.S. Mendes, R.O. Vallejos, A.M. Mariz, Phys. Rev. E 56 (1997) R4922.
[196] R.O. Vallejos, R.S. Mendes, L.R. da Silva, C. Tsallis, Phys. Rev. E 58 (1998) 1346.
[197] H.-O. Peitgen, H. Jurgens, D. Saupe, Chaos and Fractals, Springer-Verlag, Heidelberg, 1992.
[198] L.R. da Silva, R.O. Vallejos, C. Tsallis, R.S. Mendes, S. Roux, Phys. Rev. E 64 (2001) 11104.
[199] D.J.B. Soares, M.L. Lyra, L.R. da Silva, Phys. Lett. A 318 (2003) 452.
[200] P.W. Mauriz, E.L. Albuquerque, M.S. Vasconcelos, Phys. Rev. B 63 (2001) 184203.
[201] I.-S. Yang, A.C. Anderson, Phys. Rev. B 35 (1987) 9305.
[202] D.A. Moreira, E.L. Albuquerque, P.W. Mauriz, M.S. Vasconcelos, Physica A 371 (2006) 441.
[203] I. Procaccia, Proceedings of Nobel Symposium on Chaos and Related Problems [Phys. Scr. T9 (1985) 40].
[204] T.C. Halsey, P. Meakin, I. Procaccia, Phys. Rev. Lett. 56 (1986) 854.
[205] A.B. Chhabra, R.V. Jensen, Phys. Rev. Lett. 62 (1989) 1327.
[206] R.O. Vallejos, C. Anteneodo, Phys. Rev. E 58 (1998) 4134.
[207] D.A. Moreira, E.L. Albuquerque, C.G. Bezerra, Eur. Phys. J. B 54 (2006) 393.
[208] G.M. Mrevlishvili, L.L. Buishvili, G.Sh. Japaridze, G.R. Kakabadze, Thermochim. Acta 290 (1996) 65.
[209] G.M. Mrevlishvili, Thermochim. Acta 308 (1998) 49.
[210] D.A. Moreira, E.L. Albuquerque, D.H.A.L. Anselmo, Phys. Lett. A 372 (2008) 5233.
[211] E. Schrödinger, What is Life? The Physical Aspect of the Living Cell, Cambridge University Press, Cambridge, 1945.
[212] D.H.A.L. Anselmo, A.L. Dantas, E.L. Albuquerque, Physica A 362 (2006) 289.
[213] M. Gell-Mann, C. Tsallis (Eds.), Nonextensive Entropy—Interdisciplinary Applications, Oxford University Press, Oxford, 2004.
[214] C. Tsallis, in: C. Beck, A. Rapisarda, C. Tsallis (Eds.), Complexity, Metastability and Nonextensivity, World Scientific, Singapore, 2005.
[215] H. Herrmann, M. Barbosa, E. Curado (Eds.), Physica A 344 (2004) (special issue).
[216] C. Tsallis, J. Stat. Phys. 52 (1988) 479.
[217] J.M. Luck, Th.M. Nieuwenhuizen, Europhys. Lett. 2 (1987) 256.
[218] A. Petri, G. Ruocco, Phys. Rev. B 51 (1995) 11399.
[219] D. Badalian, V. Gasparian, R. Abramian, A. Khachatrian, U. Gummich, Physica B 226 (1996) 385.
[220] P. Carpena, A.V. Coronado, P. Bernaola-Galván, Phys. Rev. E 61 (2000) 2281.
[221] I.N. de Oliveira, M.L. Lyra, E.L. Albuquerque, Physica A 343 (2004) 424.
[222] I.N. de Oliveira, M.L. Lyra, E.L. Albuquerque, L.R. da Silva, J. Phys.: Condens. Matter 17 (2005) 3499.
[223] C. Tsallis, R.S. Mendes, A.R. Plastino, Physica A 261 (1998) 534.
[224] D.A. Moreira, E.L. Albuquerque, L.R. da Silva, D.S. Galvão, Physica A 387 (2008) 5477.
[225] M.L. Lyra, C. Tsallis, Phys. Rev. Lett. 80 (1998) 53.
[226] F. Baldovin, A. Robledo, Phys. Rev. E 69 (2004) 045202.
[227] A.V. Coronado, P. Carpena, Physica A 358 (2005) 299.
[228] P. Carpena, P.B-. Galván, A.V. Coronado, M. Hackenberg, J.L. Oliver, Phys. Rev. E 75 (2006) 032903.
[229] A.V. Coronado, P. Carpena, Phys. Rev. E 73 (2006) 016124.
[230] D.D. Eley, D.I. Spivey, Trans. Faraday Soc. 58 (1962) 411.
[231] R. Di Felice, A. Calzolari, E. Molinari, A. Garbesi, Phys. Rev. B 65 (2001) 045104.
[232] J. Ladik, A. Bende, F. Bogár, J. Chem. Phys. 128 (2008) 105101.
[233] C.F. Guerra, F.M. Bickelhaupt, J.G. Snidjers, E.J. Baerends, J. Am. Chem. Soc. 122 (2000) 4117.
[234] A. Sadowska-Aleksiejew, J. Rak, A.A. Voityuk, Chem. Phys. Lett. 429 (2006) 546.
[235] Y. Mo, J. Mol. Model. 12 (2006) 665.
[236] A. Calzolari, R. Di Felice, E. Molinari, Sol. Stat. Commun. 131 (2004) 557.
[237] A. Robertazzi, J.A. Platts, J. Phys. Chem. A 110 (2006) 3992.
[238] V.R. Cooper, T. Thonhauser, A. Puzder, E. Schröder, B.I. Lundqvist, D.C. Langreth, J. Am. Chem. Soc. 130 (2008) 1304.
[239] F.L. Gervasio, P. Carloni, M. Parinello, Phys. Rev. Lett. 89 (2002) 108102.
[240] A. Hübsch, R.G. Endres, D.L. Cox, R.R.P. Singh, Phys. Rev. Lett. 94 (2005) 178102.
[241] R.N. Barnett, C.L. Cleveland, U. Landman, E. Boone, S. Kanvah, G.B. Schuster, J. Am. Chem. Soc. 107 (2003) 3225.
[242] M. Kabeláč, P. Hobza, Phys. Chem. Chem. Phys. 9 (2007) 903.
[243] F. Ortmann, K. Hannewald, F. Bechstedt, J. Phys. Chem. B 113 (2009) 7367.
[244] S.D. Silaghi, M. Friedrich, C. Cobet, N. Esser, W. Braun, D.R.T. Zahn, Phys. Status Solidi b 242 (2005) 3047.
[245] Y. Zhao, D.G. Truhlar, Phys. Chem. Chem. Phys. 7 (2005) 2701.
[246] T. Van Der Wijst, C.F. Guerra, M. Swart, F.M. Bickelhaupt, Chem. Phys. Lett. 426 (2006) 415.
[247] V.R. Cooper, T. Tronhauser, D.C. Langreth, J. Chem. Phys. 128 (2008) 204102.
[248] P.L. Silvestrelli, J. Phys. Chem. A 113 (2009) 5224.
[249] J. Šponer, J. Lesczyński, P. Hobza, J. Phys. Chem. 100 (1996) 5590.

[250] C.E. Bugg, J.M. Thomas, M. Sundaralingam, S.T. Rao, Biopolymers 10 (1971) 175.
[251] J. Šponer, J. Kypr, J. Biomol. Struct. Dyn. 11 (1993) 277.
[252] J. Šponer, K.E. Riley, P. Hobza, Phys. Chem. Chem. Phys. 10 (2008) 2595.
[253] Z. Czy znikowska, J. Mol. Struct. 895 (2009) 161.
[254] M. Taniguchi, T. Kawai, Phys. Rev. E 70 (2004) 011913.
[255] K. Ozeki, N. Sakabe, J. Tanaka, Acta Crystallogr. Sect. B 25 (1969) 1038.
[256] G. Portalone, L. Bencivenni, M. Colapietro, A. Pieretti, F. Ramondo, Acta Chem. Scand. 53 (1999) 57.
[257] R.J. McClure, B.M. Craven, Acta Crystallogr. Sect. B 29 (1973) 1234.
[258] D.L. Barker, R.E. Marsh, Acta Cryst. 17 (1964) 1581.
[259] S. Mahapatra, S.K. Nayak, S.J. Prathapa, T.N. Guru Row, Crys. Growth Design 8 (2008) 1223.
[260] F.F. Maia Jr., V.N. Freire, E.W.S. Caetano, D.L. Azevedo, F.A.M. Sales, E.L. Albuquerque, J. Chem. Phys. 134 (2011) 175101.
[261] K. Guille, W. Clegg, Acta Cryst. C 62 (2006) o515.
[262] M.C. Payne, M.P. Peter, D.C. Allan, T.A. Arias, J.D. Joannopoulos, Rev. Modern Phys. 64 (1992) 1045.
[263] M.D. Segall, P.J.D. Lindan, M.J. Probert, C.J. Pickard, P.J. Hasnip, S.J. Clark, M.C. Payne, J. Phys.: Condens. Matter 14 (2002) 2717.
[264] D.M. Ceperley, B.J. Alder, Phys. Rev. Lett. 45 (1980) 566.
[265] J.P. Perdew, A. Zunger, Phys. Rev. B 23 (1981) 5048.
[266] S.K. Medeiros, E.L. Albuquerque, F.F. Maia, E.W.S. Caetano, V.N. Freire, Chem. Phys. Lett. 435 (2007) 59.
[267] F. Ortmann, W.G. Schmidt, F. Bechstedt, Phys. Rev. Lett. 95 (2005) 186101.
[268] F. Ortmann, F. Bechstedt, W.G. Schmidt, Phys. Rev. B 73 (2006) 205101.
[269] D. Vanderbilt, Phys. Rev. B 41 (1990) 7892.
[270] B.G. Pfrommer, M. Cote, S.G. Louie, M.L. Cohen, J. Comput. Phys. 131 (1997) 233.
[271] K. Hannewald, V.M. Stojanović, J.M.T. Schellekens, R.A. Bobbert, G. Kresse, J. Hafner, Phys. Rev. B 69 (2004) 075211.
[272] U. Thewalt, C.E. Bugg, R.E. Marsh, Acta Crystallogr. B 27 (1971) 2358.
[273] R.W. Godby, M. Schlüter, L.J. Sham, Phys. Rev. B 37 (1988) 10159.
[274] J.P. Perdew, M. Levy, Phys. Rev. Lett. 51 (1983) 1884.
[275] Z.H. Levine, D.C. Allan, Phys. Rev. B 43 (1991) 4187.
[276] U. Schönberger, F. Aryasetiawan, Phys. Rev. B 52 (1995) 8788.
[277] S.Q. Wang, H.Q. Ye, J. Phys.: Condens. Matter 15 (2003) L197.
[278] J. MacNaughton, A. Moewes, E.Z. Kurmaev, J. Phys. Chem. B 109 (2005) 7749.
[279] K. Hummer, C. Ambrosh-Draxl, Phys. Rev. B 72 (2005) 205205.
[280] W. Wunderlich, H. Ohta, K. Koumoto, Physica B 404 (2009) 2202.
[281] D.N. Beratan, S.S. Skourtis, I.A. Balabin, A. Balaeff, S. Keinan, R. Venkatramani, D.Q. Xiao, Acc. Chem. Res. 42 (2009) 1669.
[282] A.L. Goodwin, M. Calleja, M.J. Conterio, M.T. Dove, J.S.O. Evans, D.A. Keen, L. Peters, M.G. Tucker, Science 319 (2008) 794.
[283] F. Ortmann, F. Bechstedt, K. Hannewald, Phys. Status Solidi b 248 (2011) 511.
[284] R. Friedlein, Y. Wang, A. Fleurence, F. Bussolotti, Y. Ogata, Y. Yamada-Takamura, J. Am. Chem. Soc. 132 (2010) 12808.
[285] M. Fox, Optical Properties of Solids, Oxford University Press, Oxford, 2001.
[286] R. de L Kronig, J. Opt. Soc. Amer. 12 (1926) 547.
[287] S. Lebègue, B. Arnaud, M. Alouani, Phys. Rev. B 72 (2005) 085103.
[288] P.A. Sontz, N.B. Muren, J.K. Barton, Acc. Chem. Res. 45 (2012) 1792.
[289] Y.C. Huang, D. Sen, J. Am. Chem. Soc. 132 (2010) 2663.
[290] W. Cheung, F. Pontoriero, O. Taratula, A.M. Chen, H. He, Adv. Drug Delivery Rev. 62 (2010) 633.
[291] H. Liu, J. He, J. Tang, H. Liu, P. Pang, D. Cao, P. Krstic, S. Joseph, S. Lindsay, C. Nuckolls, Science 237 (2010) 64.
[292] S. Kanvah, J. Joseph, G.B. Schuster, R.N. Barnett, C.L. Cleveland, U. Landman, Acc. Chem. Res. 43 (2010) 280.
[293] P.A. Sontz, T.P. Mui, J.O. Fuss, J.A. Tainer, J.K. Barton, Proc. Natl. Acad. Sci. 109 (2012) 1856.
[294] C.-T. Shih, S.A. Wells, C.-L. Hsu, Y.-Y. Cheng, R.A. Römer, Scientific Rep. 2 (2012) 272.
[295] R.N. Barnett, J. Joseph, U. Landman, G.B. Schuster, J. Am. Chem. Soc. 135 (2013) 3904.
[296] H. Yang, K.L. Metera, H.F. Sleiman, Coord. Chem. Rev. 254 (2010) 2403.
[297] M. Endo, T. Shiroyama, M. Fujitsuka, T. Majima, J. Org. Chem. 70 (2005) 7468.
[298] J.L. Czlapinski, T.L. Sheppard, ChemBioChem 5 (2004) 127.
[299] L.-A. Fendt, I. Bouamaied, S. Thoni, N. Amiot, E. Stulz, J. Am. Chem. Soc. 129 (2007) 15319.
[300] M. Kalek, A.S. Madsen, J. Wengel, J. Am. Chem. Soc. 129 (2007) 9392.
[301] A.J. Fleisher, P.J. Morgan, D.W. Pratt, J. Chem. Phys. 131 (2009) 211101.
[302] E. Shapir, G. Brancolini, T. Molotsky, A.B. Kotlyar, R. Di Felice, D. Porath, Adv. Mater. 23 (2011) 4290.
[303] J.J. Toppari, J. Wirth, F. Garwe, O. Stranik, A. Csaki, J. Bergmann, W. Paa, W. Fritzsche, ACS Nano 7 (2013) 1291.
[304] J.D. Slinker, N.B. Muren, A.A. Gorodetsky, J.K. Barton, J. Am. Chem. Soc. 132 (2010) 2769.
[305] N. Lu, H. Pei, Z. Ge, C.R. Simmons, H. Yan, C. Fan, J. Am. Chem. Soc. 134 (2012) 13148.
[306] I. Rau, J.G. Grote, F. Kajzar, A. Pawlicka, C.R. Physique 13 (2012) 853.
[307] C.G. Pheeney, L.F. Guerra, J.K. Barton, Proc. Natl. Acad. Sci. 109 (2012) 11528.
[308] N. Kang, A. Erbe, E. Scheer, Appl. Phys. Lett. 96 (2010) 023701.
[309] J. Ladik, A. Bende, F. Bogár, Theor. Chem. Acc. 125 (2010) 185.
[310] K. Maie, K. Miyagi, T. Takada, M. Nakamura, K. Yamana, J. Am. Chem. Soc. 131 (2009) 13188.
[311] C. Yamahata, D. Collard, T. Takekawa, M. Kumemura, G. Hashiguchi, H. Fujita, Biophys. J. 94 (2008) 63.
[312] S.S. Mallajosyula, J.C. Lin, D.L. Cox, S.K. Pati, R.R.P. Singh, Phys. Rev. Lett. 101 (2008) 176805.
[313] R. Gutiérrez, R.A. Caetano, B.P. Woiczikowski, T. Kubar, M. Elstner, G. Cuniberti, Phys. Rev. Lett. 102 (2009) 208102.
[314] E.B. Starikov, A. Quintilla, C. Nganou, K.H. Lee, G. Cuniberti, W. Wenzel, Chem. Phys. Lett. 467 (2009) 369.
[315] J.M. Leveritt, C. Dibaya, S. Tesar, R. Shrestha, A.L. Burin, J. Chem. Phys. 131 (2009) 245102.
[316] E. Leary, H. Höbenreich, S.J. Higgins, H. van Zalinge, W. Haiss, R.J. Nichols, C.M. Finch, I. Grace, C.J. Lambert, R. McGrath, J. Smerdon, Phys. Rev. Lett. 102 (2009) 086801.
[317] I. Rungger, X. Chen, U. Schwingenschlögl, S. Sanvito, Phys. Rev. B 81 (2010) 235407.
[318] H.-Y. Chen, C.-L. Kao, S.C.N. Hsu, J. Am. Chem. Soc. 131 (2009) 15930.
[319] T. Kubař, U. Kleinekathöfer, M. Elstner, J. Phys. Chem. B 113 (2009) 13107.
[320] M. Pavanello, L. Adamowicz, M. Volobuyev, B. Mennucci, J. Phys. Chem. B 114 (2010) 4416.
[321] A. Furmanchuk, O. Isayev, O.V. Shishkin, L. Gorb, J. Leszczynski, Phys. Chem. Chem. Phys. 12 (2010) 3363.
[322] J.C. Genereux, J.K. Barton, Chem. Rev. 110 (2010) 1642.
[323] J.C. Genereux, S.M. Wuerth, J.K. Barton, J. Am. Chem. Soc. 133 (2011) 3863.
[324] A.D. Koko, C.B. Tabi, H.P.E. Fouda, A. Mohamadou, T.C. Kofané, Chaos 22 (2012) 043110.
[325] Y.A. Berlin, A.A. Voityuk, M.A. Ratner, ACS Nano 6 (2012) 8216.
[326] S. Abdalla, Prog. Biophys. Mol. Biol. 106 (2011) 485.
[327] S.S. Mallajosyula, S.K. Pati, J. Phys. Chem. Lett. 1 (2010) 1881.
[328] Y. Maeda, A. Okamoto, Y. Hoshiba, T. Tsukamoto, Y. Ishikawa, N. Kurita, Comput. Mater. Sci. 53 (2012) 314.

[329] A. Okamoto, Y. Maeda, T. Tsukamoto, Y. Ishikawa, N. Kurita, Comput. Mater. Sci. 53 (2012) 416.
[330] C.D. Pemmaraju, I. Rungger, X. Chen, A.R. Rocha, S. Sanvito, Phys. Rev. B 82 (2010) 125426.
[331] J. Qi, N. Edirisinghe, M.G. Rabbani, M.P. Anantram, Phys. Rev. B 87 (2013) 085404.
[332] M. Rooman, R. Wintjens, J. Biomol. Struct. Dyn. (2013) http://dx.doi.org/10.1080/07391102.2013.783508.
[333] P.G. Szalay, T. Watson, A. Perera, V.F. Lotrich, R.J. Bartlett, J. Phys. Chem. A 116 (2012) 6702.
[334] P.G. Szalay, T. Watson, A. Perera, V.F. Lotrich, G. Fogarasi, R.J. Bartlett, J. Phys. Chem. A 116 (2012) 8851.
[335] P.G. Szalay, T. Watson, A. Perera, V.F. Lotrich, R.J. Bartlett, J. Phys. Chem. A 117 (2013) 3149.
[336] P.G. Szalay, Int. J. Quantum Chem. 113 (2013) 1821.
[337] A. Bende, F. Bogár, J. Ladik, Chem. Phys. Lett. 565 (2013) 128.
[338] J.D. Slinker, N.B. Muren, S.E. Renfrew, J.K. Barton, Nature Chem. 3 (2011) 228.
[339] N. Renaud, Y.A. Berlin, F.D. Lewis, M.A. Ratner, J. Am. Chem. Soc. 135 (2013) 3953.
[340] A. Maleki, S. Alavi, B. Najafi, J. Phys. Chem. C 115 (2011) 22484.
[341] D. Bogdan, C. Morari, J. Phys. Chem. C 116 (2012) 7351.
[342] D. Bogdan, C. Morari, J. Phys. Chem. A 117 (2013) 4669.
[343] K. Lee, E.D. Murray, L. Kong, B.I. Lundqvist, D.C. Langreth, Phys. Rev. B 82 (2010) 081101.
[344] G. Zhang, H. Hu, S. Cui, Z. Lv, Physica B 405 (2010) 4382.
[345] D.K. Suhendro, E. Yudiarsah, R. Saleh, Physica B 405 (2010) 4806.
[346] R. Gutierrez, G. Cuniberti, J. Self-Assembly Molecular Electron. 1 (2013) 1.
[347] P.S. Lukeman, A. Mittal, N.C. Seeman, Chem. Commun. 15 (1694) 2004.
[348] S.Y. Park, A.K.R. Lytton-Jean, B. Lee, S. Weigand, G.C. Schatz, C.A. Mirkin, Nature 451 (2008) 553.